Modeling of Large-Scale Power Electronics Based Power System

Chou, Shihfeng

DOI (link to publication from Publisher):
10.54337/aau455016835

Publication date:
2021

Document Version
Publisher's PDF, also known as Version of record

MODELING OF LARGE-SCALE POWER ELECTRONICS BASED POWER SYSTEM

BY
SHIH-FENG CHOU

DISSERTATION SUBMITTED 2021

AALBORG UNIVERSITY
DENMARK

Modeling of Large-Scale Power Electronics Based Power System

Ph.D. Dissertation

Shih-Feng Chou

Dissertation submitted July 7, 2021

Dissertation submitted: July 7, 2021

PhD supervisor: Professor Frede Blaabjerg
Aalborg University

Assistant PhD supervisor: Professor Xiongfei Wang
Aalborg University

PhD committee: Associate Professor Amjad Anvari-Moghaddam (chair)
Aalborg University

Dr. Jan R. Svensson
Hitachi Power Grids

Professor Juri Jatskevich
University of British Columbia

PhD Series: Faculty of Engineering and Science, Aalborg University

Department: Department of Energy Technology

ISSN (online): 2446-1636
ISBN (online): 978-87-7210-964-0

Published by:
Aalborg University Press
Kroghstræde 3
DK – 9220 Aalborg Ø
Phone: +45 99407140
aauf@forlag.aau.dk
forlag.aau.dk

Printed in Denmark by Rosendahls, 2021

Abstract

In modern power systems, the increase in renewable energy resources enables power system to replace carbon-intensive energy resources, which can significantly reduce carbon dioxide emission and fight against climate change. Among various renewable energy resources, solar and wind energies have dominated the growth of renewable energy for 20 years, and they still maintain the momentum of growth, which are expected to be even more dominant. Whether it is solar PV generation or wind power generation, these two kinds of renewable energy resources often require power converters interface to connect to the power grid. Due to the demand for power electronic-interfaced renewable energy resources steadily grows, the penetration level of power electronics in modern power systems increases constantly. Since the control dynamics of power electronic converters are multi-time-scale, the interactions between power electronic converters can introduce not only high-frequency voltage and current harmonics into the grid, but also the oscillations in a wide frequency range, which may cause power quality and system stability challenges.

Therefore, to achieve a successful transition to a power electronics-based power system, small-signal modeling methods capable of describing the interactions between adjacent multiple converters in large-scale converter-based power system should be developed. For the system-level stability analysis in power electronic based power systems, it is now achieved by using the aggregated models and reduced-order models developed for synchronous generator based power system in the meantime. Thus, the power-electronic-focused aggregated models are required to evaluate the system stability in a large-scale converter-based power system.

To tackle these issues, this Ph.D. project proposes a small-signal modeling method and stability criterion for single converter and multi-converter systems, which are verified through experimental tests. To further investigate how the parameters in converters affect the oscillations in the system caused by the control dynamics of converters, this Ph.D. project proposes an improved sensitivity analysis method, which can be used to enhance system damping. By employing the presented models, an aggregated model consid-

ering the modularity, scalability, and flexibility can be derived. Accordingly, an workflow for modeling and analyzing large-scale power electronics based power system is summarized, where the presented workflow may be used in future power electronics-based power systems to increase the power system reliability.

Dansk Resumé

I takt med en stigende andel af vedvarende energikilder i det moderne elnet, erstattes teknologier som baserer sig på kul og fossile brændsler, hvilket har en positiv effekt i forhold til bekæmpelsen af klimaforandringerne. Blandt de forskellige vedvarende energikilder har især sol- og vindbaseret energi domineret den samlede vækst af vedvarende energi og den nuværende vækst forventes at tiltage yderligere i den kommende fremtid. I de førnævnte vedvarende energiteknologier kræves der effektelektroniske konvertere til at processere den elektriske effekt inden den leveres til elnettet. På grund af den stadig større implementering af vedvarende energikilder øges mængden af den nødvendige effektelektronik som skal udgøre grænsefladen mellem energikilderne og elnettet. På grund af at kontroldynamikken af effektelektroniske konvertere foregår over flere tidsskalaer, baserer interaktionen mellem disse konvertere ikke kun i form af højfrekvente strøm- og spændingsovertoner men også i form lavfrekvente svingninger. Disse lavfrekvente svingninger kan skabe udfordringer med hensyn til strømkvalitet og systemstabilitet.

For at opnå en vellykket overgang til et effektelektronikbaseret elforsyningssystem, kræves det at der udvikles småsignal modelleringsmetoder, der er i stand til at beskrive de interaktioner der opstår i storskala systemer hvor flere konvertere er lokaliseret i nærheden af hinanden. Med hensyn til de eksisterende systemanalyser af effektelektroniske systemer består af samle modeller af delsystemer og modeller af reduceret kompleksitet som normalt er anvendt på synkron generatorbaseret elsystemer. Derfor er der et behov evaluere systemstabilitet ved hjælp af modeller som gør sig egnet til storskala konverterbaseret elsystemer.

For at overkomme disse problemstillinger, præsenterer dette Ph.D. projekt en småsignal modelleringsmetode og et stabilitetskriterie for både enkeltkonverter – og multikonvertersystemer, som verificeres gennem eksperimentelle tests. Med henblik på at yderligere undersøge, hvordan konverternes kontrolparametre påvirker eventuelle svingninger i systemet, som er direkte forårsaget af konverterens kontroldynamik, præsenterer dette Ph.D. projekt en forbedret sensitivitetsanalyse, som kan anvendes til at forbedre systemdæmpningen. Ved at anvende de præsenterede modeller kan der udledes en samlet

model, som tager højde for modularitet, skalerbarhed og fleksibilitet. Endelig opsummeres en tilsvarende oversigt over den arbejdsgang som kræves til modellering og analyse af effektelektroniskbaseret elsystemer, hvor denne arbjedsgang kan anvendes i fremtidige energisystemer med henblik på at øge disse systemers pålidelighed.

Contents

Thesis Details

Thesis Title: Modeling of Large-Scale Power Electronics Base Power System

Ph.D. Student: Shih-Feng Chou

Supervisors: Professor Frede Blaabjerg, Aalborg University

Professor Xiongfei Wang, Aalborg University

The main part of the dissertation is based on the following publications:
Publications in Referred Journals

[J1] **S. -F. Chou**, X. Wang, and F. Blaabjerg, "Two-Port Network Modeling and Stability Analysis of Grid-Connected Current-Controlled VSCs," in *IEEE Trans. Power Electrons.*, vol. 35, no.4, pp. 3519-3529, April 2020.

[J2] **S. -F. Chou**, X. Wang, and F. Blaabjerg, "Reflection Coefficient Stability Criterion for Multi-Bus Multi-VSC Power Systems," in *IEEE Access*, vol. 8, pp. 111186-111199, 2020.

[J3] **S. -F. Chou**, X. Wang, and F. Blaabjerg, "Frequency-Domain Modal Analysis for Power-Electronic-Based Power Systems," in *IEEE Trans. Power Electrons.*, vol. 36, no. 5, pp. 4910-4914, May 2021.

[J4] **S. -F. Chou**, X. Wang, and F. Blaabjerg, "Use of Modal Quality Factor for Resonance Mode Analysis in VSC-Based Power Systems," under review in *IEEE Journal Emerg. Sel. Topics Power Electron.*, 2020.

[J5] **S. -F. Chou**, X. Wang, and F. Blaabjerg, "Frequency-Dependent Aggregated Model for Power Electronic System," to be submitted to *IEEE Trans. Power Electron.*, 2021.

[J6] **S. -F. Chou**, X. Wang, and F. Blaabjerg, "Impedance-Based Modeling and Analysis Process for VSC Dominant Power System," to be submitted to *IEEE Journal Emerg. Sel. Topics Power Electron.*, 2021.

Publications in Referred Conferences

[C1] **S. -F. Chou**, X. Wang, and F. Blaabjerg, "Stability Analysis of Grid-connected VSCs Based on Two-port Network Theory," *IEEE Applied Power Electronics Conference and Exposition (APEC)*, Anaheim, CA, USA, 2019, pp. 1165-1172

[C2] **S. -F. Chou**, X. Wang, and F. Blaabjerg, "Extensions to Two-Port Network Modeling Method and Analysis of Multiple-VSC-Based Systems," *20th Workshop on Control and Modeling for Power Electronics (COMPEL)*, Toronto, ON, Canada, 2019, pp. 1-8.

[C3] **S. -F. Chou**, X. Wang, and F. Blaabjerg, "Stability Analysis of Grid-Connected VSCs Based on S-parameters and Reflection Coefficient," *IEEE Energy Conversion Congress and Exposition (ECCE)*, Baltimore, MD, USA, 2019, pp. 5171-5178.

[C4] **S. -F. Chou**, X. Wang, and F. Blaabjerg, "Subsynchronous Resonance Analysis in Multi-Bus Multi-VSC Power System Based on Two-Port Network Modeling Method," *IEEE Energy Conversion Congress and Exposition (ECCE)*, Detroit, MI, USA, 2020, pp. 5696-5702.

[C5] **S. -F. Chou**, X. Wang, and F. Blaabjerg, "An Aggregated Model for Power Electronic System Based on Multi-Port Network Reduction Method," *IEEE 21st Workshop on Control and Modeling for Power Electronics (COMPEL)*, Aalborg, Denmark, 2020, pp. 1-6.

This dissertation has been submitted for assessment in partial fulfillment of the Ph.D. degree. The thesis serves as a summary of above publications with highlighting the outcome of the Ph.D. project. Parts of the results are used directly or indirectly in the extended summary of the thesis. The co-author statements have been made available to the assessment committee and are also available at the Faculty of Engineering and Science, Aalborg University.

Preface

This dissertation summarizes the outcomes of the Ph.D. project "Modeling of Large-Scale Power Electronic Based Power Systems", which was carried out at the Department of Energy Technology, Aalborg University, Denmark. This Ph.D. project is supported by the Villum Foundation Denmark through the Reliable Power Electronic based Power Systems (REPEPS) project. The author would like to acknowledge the above-mentioned institutions.

I would like express my sincere gratitude to my supervisor Professor Frede Blaabjerg for his continuous guidance, encouragement, and inspiration throughout the entire Ph.D. study. His valuable recommendations and advice have been essential in completing this thesis. Also, I would like to extended my deepest appreciation to my co-supervisor Professor Xiongfei Wang, who gave me the opportunity to work in Aalborg University when I was seeking a career change, and his constant support and guidance helped me overcome the challenges encountered throughout this Ph.D project.

I would also like to thank Dr. Mats Larsson for his valuable inputs and collaboration during my virtual study abroad with Hitachi ABB Power Grids.

A special thanks to all my colleagues at the Department of Energy Technology, Aalborg University, and especially to Mads Graungaard Taul, Joachim Steinkohl, Martin Kjær, Martin Bendix Fogsgaard, and Amirali Davoodi, for all their suggestions and fruitful discussions for research works, as well as their advice and help for daily life in Denmark.

Finally, I would like to express my most sincere gratitude to my family members, my father Yeh-Yang Chou, my mother Li-Feng Chang, and my brother Yu-Min Chou for their support and understanding. I also wish to pay tribute to my grandmother, Kui-Jung Huang, who passed away in January 2021. May her rest in peace. None of this would have been possible without you.

Shih-Feng Chou
Aalborg University, July 7, 2021

Part I

Report

Chapter 1

Introduction

1.1 Background

In modern power systems, renewable energy resources spread across a wide geographical area, which have brought considerable economic benefits, and helped alleviate climate change. Multiple countries, including Denmark, Germany, South Australia, and certain states in the United States have already achieved high integration of various renewable energy resources. According to International Energy Outlook 2019 from U.S. Energy Information Administration (EIA), it is expected that by 2050, renewable energy power generation will be equal to the coal and natural gas power generations worldwide as shown in Fig. 1.1 [1]. In addition, there are 77 countries, 10 regions, and more than 100 cities committed to achieving net zero carbon emissions by 2050 [2].

Based on the 2020 annual renewable global status report by Renewable Energy Policy Network for the 21^{st} century (REN21), renewable energy had supplied 27.3% of global electricity by end of 2019 [2]. In 2019, the renewable energy reached 75% of the net annual additions in power generating capacity, and since 2012, the net annual addition in renewable energy has exceeded non-renewable energy. Among various renewable energy resources, solar and wind energies have dominated the growth of renewable energy for 20 years, and they still maintain the momentum of growth in 2019 expected to be even more dominant. By 2050, the renewable energies will surpass the fossil-based energy sources, where the solar power and wind power will have equal share of 31% of the renewable energy share [3]. The solar power can be sorted into two kinds, the photovoltaics (PV) directly converts the sunlight into electricity, where the concentrating solar thermal power (CSP) converts the sunlight into heat, which the heat drives a heat engine connected to the electrical generators. Yet, the CSP has the global capacity of 6.2 GW in 2020,

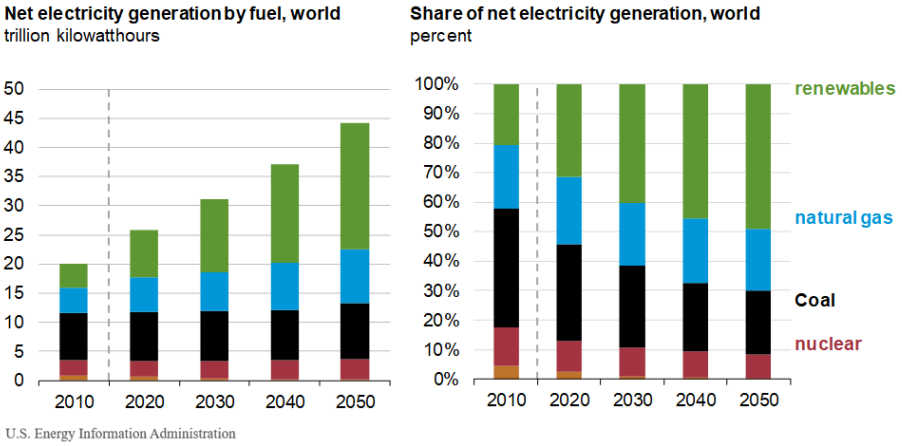

Fig. 1.1: Worldwide net electicity generation projection, 2010-2050. Source: [1].

where the solar PV has the global capacity of 627 GW in the same year [2]. Fig. 1.2 depicts that the solar PV was added globally around 115 GW, which had the share of 57%, and the wind power was added around 60 GW for 30% [2]. Compared with the solar energy, the wind power generation played a vital role in the decarbonization of global warming and shaping the supply chain of energy, accounting for nearly half of the global renewable energy power generation growth in 2015.

Although wind energy accounts for a considerable proportion of today's renewable energy resources, the saturation of onshore wind farms posed a challenge to the growth of wind energy from 2015 to 2018. Thus, the trend of wind power plant construction has then developed from onshore to offshore, where the 2019 annual global wind power market report depicts that in 2015, the EU's onshore market decreased 7.8%, while the offshore installed capacity had doubled. Offshore wind power plants (WPPs) replace onshore WPPs, which maintain the growth momentum of wind energy [5], where the prediction of the installation capacity of offshore WPPs will surpass 20 GW in 2025 and 30 GW in 2030 as shown in Fig. 1.3 [4]. Whether it is solar PV generation or wind power generation, these two kinds of renewable energy resources require generally power converters interface to connect to the power grid. Thus, the demand for power electronic-interfaced renewable energy resources has steadily increased. In Denmark, due to its high latitude, the total solar irradiance is lower than the subtropical regions. Hence, the solar power capacity (3.7%) is much lower than the wind power capacity (70.2%) in the renewable energy based electricity generation in 2017 [6]. Furthermore, due to the high proportion of wind energy in Denmark's renewable energy and the increasing proportion of offshore WPPs, the offshore WPP has been selected as the

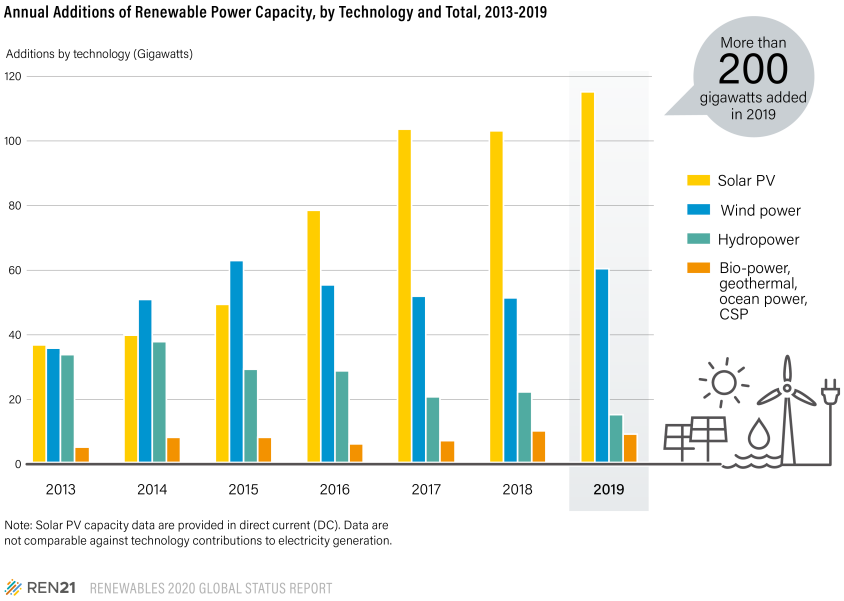

Fig. 1.2: Annual Additions of Renewable Power Capacity, by Technology and Total, 2013-2019. Source: [2].

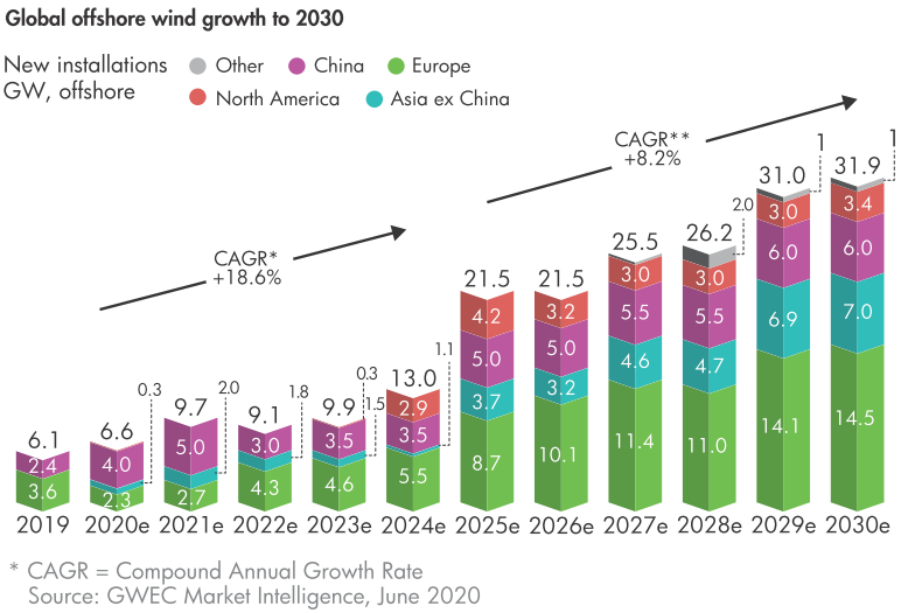

Fig. 1.3: Prediction of global offshore wind growth in GW, 2019-2030. Source: [4].

focus of this Ph.D. project.

Even though the power-electronic-based renewable energy resources bring economic and environmental benefits [7], a large number of power electronic converters in the power system brings also challenges. Since the dynamics of controllers in power electronic converter have multiple time scales, the power electronic converters can introduce not only high-frequency voltage and current harmonics into the grid that cause the power quality and system stability challenges [8, 9], but also the oscillations in a wide frequency range because of the higher control bandwidth of the converters compared with the electrical machines generators used in the conventional power grid [10, 11]. Due to the increased complexity of the system, it is a challenge for modeling and analysis of dynamics in the large-scale power electronic based power system in order to ensure the system stability. Thus, to make a successful transition from a conventional, centralized, synchronous generator based power system to a decentralized distributed, power electronic based power system, the interactions between multiple paralleled power converters and their influence on power system stability must be understood and addressed.

1.1.1 System Stability Analysis in Power Electronic Based Power Systems

For the power system stability with dominant power electronics, the stability has recently been re-categorized in four groups [12], which are synchronization stability, frequency stability, harmonic stability, and voltage stability. In these stability categories, the synchronization stability, frequency stability, and voltage stability can be further divided as small-signal and large-signal stability problems, where the large-signal stability problems are caused by large disturbances, e.g. grid faults, drastic load changes, power generation units tripping, which require several models to handle different abnormal conditions. When instability occurs and causes over-current or over-voltage in the system, the protection components are activated to protect the interface voltage source converters (VSCs) in the system, which forces VSCs to become disconnected and leads to an unreliable power system [13]. Yet, the tripping of VSC is not only caused by large disturbances but also the small-signal stability problems. Since the dynamics of VSCs are broad time-scale and frequency-coupled, the interaction between multiple VSCs and the grid impedance may also cause the instability [14–18]. , which is defined as the harmonic stability problem in [10]. Thus, this project focuses on harmonic stability of grid-connected converters in large-scale power electronic based power systems.

In the meantime, the system-level harmonic stability analysis for power electronic based power systems is achieved by using aggregated models and reduced-order models, which were developed to be applied for synchronous

generator based power system [19]. Therefore, even if the aggregated model in [19] can preserve the frequency characteristics of the critical modes, but it has also introduced significantly different values of damping to the other modes compared with the results obtained from the full-state detailed model [20]. For certain operating conditions, the damping ratio may even become negative, which inaccurately evaluate the stability conditions. Thus, the existing aggregated models based on the aggregating of synchronous generators are not accurate enough to describe the power-electronics based power system.

For the stability analysis of grid-connected VSCs, there exist two kinds of analytic methods based on the average small-signal model, which are the state-space-based stability analysis method in the time domain and the impedance-based stability analysis method in the frequency domain [10]. The state-space method has been widely implemented for the synchronous generator based power system. It has also been implemented in the grid-connected VSCs stability analysis, and it is based on the eigenvalue analysis, where the eigenvalues of the state matrix are the poles of the characteristic equation of system indicating the system stability, i.e., if one of the poles locates in the right-half plane of complex plane, the system is unstable. Within the specified frequency range, the critical states can be distinguished from the eigenvalues of the state matrix by the participation factors, where the poles movement can be predicted with the change of the parameters through sensitivity analysis [21,22]. However, when analyzing the states of the multiple-paralleled-VSCs system, even if the poles movement can be observed when the parameters in the controller are adjusted, the states are usually coupled, which are then impossible to distinguish in the analysis [23].

Differing from the state-space model methods, which require detailed information about the VSCs, the impedance-based stability analysis approaches derive the impedance-ratio at the point of interest in the system, based on which, the Nyquist stability criterion is then used to evaluate the system stability. Thus, the VSCs can be treated as "black box" models, and the impedance-based methods have guaranteed the effectiveness in analyzing the stability in multiple-paralleled-VSCs systems [18,24]. Yet, the impedance-based stability analysis method can only provide the qualitative information about the system stability, i.e. whether the system is stable or unstable, but it fails to give the quantitative information about how the parameter changes in the VSC controller affect the stability condition.

Research Gap 1 (Supplement to existing system stability analysis methods)
When analyzing large-scale power electronic based power systems, either using state-space modeling methods or impedance-based modeling methods face their respective challenges, where the state-space models of the

systems have high dimension, causing complex stability evaluation, but the impedance-based stability analysis method lacks the quantitative information about how to improve the system stability. Therefore, to use one's strengths to compensate for the other's shortcomings may benefit both in an "integrated" modeling approach.

1.1.2 Modeling of Grid-Connected VSCs

Due to the multi-timescale control dynamics of VSCs, the harmonic instability caused by the VSC-grid interaction or VSC-VSC interaction spread across a wide frequency range [24]. These harmonic instabilities phenomena can be categorized into the frequency-decoupled resonances at harmonic frequencies and the sideband (frequency-coupled) resonances around the grid fundamental frequency [10].

The main cause of harmonic resonances in the VSC-grid interaction is the inner current control loop of the VSC, where the time delay of the digital control system plays an important role that introduces the negative damping close to the resonance frequencies of passive filters and grid impedance [25, 26]. The inner current control loop has symmetric dynamic either in the dq-frame (synchronous reference frame) or the $\alpha\beta$-frame (stationary reference frame), the dynamic can be described with two single-input single-output (SISO) transfer functions or one complex transfer function [25, 27]. Then, based on the Nyquist stability criterion, the resonance frequency can be readily identified in Bode plots.

However, for the sideband resonances of the fundamental frequency, which are caused by the asymmetric dq-frame dynamics of VSC, e.g. the phase-locked loop (PLL) [11, 28–32], or the outer power control loops like the dc link voltage control loop [33, 34], or the alternative voltage magnitude control loop [35]. Unlike the case of harmonic resonance, the negative damping is not introduced symmetrically on the d-axis and q-axis but only on the d-axis or q-axis. Thus, the sideband resonances cannot simply be modeled by SISO transfer functions [27]. To capture these asymmetric control dynamics, the multiple-input multiple-output (MIMO) transfer function matrices are needed to characterize the frequency-coupling dynamics [11, 32, 33]. Many MIMO impedance models have been reported, where they can be categorized according to the used reference frame, i.e. the dq-frame impedance matrices [28–30, 34] and the $\alpha\beta$-frame impedance matrices [11, 31–33]. In [11], by clearly revealing the mathematical relationship between the two reference frame impedance matrices, it is proved that the two impedance matrices have the same stability implication.

To be noticed, both impedance matrices are MIMO systems, which require using the generalized (multivariable) Nyquist stability criterion to predict the

system stability. Instead of plotting the impedance-ratio at the point of interest in the system, the Bode plots of the eigenvalues of the MIMO return-ratio matrix were plotted to identify resonance frequencies of the marginally stable system. In [31], the off-diagonal elements in the MIMO 2×2 impedance matrix are discarded due to the magnitudes of off-diagonal elements are far less than the diagonal elements in the impedance matrix. The research in [31] then claims the MIMO impedance matrix can be simplified as two SISO impedances transfer functions in the $\alpha\beta$-frame, so called the sequence-domain impedance model. Since the off-diagonal terms are discarded, the system stability has been analyzed with two return ratio transfer functions. However, this simplification implies that the frequency-coupling dynamics are not considered, which results in an inaccurate stability prediction [11, 32, 33]. To investigate the interaction between the grid-connected VSC and grid impedance, the modeling method in [35] has considered the controllers in large. Yet, the model dedicates to characterize the influence of controller parameters to the overall stability through the common characteristic equation of the system, where the grid impedance appears in both the denominator and numerator of the characteristic equation. Thus, it can only provide little insight into how the grid impedance affect the system stability.

Research Gap 2 (Revealing the VSC-grid interaction)
Due to the asymmetric control dynamics of VSC, the use of generalized Nyquist stability criterion for the MIMO system cannot be avoided in [35]. To apply the generalized Nyquist stability criterion, the eigenvalues of the system MIMO return-ratio matrix must be obtained. Since the grid impedance is hidden in the return-ratio matrix of system, the VSC-grid interactions can only be implicitly exposed. The method can clearly reveal the influence of grid impedance to the stability is lacking.

1.1.3 Reduced-Complexity Model of Multiple Paralleled Grid-connected Converters

To reduce the modeling complexity of a large system with multiple paralleled grid-connected VSCs, the state-space based analysis methods generally use reduced-order models, where the eigenvalues of its state matrix represent the poles of system. The critical modes can be identified from the eigenvalues of state matrix according to their damping ratios. Then, the relevant states and irrelevant states can be distinguished using the participation factors of state matrix, which is named as the selective modal analysis (SMA) in [36, 37]. In the research of [38], the method reduces the order of the state-space model of the HVDC (High-voltage, direct current) Light system, which is based on the VSC technology, from 7 states to 2 subsystems of "slow" and "fast" dynamics according to different time-scales with 4 states, respectively. However, there

is no specific guidance for the transition between "slow" and "fast" subsystems. Thus, when analyzing the coupled "slow" and "fast" dynamics, the full-state-space model is still required. To avoid removing influential "fast" states when analyzing the "slow" dominant states, the research in [39] proposes a so-called "Peel-off and add-back" method, which firstly separates the "slow" and "fast" subsystems according to the bandwidth of different control loops, e.g. the inner current control loop and harmonic filters are "fast", where the outer control loops and dc link capacitors are "slow". Yet, when the states in "fast" subsystem with the lowest bandwidth are close to the states in "slow" subsystem with the highest bandwidth, the reduced-order model without considering these low bandwidth states in "fast" subsystem may lose accuracy. Thus, the order of the "fast" subsystem is further reduced by defining a critical frequency boundary related to the highest bandwidth in the "slow" subsystem. To that end, the states in the "fast" subsystem below the critical frequency are preserved and are added back to the "slow" subsystem to improve the accuracy of reduced-order model. Yet, this method can be used for a given and less changing system because once there is a change in the system, the whole progress of "Peel-off and add-back" is needed to be performed again. For the reduced-order model based on the state-space model, the challenge is to clearly distinguish states at different time scales since the state-space model is time-domain model.

In contrast, the impedance-based model has no "state" to be simplified, and it is a frequency-domain model, which can preserve the dynamics across wide frequency range.

Research Gap 3 (Frequency dependent reduced-complexity model for multiple paralleled grid-connected converters)
The challenge to obtain a reduced-complexity model for the state-space modeling method is to clearly distinguish the relevant states and irrelevant states according to the different time-scales. Since the impedance-based model is modeled in the frequency-domain, it can preserve the multi-time-scale dynamics, which makes the impedance-based model suitable for the system with multiple paralleled grid-connected converters. Yet, systematic methods to derive the reduced-complexity model for the impedance-based modeling method is missing.

Compared with the SMA used in the state-space based analysis method, the nodal admittance matrix of the power system network is used in [40, 41] to identify the critical resonances for the conventional power system, which is called the harmonic resonance mode analysis (RMA). The resonances can be identified through the frequency of the nodal admittance matrix close to the singular points with the eigenvalue of the nodal admittance matrix [40]. In order to investigate the impact on the network component parameters to the critical mode, the modal sensitivity analysis was introduced in [41]. Thus,

the RMA was lately applied to various multiple-VSC power systems, e.g. in railway networks [42], in microgrids [43], and in wind power plants [44]. However, these studies merely use RMA with simplified models of VSCs. The resaerch in [44] has excluded the dynamics of controllers by considering the VSCs as harmonic sources. The researches in [42, 43] have considered the dynamics of the current control with the simplified SISO transfer functions, where they neglect the dq-frame asymmetrical control dynamics of the output power loops and of the PLL, which may imply inaccurate damping conditions.

Research Gap 4 (Improved RMA for large-scale power electronic power systems)
The SMA is a powerful design-oriented tool for state-space modeling methods since it can quantitatively define the influence of control parameters on states in the state matrix. Therefore, the concept has been adopted as RMA for the impedance-based modeling methods. However, the existing RMA researches were used in the conventional power systems without considering the control dynamics of VSC. Thus, if such dynamics of VSC are not included, the method is not sufficient for the large-scale power electronic based power system analysis yet and should be included.

1.1.4 Aggregated Model for the Group of VSCs in Renewable Energy Resources

The existing aggregated models of WPPs deal with the aggregation of a WPP by considering the equivalent of the connection lines of the turbines, and the equivalent power production of the wind power plant [19, 20]. Yet, the output power from all wind turbines may not be the same all the time, and the length, type of the cables will not be the same either [45].

In [46], the aggregated model simplifies the whole WPP as one single wind turbine, which assumes that the output of WPP contains only fundamental frequency, ignoring harmonics, switching performances, and the mutual interactions between converters. However, the resonances caused by the control of the grid-connected VSCs are not monotonous, which are the frequency-coupling resonances [47, 48]. Thus, the resonances might appear in a wider frequency range which the monotonous aggregated model may not be sufficient for the power electronic based power system.

Research Gap 5 (Modularity, scalability, and flexibility of aggregated model)
The existing aggregating models of WPPs generally use the assumptions of identical wind turbines, same operating points, cables, which is not the case in practical systems. Thus, the process of deriving aggregated model

must consider the modularity of wind turbines and cables, scalability, flexibility, and heterogeneity.

1.2 Project Motivation

As discussed in the previous sections, several research gaps arise when analyzing the large-scale power electronic based power systems, where the main challenges are the VSC-grid and VSC-VSC interactions because of the dynamic characteristics of VSCs are multi-timescale and asymmetrical.

Firstly, to achieve the goal of analyzing the multi-timescale dynamics of VSC, the impedance-based modeling method is endorsed since it is the frequency-domain model that comprises multi-timescale dynamics. The instability phenomena caused by the dynamic interactions, between single VSC and the grid impedance or among multiple VSCs, must be investigated and properly analyzed based on the impedance-based models. For VSC-grid interactions, the grid impedance can be assumed containing only passive components, which involves only two quadrants in the complex plane. Thus, the attention can be focused on the MIMO control dynamic of VSC, and how the grid impedance affects the stability condition. Then, to analyze the VSC-VSC interactions, all four quadrants in the complex plane must be considered, which is generalized from the previous VSC-grid interaction.

Secondly, to investigate the influence of control parameters in VSCs on harmonic instability in large-scale power electronic power systems, a systematic method must be realized to derive the nodal admittance matrix for RMA, which includes the asymmetric dynamics of the VSC embedding multiple MIMO impedance models. Then, how to extend the current RMA method used in conventional power systems to large-scale power electronic power systems must be resolved.

Finally, there are numerous VSCs, passive filters, transmission line cables, and transformers in the large-scale power electronic based power system, the frequency- dependent aggregated model is required to accurately assess the stability conditions. However, the operating conditions of VSCs may change over time, where the modularity of aggregated model must be adapted to different operating conditions. The scalability of the aggregated model is also important for evaluating the influence from other equipments, such as battery system and the power-to-X conversion technologies. At last, the flexibility of the aggregated model is also of value to temporally disconnect part of the system for fault conditions.

The main motivation of this Ph.D. study is to have a better understanding of the dynamic behavior of large-scale power electronic based power system using improved analysis methods.

1.3 Project Objectives and Limitations

1.3.1 Research Questions and Objectives

With the above mentioned challenges, the overall research hypothesis of this Ph.D. study can be summarized as the following research question:

"How to provide a design-oriented approach to model and analyze multiple paralleled grid-connected voltage source converters with asymmetric and multi-timescale control dynamics in scalable power-electronic-based power system?"

To answer this question, the modeling method targeting the power-electronic-based power system should be general, and capture the frequency-coupling dynamics, as well as the multi-time scale dynamics in the converters. Even if the complexity of the system assembled with a number of converters is reduced by the aggregated model, the aggregated model should still preserve the necessary information for stability assessment. Based on the overall research question and the research gaps in the introduction, multiple sub-questions are formulated as follows:

- How should the MIMO impedance matrix of converters be interpreted, and is it possible to reconstruct the MIMO impedance matrix into SISO sub-systems for stability analysis to avoid using generalized Nyquist stability criterion?
- How to apply impedance-based method for different connections of large-scale VSC-based systems, and when instability occur, how to distinguish the critical converter in the system?
- What should be considered when analyzing the resonance instability caused by the VSC dynamics, and how to analyze the impact of the control parameters in VSC to the resonance?
- How to aggregate the impedance models of the large-scale power electronic based power system that can adapt various operating conditions of converters?

With those research questions, the PhD project can be divided into the following objectives:

Develop MIMO system stability analysis method for a single-VSC system

As mentioned previously, several researches have been reported for analyzing the stability of MIMO system. However, the use of generalized Nyquist criterion cannot be avoided when considering the off-diagonal terms in the MIMO impedance matrix. In the large-scale power electronic based power system, the dimension of the MIMO system will increase dramatically. Thus,

a proper method should be developed considering the large-scale utilization possibility. The effectiveness of the proposed method will be validated experimentally with a three-phase grid-connected VSC considering the grid impedance.

Identify the critical VSC in a marginally stable multiple-VSC system

For the multiple-VSC system, not only the VSC-grid interaction but also the VSC-VSC interaction should be considered, where the identification of the critical VSC is crucial for enhancing the system stability especially in marginally stable power system, which will be addressed in this project. To validate the system stability in large-scale power electronics based power system, a simple multiple-bus system will be considered, which has a reasonable number of VSCs and can also be used for experimental validation.

Resonance mode analysis and sensitization in the multiple-VSC system

The existing resonance mode analysis method was developed for the passive LC networks. Thus, the researches, which implement the method in the multiple-VSC system, usually overlook the dynamics of the VSC or just consider only the simplified SISO dynamics. Therefore, it is necessary to revisit the resonance mode analysis method adapting MIMO dynamics of VSC and develop an improved version specifically for power electronic based power system. To validate, the same multiple bus system in the previous sub-objective will be used, and the resonance mitigation will be achieved.

Frequency dependent aggregated model for large-scale power electronics based power system

Take a large-scale power electronics based power system, such as offshore wind power plant, for example, the existing aggregated models generally use the assumptions of identical wind turbines, cables, where the accuracy is questionable. In addition, the multi-timescale, frequency-coupling control dynamics of wind turbines may impact the system in a wide frequency range. Thus, the process of deriving the frequency dependent aggregated model must consider the modularity of wind turbines and cables, the scalability of the potential auxiliary system, and the flexibility for various operating conditions. To prove the effectiveness of this work, a practical offshore wind farm, i.e., Anholt Offshore WPP, will be studied, and system with high complexity will be considered.

1.3.2 Limitations

In this project, the study focuses on the grid-following VSCs, where the other variations of grid-connected converters, such as, grid-forming converters and current source converters are not considered. For the control of grid-

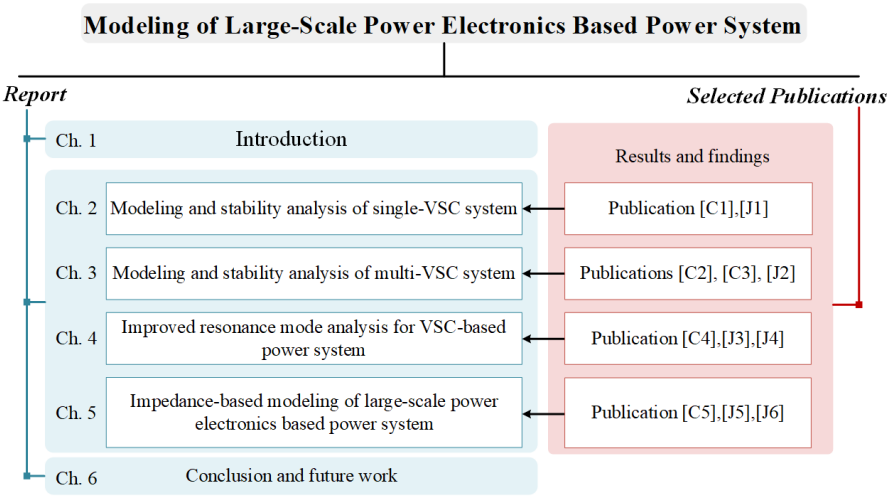

Fig. 1.4: Report structure and how the selected publications link to the chapters.

following VSCs, this project discusses only the inner current control loop and the phase-locked loop. Thus, the impact of MIMO asymmetric control dynamic in the stability analysis is contributed only with the phase-locked loop, where the dynamics of other outer control loops, e.g. dc-link voltage control, ac voltage control, active and reactive power loop are neglected.

For the stability analysis in the multiple-VSC system, only the small-signal stability is studied, where the large-signal/transient stability issues, e.g. grid fault, is not discussed. In the experimental validation, the grid impedance is represented by inductors, and therefore a short transmission line model is used in the simulations and theoretical deviation. On the other hand, the medium length transmission lines (80 km to 200 km) are considered in the system-level study of wind power plant study. Yet, due to the limited information, the length and the type of transmission lines, the parameters of the step-up transformers, and the control parameters of wind turbines are presumed in the system-level wind power plant simulations.

1.4 Thesis Outline

The outcomes and results of this Ph.D. project are summarized in the form of a Ph.D. thesis based on the collection of papers. The thesis can be separated into two parts, the report part and the selected publications part, where the link between chapters in the report and the papers in the selected publications is shown in Fig. 1.4. The report consists of five chapters to conclude the Ph.D.

study as follows:

Chapter 1: Introduction

The background and motivation of this Ph.D. study are given, where the state-of-art and the research gaps are clarified. Then, the research questions are defined based on the research gaps, which further defines the objectives of this Ph.D. project. Finally, the outline of each chapter and the list of publications are given.

Chapter 2: Modeling and stability analysis of single-VSC system

Impedance-based modeling methods on the frequency-coupling dynamics are presented in this chapter, where the difficulties of using the generalized Nyquist stability criterion are explained. The modeling method based on the two-port network theory is then introduced in details, which can simplify the MIMO system into two SISO sub-systems. Thus, instead of using generalized Nyquist stability criterion, the conventional stability analysis tools, e.g. Bode plot, Nyquist stability criterion, can be used. Then, the advantages and disadvantages are discussed with other modeling methods. By selecting different test cases, including different values of grid impedance, operating conditions of VSC, and control parameters, the theoretical derivations are validated with both simulations and experimental results.

Chapter 3: Modeling and stability analysis of multi-VSC system

For using the Nyquist stability criterion in the impedance-based stability analysis methods, prior knowledge of the number of open-loop right-half-plane poles in the impedance-ratio is necessary. Thus, when analyzing the multi-VSC system, a proper partitioning that separates the system into multiple impedance-impedance or impedance-admittance subsystems is required, which needs prior knowledge of the system. Therefore, a SISO reflection coefficient stability criterion for multi-VSC system is presented, which is proven unaffected by the open-loop right-half-plane poles of the impedances. Therefore, the system pre-partitioning to make the subsystem stable is unnecessary for system stability analysis.

Chapter 4: Improved resonance mode analysis for VSC-based power system

To conduct the resonance mode analysis for VSC-based power system, the nodal admittance matrix embedding the MIMO impedance matrices is required, which is a method using the graph theory to systematically derive the nodal admittance matrix. Then, the resonance mode analysis method is revisited, where it is found that to solely describe a resonance requires three factors: 1) the resonance magnitude, 2) the resonance frequency, and 3) the quality factor of the resonance. The investigations of the magnitude [41] and frequency [49] to the resonance have already been covered. However, the quality factor of the resonance had been overlooked in the synchronous-

generator-based power system, which is proven indicating the system is active or passive that is crucial in the VSC-based power system. Thus, the concept of the sensitivity of modal quality factor is presented for VSC-based power system, where the impact of the control parameters in VSCs to the resonance can be quantitatively defined, which is further verified with experimental results.

Chapter 5: Impedance-Based Modeling of Large-Scale Power Electronics Based Power System

The nodal admittance matrix derived in the previous chapter has embedded the MIMO impedance matrices of VSCs, which is naturally frequency-dependent, and it represents a multi-port network. Thus, the aggregated model for large-scale power electronic based power system is derived by reducing the number of ports in the multi-port network by matrix operations on its four submatrices. Then, the aggregated model can be analyzed by studying the eigenvalues or singular values of its submatrices, where the sensitivity indices presented in the previous chapter can also be used. A test case with the practical layout of the wind power plant is studied, which shows the modularity, scalability, and the flexibility of the aggregated model.

Chapter 6: Conclusion and future work This chapter summarizes the main findings and conclusion of the thesis, which also discusses the topics for the future work.

1.5 List of Publications

The research outcomes of the Ph.D. project have been disseminated in forms of publications: journal papers, and conference proceedings, as listed below. Nonetheless, only a selected few (e.g., Cx, and Jx) are summarized and considered within this Ph.D. dissertation, which is based on a collection of papers. A complete list of publications during this Ph.D. study is as follows:

Publications in Referred Journals

[J1] **S. -F. Chou**, X. Wang, and F. Blaabjerg, "Two-Port Network Modeling and Stability Analysis of Grid-Connected Current-Controlled VSCs," in *IEEE Trans. Power Electrons.*, vol. 35, no.4, pp. 3519-3529, April 2020.

[J2] **S. -F. Chou**, X. Wang, and F. Blaabjerg, "Reflection Coefficient Stability Criterion for Multi-Bus Multi-VSC Power Systems," in *IEEE Access*, vol. 8, pp. 111186-111199, 2020.

[J3] **S. -F. Chou**, X. Wang, and F. Blaabjerg, "Frequency-Domain Modal Anal-

ysis for Power-Electronic-Based Power Systems," in *IEEE Trans. Power Electrons.*, vol. 36, no. 5, pp. 4910-4914, May 2021.

[J4] **S. -F. Chou**, X. Wang, and F. Blaabjerg, "Use of Modal Quality Factor for Resonance Mode Analysis in VSC-Based Power Systems," under review in *IEEE Journal Emerg. Sel. Topics Power Electron.*, 2020.

[J5] **S. -F. Chou**, X. Wang, and F. Blaabjerg, "Frequency-Dependent Aggregated Model for Power Electronic System," to be submitted to *IEEE Trans. Power Electron.*, 2021.

[J6] **S. -F. Chou**, X. Wang, and F. Blaabjerg, "Impedance-Based Modeling and Analysis Process for VSC Dominant Power System," to be submitted to *IEEE Journal Emerg. Sel. Topics Power Electron.*, 2021.

- F. Hans, W. Schumacher, **S. -F. Chou**, and X. Wang, "Passivation of Current-Controlled Grid-Connected VSCs Using Passivity Indices," in *IEEE Trans. Industrial Electron.*, vol. 66, no. 11, pp. 8971-8980, Nov. 2019.

- L. Harnefors, X. Wang, **S. -F. Chou**, M. Bongiorno, M. Hinkkanen, and M. Routimo, "Asymmetric Complex-Vector Models With Application to VSC–Grid Interaction," in *IEEE Journal Emerg. Sel. Topics Power Electron.*, vol. 8, no. 2, pp. 1911-1921, June 2020.

- F. Hans, W. Schumacher, **S. -F. Chou**, and X. Wang, "Design of Multifrequency Proportional–Resonant Current Controllers for Voltage-Source Converters," in *IEEE Trans. Power Electron.*, vol. 35, no. 12, pp. 13573-13589, Dec. 2020.

- W. Liu, F. Blaabjerg, D. Zhou, and **S. -F. Chou**, "Modified Instantaneous Power Control with Phase Compensation and Current-limited Function under Unbalanced Grid Faults," in *IEEE Journal Emerg. Sel. Topics Power Electron.*, 2021.

Publications in Referred Conferences

[C1] **S. -F. Chou**, X. Wang, and F. Blaabjerg, "Stability Analysis of Grid-connected VSCs Based on Two-port Network Theory," *IEEE Applied Power Electronics Conference and Exposition (APEC)*, Anaheim, CA, USA, 2019, pp. 1165-1172

[C2] **S. -F. Chou**, X. Wang, and F. Blaabjerg, "Extensions to Two-Port Network Modeling Method and Analysis of Multiple-VSC-Based Systems," *20th*

Workshop on Control and Modeling for Power Electronics (COMPEL), Toronto, ON, Canada, 2019, pp. 1-8.

[C3] **S. -F. Chou**, X. Wang, and F. Blaabjerg, "Stability Analysis of Grid-Connected VSCs Based on S-parameters and Reflection Coefficient," *IEEE Energy Conversion Congress and Exposition (ECCE)*, Baltimore, MD, USA, 2019, pp. 5171-5178.

[C4] **S. -F. Chou**, X. Wang, and F. Blaabjerg, "Subsynchronous Resonance Analysis in Multi-Bus Multi-VSC Power System Based on Two-Port Network Modeling Method," *IEEE Energy Conversion Congress and Exposition (ECCE)*, Detroit, MI, USA, 2020, pp. 5696-5702.

[C5] **S. -F. Chou**, X. Wang, and F. Blaabjerg, "An Aggregated Model for Power Electronic System Based on Multi-Port Network Reduction Method," *IEEE 21st Workshop on Control and Modeling for Power Electronics (COMPEL)*, Aalborg, Denmark, 2020, pp. 1-6.

- **S. -F. Chou**, X. Wang and F. Blaabjerg, "Passivity-based LCL Filter Design of Grid-Connected VSCs with Converter Side Current Feedback," *International Power Electronics Conference (IPEC-Niigata 2018 -ECCE Asia)*, Niigata, 2018, pp. 1711-1718.

- **S. -F. Chou**, X. Wang, H. Matsumori, T. Shimizu and F. Blaabjerg, "Linearized Modeling and Controller Design of the Nonlinear Inductors in $\alpha\beta$-frame," *20th European Conference on Power Electronics and Applications (EPE'18 ECCE Europe)*, Riga, 2018, pp. P.1-P.9.

- **S. -F. Chou**, X. Wang and F. Blaabjerg, "A Fractional-Order Model of Filter Inductors within Converter Control Bandwidth," *IEEE Electronic Power Grid (eGrid)*, Charleston, SC, 2018, pp. 1-6.

Chapter 2

Modeling and Stability Analysis of Single-VSC System

2.1 Background

In the renewable energy resources, the voltage source converters (VSCs) have been generally used as grid-interfaced converters, which rapidly increases the penetration level of power electronics in the modern power system [7]. The renewable energy penetration level can be defined as the fraction of energy produced by renewables to the total energy production, where the wind energy covered 16% of Europe energy demand in 2020, and it even covered 48% of Denmark energy demand in the same year [50]. With VSCs in the power system, their multi-timescale control dynamics tend to bring the harmonic instability across a wide frequency range [24]. In respect to distribution of the resonances in frequency spectrum [10], the resonances can be categorized into frequency-decoupled resonances at harmonic frequencies and frequency-coupled sideband resonances around the grid fundamental frequency.

The harmonic resonances, which are caused by symmetric dynamic in the dq-frame or the $\alpha\beta$-frame, e.g. inner current control loop, can be analyzed as two SISO transfer functions or one complex transfer function using the Nyquist stability criterion [25, 27]. However, the sideband resonances of the fundamental frequency caused by the asymmetric dq-frame dynamics of VSC, e.g. the PLL [11, 28–32], or the outer power control loops [33–35], require the MIMO transfer function matrices to capture and to analyze the frequency-coupling dynamics [11, 32, 33]. Many MIMO impedance models

have been reported and reviewed in *Chapter I*, which can be categorized as the dq-frame impedance matrices and the $\alpha\beta$-frame impedance matrices. In [11], the mathematical relationship between two reference frame impedance matrices is revealed. In order to analyze the large-scale power electronic based power systems, the $\alpha\beta$-frame impedance matrices have the advantage over the dq-frame impedance matrices since the

. Thus, the $\alpha\beta$-frame impedance models are selected to use in this Chapter. Yet, the MIMO impedance models in the $\alpha\beta$-frame lead to a MIMO matrix form of the return-ratio obtained from VSC impedance matrix and grid impedance matrix, which requires the generalized Nyquist stability criterion for stability analysis.

To derive the analytic equations of eigenvalues of the MIMO matrix is impractical, and thus, it is difficult to analyze how the system parameters, e.g. grid impedance, affect the system resonance. To solve the difficulties of analysis caused by the MIMO impedance models, this chapter describe the MIMO system with two-port network theory and then derive the characteristic equation of the MIMO system. Based on that, two admittance ratios can be formed from the characteristic equation, which clearly distinguish the influences from VSC impedance model or grid impedance.

2.2 Two-Port Network Modeling with Y-Parameter

Since the frequency-coupled dynamic of the VSC needs to be modeled as a transfer function matrix, and will be used in the multi-VSC system in Chapter 3, the $\alpha\beta$-frame impedance model of a current-controlled grid-connected VSC with the synchronous reference frame phase-locked loop (SRF-PLL) is briefly introduced. First, the dq-frame impedacne model can be derived using the single-line diagram of three-phase grid-connected current-controlled VSC like shown in Fig. 2.1, where a stiff dc voltage source, v_{dc}, is connected at the dc side to omit the dynamic of dc link voltage controller and to focus on the asymmetric dynamic of SRF-PLL. At the ac side, the VSC connects to the grid voltage, v_g through an LCL filter, L_o, C_g, and L_g. Since the capacitor voltage, v_c, of C_g is measured as the input of SRF-PLL for the grid synchronization, and the inductor current of L_o, i_c is measured for the ac current controller, the voltage at point of common coupling (PCC) is defined as v_c, where the LC-filter, C_g and L_g, form the grid impedance in the study. C_g is also used as the filter capacitor of the VSC so it has a constant value. However, the value of L_g depends on different grid conditions.

The current controller is implemented in the dq-frame with the current commands $i_{ref,dq}$, which is affected by the dynamics of the SRF-PLL through the Park transformation and inverse Park transformation. Accordingly, the small-signal block diagram of the current control loop with the dynamic of

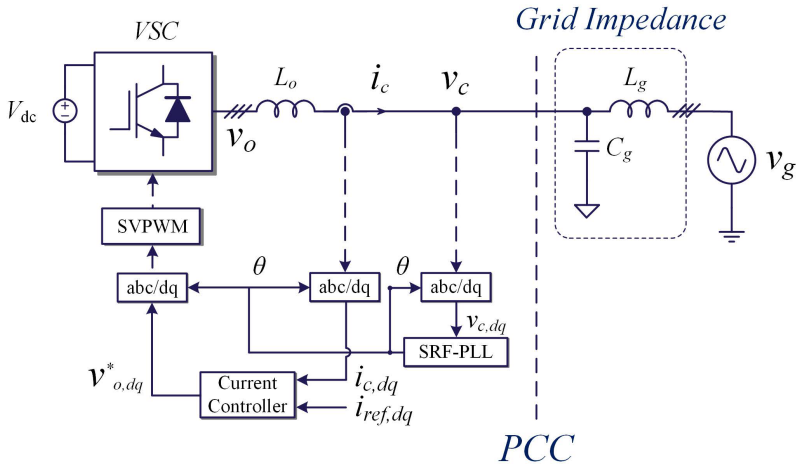

Fig. 2.1: Single-line diagram of a three-phase grid-connected VSC with current control loop and SRF-PLL. Source: [J1].

the SRF-PLL in the dq-frame is shown in Fig. 2.2, where the details can be found in [11].

In Fig. 2.2, the blocks with superscript "m" represents the MIMO transfer function matrices, where the $Y^m_{p,dq}(s)$ and $Y^m_{o,dq}(s)$ illustrate the dynamics of L_o, which represent the inductor current dynamic from the PCC voltage, $\Delta v_{c,dq}$, and the output voltage of VSC, $\Delta v_{o,dq}$, respectively.

To be noticed, the matrices $G^m_{c,dq}(s)$ and $G^m_{del}(s)$ are diagonal matrices, where $G^m_{c,dq}(s)$ represents the PI current controller transfer function matrix with the proportional gain K_{cp} and the integral gain K_{ci}, and $G^m_{del}(s)$ represents the delay contributed by the digital computation (T_s) and the pulse width modulation $(0.5T_s)$ [51], and T_s represents the sampling period.

Different from the diagonal matrices, $G^m_{c,dq}(s)$ and $G^m_{del}(s)$, $Y^m_{PLL}(s)$ and $G^m_{PLL}(s)$ represent the asymmetric dynamics of SRF-PLL, where $Y^m_{PLL}(s)$ represents the impact from $\Delta v_{c,dq}$ to the current $\Delta i_{c,dq}$, and $G^m_{PLL}(s)$ denotes the impact from $\Delta v_{c,dq}$ to the output voltage command $v^*_{o,dq}$, which are given as

$$Y^m_{PLL}(s) = \begin{bmatrix} 0 & -H_{PLL}(s)\,V_{c,q} \\ 0 & H_{PLL}(s)\,V_{c,d} \end{bmatrix} \tag{2.1}$$

$$G^m_{PLL}(s) = \begin{bmatrix} 0 & -H_{PLL}(s)\,I_{c,q} \\ 0 & H_{PLL}(s)\,I_{c,d} \end{bmatrix} \tag{2.2}$$

where $H_{PLL}(s)$ is the linearized 2^{nd}-order transfer function representing the small-signal model of the SRF-PLL [25]. Then, the closed-loop output admit-

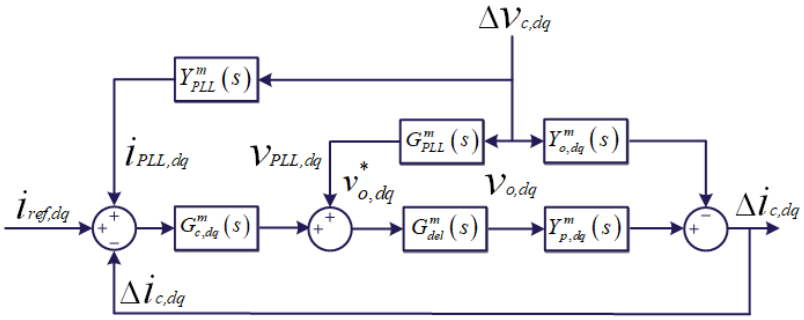

Fig. 2.2: Small-signal block diagram of the current control loop with the effect of SRF-PLL in the dq-frame. Source: [J1].

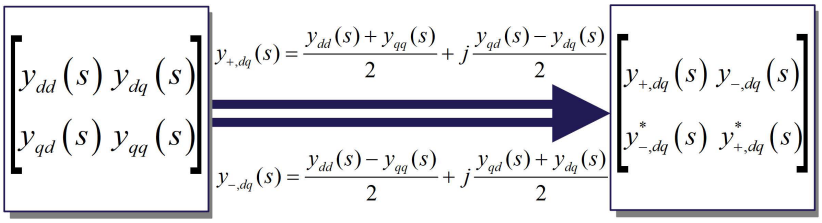

Fig. 2.3: The complex transfer function equivalent of an asymmetric transfer function matrix. Source: [J1].

tance matrix, $Y^m_{cl,dq}(s)$ can be derived as

$$Y^m_{cl,dq}(s) = G^m_{cl,dq}(s)\,Y^m_{PLL}(s) + \left[I^m + T^m_{dq}(s)\right]^{-1} Y^m_{p,dq}(s)\,G^m_{del,dq}(s)\,G^m_{PLL}(s) - \left[I^m + T^m_{dq}(s)\right]^{-1} Y^m_{o,dq}(s) \tag{2.3}$$

where the closed-loop transfer matrix $G^m_{cl,dq}(s)$ and the open-loop gain of the transfer function matrix, $T^m_{dq}(s)$, are given as

$$G^m_{cl,dq}(s) = \left[I^m + T^m_{dq}(s)\right]^{-1} T^m_{dq}(s) \tag{2.4}$$

$$T^m_{dq}(s) = Y^m_{p,dq}(s)\,G^m_{del,dq}(s)\,G^m_{c,dq}(s) \tag{2.5}$$

The $Y^m_{PLL}(s)$ and $G^m_{PLL}(s)$ given in (2.1) and (2.2) are asymmetric matrices, where $Y^m_{PLL}(s)$ and $G^m_{PLL}(s)$ appear at the first and second terms of the right hand side of (2.3). Thus, the $Y^m_{cl,dq}(s)$ results in an asymmetric matrix. In addition, the $Y^m_{cl,dq}(s)$ in (2.3) is a linear time invariant system since its

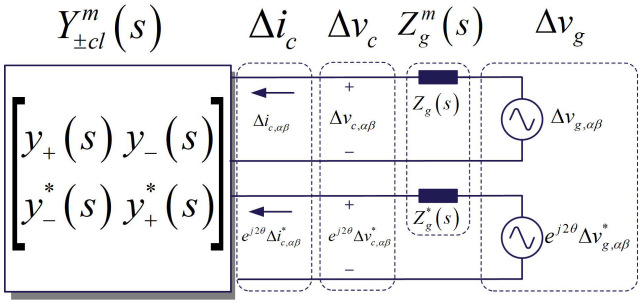

Fig. 2.4: Impedance equivalent circuit of the current-controlled grid-connected VSC in the $\alpha\beta$-frame. Source: [J1].

inputs are real vectors, $\Delta v_{c,d}$ and $\Delta v_{c,q}$, where it is hard to reveal the dynamic couplings between different frequencies in the phase domain. In [52], the transformation between the general real-value transfer function matrix to its complex-vector equivalent has been introduced. It is then realized for the dq-frame impedance matrix in [10, 30] as illustrated in Fig. 2.3, where $y^*_{+,dq}(s)$ and $y^*_{-,dq}(s)$ are the complex conjugates of the complex transfer functions $y_{+,dq}(s)$ and $y_{-,dq}(s)$, respectively. The frequency coupling dynamics caused by the dq-frame asymmetric control loops can then be introduced in the impedance matrix. Furthermore, the frequency translation between the dq- and $\alpha\beta$-frame has been introduced in [11], where the $\alpha\beta$-frame complex-valued impedance matrix revealing the frequency coupling dynamics can be derived as

$$\begin{bmatrix} \Delta i_{c,\alpha\beta} \\ e^{j2\theta}\Delta i^*_{c,\alpha\beta} \end{bmatrix} = \underbrace{\begin{bmatrix} y_+(s) & y_-(s) \\ y^*_-(s) & y^*_+(s) \end{bmatrix}}_{Y^m_{\pm cl}(s)} \begin{bmatrix} \Delta v_{c,\alpha\beta} \\ e^{j2\theta}\Delta v^*_{c,\alpha\beta} \end{bmatrix} \tag{2.6}$$

where the complex-valued impedance matrix of the grid impedance can also be derived by following the same process. Thus, the circuit equation of Fig. 2.1 can be derived as

$$\begin{bmatrix} \Delta v_{c,\alpha\beta} \\ e^{j2\theta}\Delta v^*_{c,\alpha\beta} \end{bmatrix} = \begin{bmatrix} \Delta v_{g,\alpha\beta} \\ e^{j2\theta}\Delta v^*_{g,\alpha\beta} \end{bmatrix} - \underbrace{\begin{bmatrix} Z_g(s) & 0 \\ 0 & Z^*_g(s) \end{bmatrix}}_{Z^m_g(s)} \begin{bmatrix} \Delta i_{c,\alpha\beta} \\ e^{j2\theta}\Delta i^*_{c,\alpha\beta} \end{bmatrix} \tag{2.7}$$

since the dynamic of the grid impedance is symmetric both in the dq-frame and in the $\alpha\beta$-frame, which results in a diagonal impedance matrix $Z^m_g(s)$. Combining equations (2.6) and (2.7), the circuit diagram in Fig. 2.1 can be drawn as the impedance equivalent circuit in the $\alpha\beta$-frame like shown in Fig. 2.4. The circuit in Fig. 2.4 can be reorganized by distributing two grid

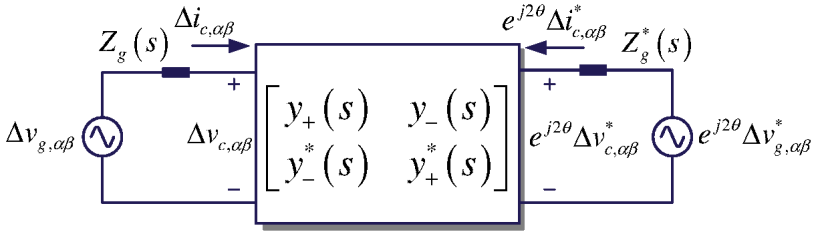

Fig. 2.5: General two-port network representation of the current-controlled grid-connected VSC in the $\alpha\beta$-frame based on admittance matrices. Source: [J1].

impedance terms, $Z_g(s)$ and $Z_g^*(s)$ to the two sides of the VSC admittance matrix, which becomes a general form of the two-port network as shown in Fig. 2.5. The general form of two-port network can be used to derive the electrical relationships between the voltage sources $\left[\Delta v_{g,\alpha\beta} \quad e^{j2\theta}\Delta v^*_{g,\alpha\beta}\right]^T$ and the terminal voltage vector $\left[\Delta v_{c,\alpha\beta} \quad e^{j2\theta}\Delta v^*_{c,\alpha\beta}\right]^T$ or the current vectors $\left[\Delta i_{c,\alpha\beta} \quad e^{j2\theta}\Delta i^*_{c,\alpha\beta}\right]^T$.

2.3 Stability Analysis with Two-Port Network

To show the difference between the two-port network stability analysis method and the conventional impedance-based stability analysis method, the conventional impedance-based stability analysis method is briefly introduced at first. As shown in Fig. 2.4, the grid impedance matrix is cascaded with the VSC admittance matrix, and then, the open-loop transfer function matrix of this MIMO system can be derived from the ratio of the impedance matrices, which is called the return-ratio matrix $L_m(s)$ given as

$$L_m(s) = Z_g^m(s)\, Y_{\pm,cl}^m(s) \tag{2.8}$$

Then, the eigenvalues of $L_m(s)$ can be derived by solving the following equation.

$$\det\left(L_m(s) - \lambda I\right) = 0 \tag{2.9}$$

Thus, by plotting the eigenvalues in the complex plane, the generalized Nyquist stability criterion can be used for the stability prediction. This method analyzes the MIMO system directly, and it has been used for the single-VSC systems [11, 28–34]. However, to derive the return-ratio matrix, all entries in the impedance matrices must be distinguished by analytical derivations or through impedance measurements [53, 54]. Furthermore, the impact of the grid impedance to the system resonance frequency is hidden in the eigenvalues of the return-ratio matrix, which can provide little insight [35].

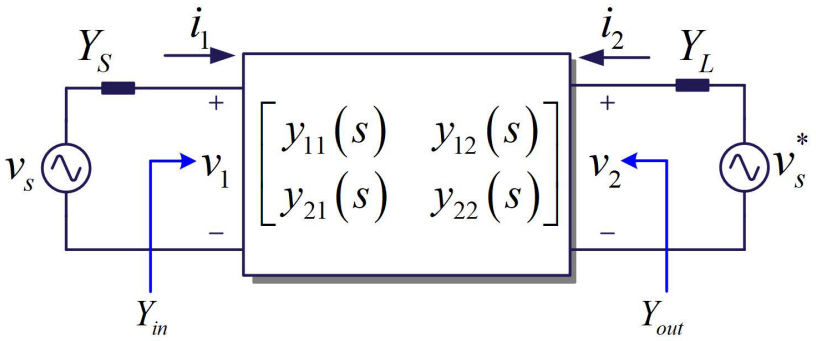

Fig. 2.6: General admittance form of the LTI two-port network model. Source: [J1].

The stability analysis method using two-port network theory is developed to solve this problem, which is based on the active network analysis theory [55]. In Fig. 2.6, a general LTI two-port network model with admittance parameters is given, which connects to two voltage sources, v_s and v_s^*, through two admittance, Y_S and Y_L, respectively. Then, the current dynamics at each port can be analyzed by the superposition principle using the SISO impedances seen from each port, where the details can be found in [J1]. The Norton's equivalent admittance at the Port 1 in Fig. 2.6, Y_{in} can be derived as

$$Y_{in} = \frac{i_1}{v_1} = y_{11} + y_{12}\frac{v_2}{v_1} = y_{11} - \frac{y_{12}y_{21}}{y_{22} + Y_L} \tag{2.10}$$

Thus, the SISO closed-loop gains from v_S to v_1, and v_2 are given as

$$\frac{v_1}{v_S} = \frac{\dfrac{Y_S}{Y_S + y_{11}}}{1 - \dfrac{y_{12}y_{21}}{(Y_S + y_{11})(Y_L + y_{22})}} \tag{2.11}$$

$$\frac{v_2}{v_S} = \frac{v_2}{v_1}\frac{v_1}{v_S} = -\frac{\dfrac{y_{21}Y_S}{(Y_S + y_{11})(Y_L + y_{22})}}{1 - \dfrac{y_{12}y_{21}}{(Y_S + y_{11})(Y_L + y_{22})}} \tag{2.12}$$

where the voltage ratio between v_2 and v_1 is given as

$$G_v = \frac{v_2}{v_1} = \frac{-y_{21}}{y_{22} + Y_L} \tag{2.13}$$

Following the process, the SISO closed-loop gains from v_S^* to v_1, and v_S^* to v_2

can be derived as

$$\frac{v_1}{v_S^*} = -\frac{\dfrac{y_{12}Y_L}{(Y_S+y_{11})(Y_L+y_{22})}}{1-\dfrac{y_{12}y_{21}}{(Y_S+y_{11})(Y_L+y_{22})}} \tag{2.14}$$

$$\frac{v_2}{v_S^*} = \frac{\dfrac{Y_L}{Y_L+y_{22}}}{1-\dfrac{y_{12}y_{21}}{(Y_S+y_{11})(Y_L+y_{22})}} \tag{2.15}$$

These four closed-loop gains, (2.11), (2.12), (2.14), and (2.15), have the same characteristic equation of the system at the denominators, and the common open-loop gain G_L is given as

$$G_L = -\frac{y_{12}y_{21}}{(Y_S+y_{11})(Y_L+y_{22})} \tag{2.16}$$

where it is a SISO transfer function. Therefore, the classical Nyquist stability criterion can be used instead of the generalized Nyquist stability criterion. However, the need of all four elements in the admittance matrix is the same as the conventional impedance-based method and it is challenge to measure all the entries in the $\alpha\beta$-frame admittance matrix. On the contrary, the measurement of the equivalent terminal admittances can be readily obtained [53]. Thus, the SISO closed-loop gains from (2.11) to (2.15) are reformulated as

$$\frac{v_1}{v_S} = \frac{Y_S}{Y_S+Y_{in}} = \frac{\dfrac{Y_S}{Y_{in}}}{1+\dfrac{Y_S}{Y_{in}}} \tag{2.17}$$

$$\frac{v_2}{v_S} = G_v\frac{Y_S}{Y_S+Y_{in}} = G_v\frac{\dfrac{Y_S}{Y_{in}}}{1+\dfrac{Y_S}{Y_{in}}} \tag{2.18}$$

$$\frac{v_1}{v_S^*} = G_v^*\frac{Y_L}{Y_L+Y_{out}} = G_v^*\frac{\dfrac{Y_L}{Y_{out}}}{1+\dfrac{Y_L}{Y_{out}}} \tag{2.19}$$

$$\frac{v_2}{v_S^*} = \frac{Y_L}{Y_L+Y_{out}} = \frac{\dfrac{Y_L}{Y_{out}}}{1+\dfrac{Y_L}{Y_{out}}} \tag{2.20}$$

where

$$G_v^* = \frac{-y_{12}}{y_{11}+Y_S} \tag{2.21}$$

Table 2.1: System parameters for simulations and experiments

Symbol	$V_{g,rms}$	V_{dc}	$I_{ref,d}$	$I_{ref,q}$	f_{sw}	T_s	L_o	C_g	L_g
Value	400 V, 50 Hz	650 V	21.2 A	-2.0 A	10 kHz	100 µs	1.5 mH	15 µF	11.0 mH

Table 2.2: Control parameters for simulations and experiments

Symbol	K_{cp}	K_{ci}	K_{pp}	K_{pi}
Value	7.9 $\mathrm{V\,A^{-1}}$	2742 $\mathrm{V\,A^{-1}\,s^{-1}}$	1.05 $\mathrm{rad\,s^{-1}\,V^{-1}}$	285 $\mathrm{rad\,s^{-2}\,V^{-1}}$

$$Y_{out} = y_{22} - \frac{y_{12}y_{21}}{y_{11} + Y_S} \tag{2.22}$$

Remark (Equivalent admittance-ratio for stability analysis of the MIMO System)
It is shown that the closed-loop gains from (2.17) to (2.20) have an open-loop gain which is equal to either Y_S/Y_{in} or Y_L/Y_{out}, which can be measured from Port 1 and Port 2. Thus, the need of all four entries in the admittance matrix can be avoided for stability analysis.

Thus, to link the admittance ratios, Y_S/Y_{in} and Y_L/Y_{out}, to the circuit in Fig. 2.5, the admittances are given as

$$Y_S = \frac{1}{Z_g(s)} \tag{2.23}$$

$$Y_L = \frac{1}{Z_g^*(s)} \tag{2.24}$$

$$Y_{in} = y_+(s) - \frac{y_-(s)\,y_-^*(s)}{\left(y_+^*(s) + \frac{1}{Z_g^*(s)}\right)} \tag{2.25}$$

$$Y_{out} = y_+^*(s) - \frac{y_-(s)\,y_-^*(s)}{\left(y_+(s) + \frac{1}{Z_g(s)}\right)} \tag{2.26}$$

Various operating conditions have been tested for this method, where both the simulation results and the experimental results validate the theoretical analysis, which can be found in [J1]. To show the effectiveness, one of the test results, which is a sequence-coupled resonance, is shown with the simulation results in Fig. 2.7 and experimental results in Fig. 2.9, where the system parameters and control parameters are listed in Table 2.1 and 2.2, respectively. In both the simulations and the experiments, the resonance frequencies are the same located at 11 Hz and 111 Hz, as shown in Fig. 2.8 and Fig. 2.10. Then, the admittance-ratios are plotted in Fig. 2.11, where the phase

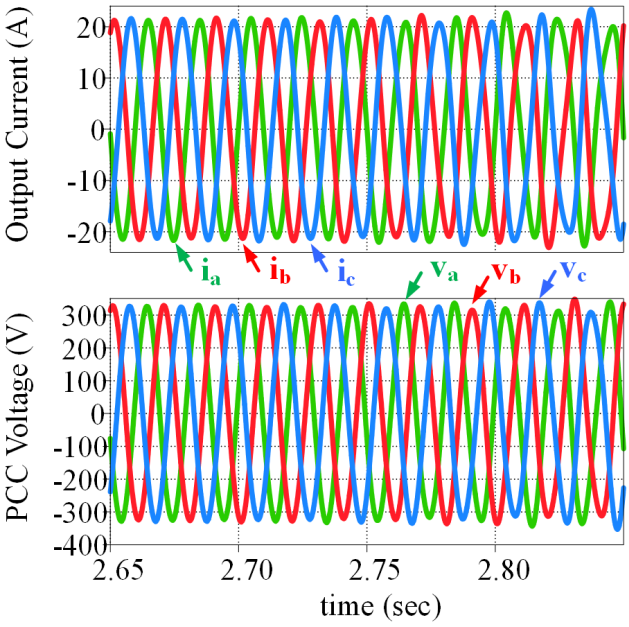

Fig. 2.7: Time-domain voltage and current waveforms of the simulation results using the parameters in Table 2.1 and Table 2.2. Source: [J1].

crossover frequencies are -10.8 Hz and 110.8 Hz with gain margin which is equal to 0.72 dB. This negative resonance frequency (-10.8 Hz) indicates a negative-sequence resonant component in the three-phase system, which is caused by the oscillations induced by the SRF-PLL at 60.8 Hz in the q-axis. Thus, in the $\alpha\beta$-frame, the resonance is transformed to $50 - 60.8 = -10.8$ Hz and $50 + 60.8 = 110.8$ Hz. Since the sequence information cannot be shown in the real-value harmonic spectra shown in Fig. 2.8 and Fig. 2.10, only the 11 Hz and 111 Hz resonance frequencies are observed. This case shows that the SISO admittance-ratio stability analysis method based on two-port network can effectively predict the sequence-coupled resonances as well.

2.4 Other Variants of Two-Port Networks

The admittance form of the two-port network model of the VSC in (2.6) is not unique, e.g. the VSC can also be modeled with the impedance parameters (Z parameters) and be formed as an impedance-matrix. Thus, the terminal voltage depends on the terminal current. Further, there exist other variants of electrical parameters (H-, G-, and ABCD-parameters [55]) can also be used to describe the two-port network, where the closed-loop gains describing the

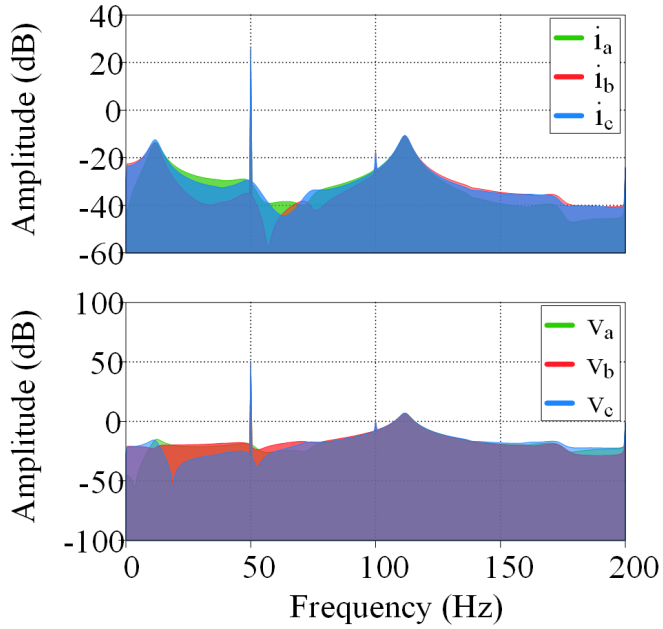

Fig. 2.8: Frequency spectrum of Fig. 2.7. Source: [J1].

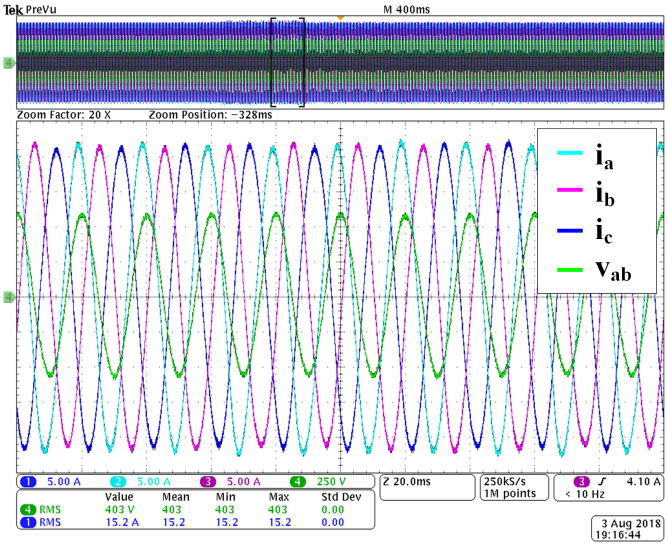

Fig. 2.9: Time-domain voltage and current waveforms of the experimental results using the parameters in Table 2.1 and Table 2.2 (X-axis: 20 ms/*div*, Y-axis: i_a, i_b, i_c: 5 A/*div*, v_{ab}: 100 V/*div*). Source: [J1].

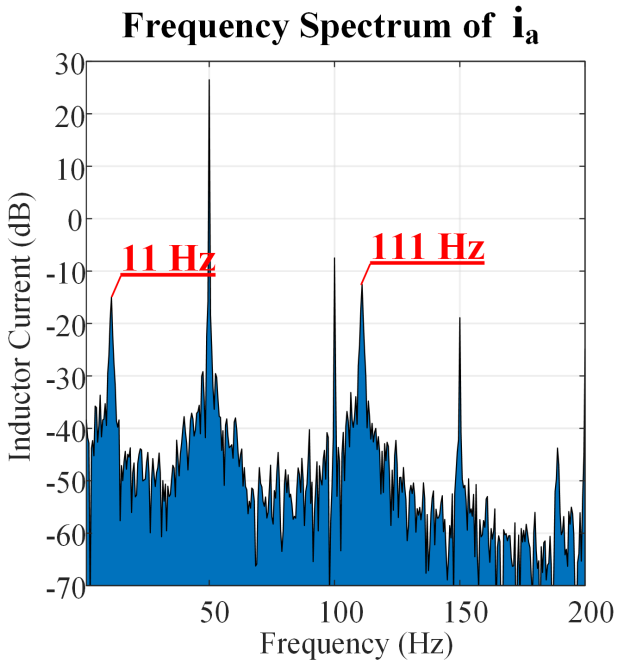

Fig. 2.10: Frequency spectrum of i_a in Fig. 2.9. Source: [J1].

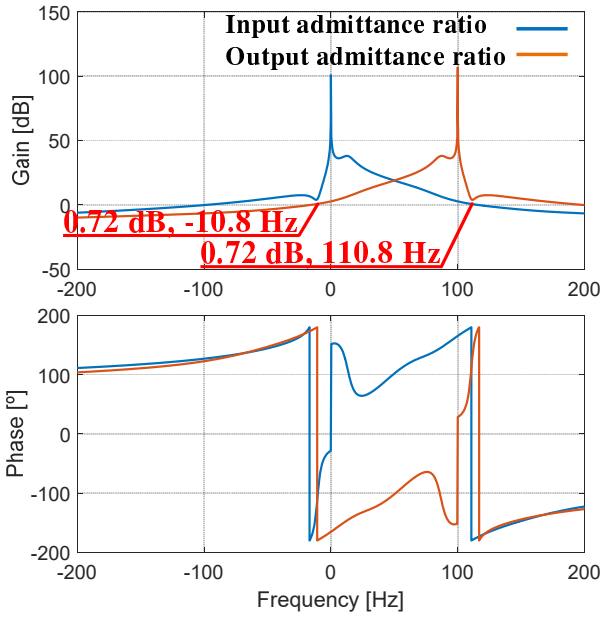

Fig. 2.11: Bode plot of input and output admittance ratios. Source: [J1].

terminal's electric relationships can be derived with a similar process, which have been proved to be mathematically equivalent [55].

Beside of the mentioned electrical-parameter-type of two-port network, there are other types of two-port networks using the incident and reflected power waves to determine, which are the scattering- and the scattering inverse-parameters (S- and T-paramters), where they are widely used in the analysis of radio-frequency (RF) and Microwave circuits when the terminal voltage and current are hardly measued in the open- or short-circuit conditions [56]. It is worth mentioning that only the Z-, Y-, and S-parameters can be used in the network with more than two ports, the other variants, H-, G-, ABCD-, and T-parameters, are limited to the two-port network since the entries in these matrices have the same unit. The two-port network with the S-parameters is further discussed in Chapter 3.

2.5 Summary

In this chapter, the $\alpha\beta$-frame impedance model of the current-controlled grid-connected VSC is briefly introduced, which is described as a two-port network with Y-parameters. Then, a common SISO open-loop gain of the MIMO system can be derived with the entries in the admittance matrix of the VSC and the grid impedances. By reformulating the closed-loop gains, the SISO open-loop gain is transformed into two SISO admittance ratios, and the need of measuring all four entries of the VSC admittance matrix can be avoided for stability analysis, which is superior to the conventional impedance-based approach. This two-port network modeling method can be used to analyze the frequency-coupled dynamics of the VSC. It has been demonstrated in the frequency-domain, time-domain simulations and experimental tests.

Related Publications

[C1] **S.-F. Chou**, X. Wang, and F. Blaabjerg, "Stability Analysis of Grid-connected VSCs Based on Two-port Network Theory," *2019 IEEE Applied Power Electronics Conference and Exposition (APEC)*, Anaheim, CA, USA, 2019, pp. 1165-1172.

[J1] **S.-F. Chou**, X. Wang, and F. Blaabjerg, "Two-Port Network Modeling and Stability Analysis of Grid-Connected Current-Controlled VSCs," in *IEEE Trans. Power Electrons.*, vol. 35, no.4, pp. 3519-3529, April 2020.

Chapter 3

Modeling and Stability Analysis of Multi-VSC System

3.1 Background

In Chapter 2, two admittance ratios, Y_S/Y_{in} and Y_L/Y_{out}, are identified as the open-loop gains to characterize the MIMO system using equations (2.17), (2.18), (2.19), and (2.20). When analyzing the single-VSC systems, the grid impedance is generally assumed to contain only the passive components. Thus, the admittances, Y_S and Y_L will not include any right-half plane (RHP) poles and zeros. Thus, when the number of RHP zeros is known to be zero, the Nyquist stability criterion can sufficiently analyze the stability in the single-VSC system with admittance ratios. However, in the multi-VSC systems, the grid impedance seen from the PCC is a combination of the passive components and the input admittances of other VSCs, where prior knowledge of RHP zeros in the admittances is necessary [57]. For this reason, in [57], an impedance-sum stability analysis method for the cascaded two VSCs system has been proposed. By analyzing the closed-loop characteristic equation of the system with the Cauchy's argument principle, the influence of the RHP zeros in the impedance of VSC can be averted. Yet, the method in [57] still requires the individually stable subsystems to ensure that the encirclement of the impedance-sum in the complex plane can truly reflect the number of RHP poles in the closed-loop characteristic equation.

Both the impedance-ratio based analysis method and impedance-sum based analysis method have been proposed and used in the multi-VSC system. In [15], the impedance-ratio based analysis method considering the

RHP zeros in the impedance of VSC is presented using the Nyquist stability criterion for the multi-loop dynamic systems, which subdivides the system into $Z + Z$ or $Z + Y$ subsystems for analyzing the stability in a source-source system or source-load system, respectively. The impedance-sum based analysis method is presented in the power system for analyzing the stability at a specified bus, e.g. with multiple wind power plants connected. It has also subdivided the system into impedance network models, which are the upstream and downstream impedances, and it is clearly shown that the upstream impedance contains only the line impedances, which is combination of passive components containing no RHP zeros [58]. Yet, for the impedance-based analysis method, the state-of-art of analyzing the multi-VSC system requires the prior knowledge of the system to properly subdivide the system into subsystems in order to achieve the assumption of no RHP zeros and having individual stable subsystems.

This chapter aims to address these issues by introducing another form of two-port network, which is shortly mentioned in Chapter 2.4, i.e., the two-port network using S-parameters. Based on it, the reflection coefficient stability criterion is developed, by which, the influence of the open-loop RHP poles in the impedances can be avoided, and prior knowledge of the system to properly subdivide the system is unnecessary. With the reflection coefficient stability criterion, a systematical approach of stability analysis using 6 steps is proposed for the multi-VSC system, which can identify the sensitive bus in the system, and the resonance frequency of the sensitive bus.

3.2 Two-Port Network Modeling with S-Parameter

To introduce the two-port network with S-parameter, the electrical port relations of the admittance matrix in Fig. 2.6, which is illustrated again in Fig. 3.1 for reference, are given as

$$\begin{bmatrix} i_1 \\ i_2 \end{bmatrix} = \begin{bmatrix} y_{11} & y_{12} \\ y_{21} & y_{22} \end{bmatrix} \begin{bmatrix} v_1 \\ v_2 \end{bmatrix} \tag{3.1}$$

where the Laplace complex variable, s, is omitted for simplification. y_{11}, y_{12}, y_{21}, and y_{22} are defined with the short-circuit conditions, which $v_1 = 0$ or $v_2 = 0$, as follows

$$\begin{aligned} y_{11} &\triangleq \left.\frac{i_1}{v_1}\right|_{v_2=0} \quad y_{12} \triangleq \left.\frac{i_1}{v_2}\right|_{v_1=0} \\ y_{21} &\triangleq \left.\frac{i_2}{v_1}\right|_{v_2=0} \quad y_{22} \triangleq \left.\frac{i_2}{v_2}\right|_{v_1=0} \end{aligned} \tag{3.2}$$

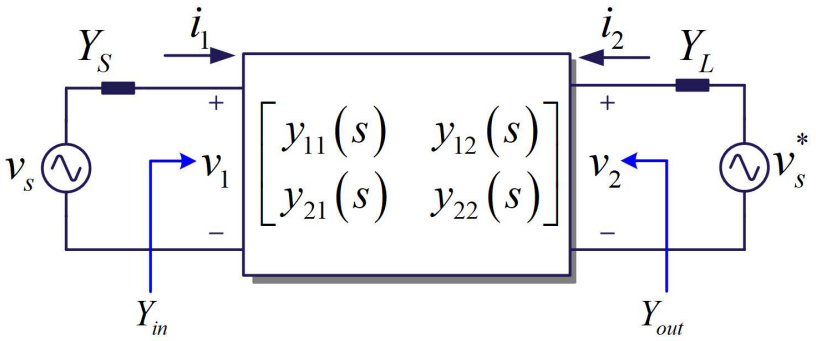

Fig. 3.1: General admittance form of the LTI two-port network model. Source: [J1].

Compared with the Y-parameter, the S-parameters are defined based on the power waves, i.e. incident power wave and reflected power wave, and the common definition used in the RF and Microwave circuits analysis [56] is based on the research from Kurokawa [59], which defines the incident power wave, a_i, and reflected power wave, b_i, at i^{th} port of a two-port network as

$$\begin{aligned} a_i &= \frac{1}{2}\frac{v_i + Z_i i_i}{\sqrt{\mathrm{Re}\{Z_i\}}} \\ b_i &= \frac{1}{2}\frac{v_i - Z_i^* i_i}{\sqrt{\mathrm{Re}\{Z_i\}}}, i = 1, 2 \end{aligned} \tag{3.3}$$

where v_i and i_i are the complex number form of the voltage and current at port i, and Z_i and Z_i^* are equivalent impedance looking out from i^{th} port and its complex conjugate, which means the impedance Z_i can be different for each port. However, to simplify the analysis process, the impedance of each port is assumed to be identical. Then, the incident and reflected power waves in (3.3) can be simplified as

$$\begin{aligned} a_i &= \frac{1}{2}\frac{v_i + Z_0 i_i}{\sqrt{\mathrm{Re}\{Z_0\}}} \\ b_i &= \frac{1}{2}\frac{v_i - Z_0^* i_i}{\sqrt{\mathrm{Re}\{Z_0\}}}, i = 1, 2 \end{aligned} \tag{3.4}$$

where Z_0 is called the characteristic impedance of the system, which corresponds to the maximum delivery power of the circuit [56]. The selection of the characteristic impedance in the VSC based power system is detailed in [J2], where the characteristic/surge impedance of the transmission line cables is used, i.e. $Z_0 = 40\ \Omega$, since the possible maximum power delivery in a power system depends on the *surge impedance load* of the tranmission line [60]. Therefore, like the two-port network characterized with the Y-parameters ma-

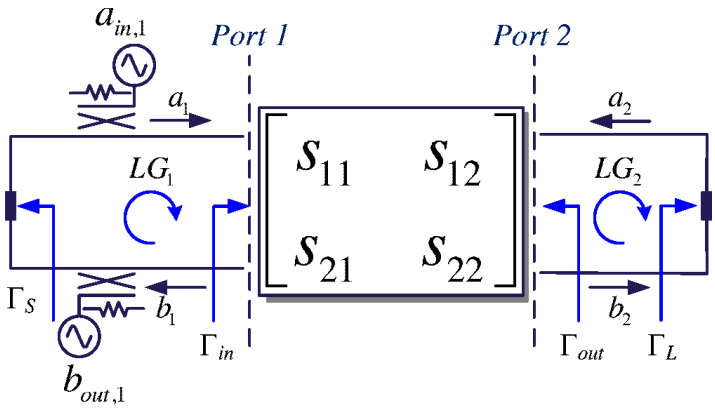

Fig. 3.2: General S-paramter form of the LTI two-port network model. Source: [J2].

trix shown in (3.1), the two-port network with the S-parameters is given as

$$\begin{bmatrix} b_1 \\ b_2 \end{bmatrix} = \begin{bmatrix} s_{11} & s_{12} \\ s_{21} & s_{22} \end{bmatrix} \begin{bmatrix} a_1 \\ a_2 \end{bmatrix} \tag{3.5}$$

To link the elements of matrices in (3.1) and (3.5) with each other, the voltage and current vectors, v_i and i_i can be written in the form of a_i, b_i, and Z_0 as

$$\begin{aligned} v_i &= \sqrt{\frac{2}{Z_0 + Z_0^*}} \cdot \left(Z_0^* a_i + Z_0 b_i\right) \\ i_i &= \sqrt{\frac{2}{Z_0 + Z_0^*}} \cdot \left(a_i - b_i\right), i = 1, 2 \end{aligned} \tag{3.6}$$

Then, the elements in the matrix of (3.5) can be derived as

$$\begin{aligned} s_{11} &= \frac{\left(1 - Z_0 y_{11}\right)\left(1 + Z_0 y_{22}\right) + Z_0^2 y_{12} y_{21}}{\left(1 + Z_0 y_{11}\right)\left(1 + Z_0 y_{22}\right) - Z_0^2 y_{12} y_{21}} \\ s_{12} &= \frac{-2 Z_0 y_{12}}{\left(1 + Z_0 y_{11}\right)\left(1 + Z_0 y_{22}\right) - Z_0^2 y_{12} y_{21}} \\ s_{21} &= \frac{-2 Z_0 y_{21}}{\left(1 + Z_0 y_{11}\right)\left(1 + Z_0 y_{22}\right) - Z_0^2 y_{12} y_{21}} \\ s_{22} &= \frac{\left(1 + Z_0 y_{11}\right)\left(1 - Z_0 y_{22}\right) + Z_0^2 y_{12} y_{21}}{\left(1 + Z_0 y_{11}\right)\left(1 + Z_0 y_{22}\right) - Z_0^2 y_{12} y_{21}} \end{aligned} \tag{3.7}$$

Thus, the Y-parameter circuit in Fig. 3.1 can be transferred to the circuit using S-parameters as shown in Fig. 3.2. Since the S-parameters are defined with the power waves, where both the voltage and the current source can

be used as the power wave sources given in (3.4), the voltage source, v_S, in Fig. 3.1 can be altered as two power wave sources, $a_{in,1}$ and $b_{out,1}$ with the direction to enter and exit from Port 1 of the circuit. The admittances, Y_S and Y_L are also transferred into the reflection coefficient form, which is defined as

$$\Gamma = \frac{Reflected\ \ wave}{Incident\ \ wave} \tag{3.8}$$

$$\begin{aligned} \Gamma_S &= \frac{\frac{1}{Y_S} - Z_0}{\frac{1}{Y_S} + Z_0} \\ \Gamma_L &= \frac{\frac{1}{Y_L} - Z_0}{\frac{1}{Y_L} + Z_0} \end{aligned} \tag{3.9}$$

where the corresponding power waves of voltage sources and the corresponding S-parameters of admittances in Fig. 3.1 can be found in Fig. 3.2.

3.3 Reflection Coefficient Stability Criterion

Like the common SISO open-loop gain can be interpreted as two admittance ratios of the two-port network with Y-parameters in [J1], the SISO open loop gains with the representations of S-parameters and reflection coefficients have been described in detail in [C2].

In Fig 3.2, when there exist a forcing wave, $a_{in,1}$, imposing into the two-port network at Port 1, the incident wave a_1 can be derived as

$$a_1 = \Gamma_S \left(a_{in,1} + b_1\right) = \Gamma_S a_{in,1} + \Gamma_S \Gamma_{in} a_1 \tag{3.10}$$

where the Γ_{in} and Γ_{out} in Fig 3.2 can be derived with the *signal-flow graph* detailed in [J2], and they are given as

$$\begin{aligned} \Gamma_{in} &= \frac{b_1}{a_1} = S_{11} + \frac{S_{12}S_{21}\Gamma_L}{1 - S_{22}\Gamma_L} \\ \Gamma_{out} &= \frac{b_2}{a_2} = S_{22} + \frac{S_{12}S_{21}\Gamma_S}{1 - S_{11}\Gamma_S} \end{aligned} \tag{3.11}$$

Thus, the SISO closed-loop gain from the forcing wave, $a_{in,1}$, to the incident wave, a_1, at Port 1 can be obtained as

$$\frac{a_1}{a_{in,1}} = \frac{\Gamma_S}{1 - \Gamma_S \Gamma_{in}} \tag{3.12}$$

where the SISO closed-loop gain from the forcing wave, $a_{in,1}$, to the reflected wave, b_1, at Port 1 can also be derived as

$$\frac{b_1}{a_{in,1}} = \frac{\Gamma_S \Gamma_{in}}{1 - \Gamma_S \Gamma_{in}} \tag{3.13}$$

It is worth mentioning that if the direction of the forcing wave is exiting the two-port network, i.e. $b_{out,1}$, the SISO closed-loop gains from $b_{out,1}$ to a_1 and b_1 are given as

$$\begin{aligned} \frac{a_1}{b_{out,1}} &= \frac{\Gamma_S \Gamma_{in}}{1 - \Gamma_S \Gamma_{in}} \\ \frac{b_1}{b_{out,1}} &= \frac{\Gamma_{in}}{1 - \Gamma_S \Gamma_{in}} \end{aligned} \tag{3.14}$$

where the same SISO open-loop gain, $LG_1 = -\Gamma_S \Gamma_{in}$ at Port 1, can be found in the denominators of (3.12), (3.13), and (3.14). The other open-loop gain, $LG_2 = -\Gamma_L \Gamma_{out}$, can be similarly derived at Port 2, which is not repeated here. To be noticed, this SISO open-loop gain, $-\Gamma_S \Gamma_{in}$, is similar to the admittance ratio, Y_S/Y_{in} identified in Chapter 2.3, but they are not equivalent. To compare with the reflection coefficient stability criterion with the impedance-based stability criteria in [57], the conversion between the impedances, Z, and the reflection coefficients, Γ, referred to the characteristic impedance, Z_0, have to be carried out first as

$$\begin{aligned} Z &= Z_0 \frac{1 + \Gamma}{1 - \Gamma} \\ \Gamma &= \frac{Z - Z_0}{Z + Z_0} \end{aligned} \tag{3.15}$$

Then, the characteristic equation, $1 - \Gamma_S \Gamma_{in}$, in (3.12), (3.13), and (3.14) can be represented with Z_S and Z_{in} as

$$1 - \Gamma_S \Gamma_{in} = \frac{2 Z_0 \left(Z_S + Z_{in} \right)}{\left(Z_S + Z_0 \right) \left(Z_{in} + Z_0 \right)} \tag{3.16}$$

where the number of times of the trajectory, $-\Gamma_S \Gamma_{in}$, clockwise encircles the point $(-1, 0)$ in the complex plane, $\mathcal{N}_{1-\Gamma_S \Gamma_{in}}$, can then be determined using the Cauthy's argument principle [61] as

$$\begin{aligned} \mathcal{N}_{1-\Gamma_S \Gamma_{in}} &= \mathcal{Z} \left(1 - \Gamma_S \Gamma_{in} \right) - \mathcal{P} \left(1 - \Gamma_S \Gamma_{in} \right) \\ &= \mathcal{Z} \left(\frac{Z_S + Z_{in}}{\left(Z_S + Z_0 \right) \left(Z_{in} + Z_0 \right)} \right) - \mathcal{P} \left(\frac{Z_S + Z_{in}}{\left(Z_S + Z_0 \right) \left(Z_{in} + Z_0 \right)} \right) \\ &= \mathcal{Z} \left(Z_S + Z_{in} \right) + \mathcal{P} \left(Z_S + Z_0 \right) + \mathcal{P} \left(Z_{in} + Z_0 \right) \\ &\quad - \mathcal{P} \left(Z_S + Z_{in} \right) - \mathcal{Z} \left(Z_S + Z_0 \right) - \mathcal{Z} \left(Z_{in} + Z_0 \right) \end{aligned} \tag{3.17}$$

where $\mathcal{P}$ and $\mathcal{Z}$ represent the number of RHP poles and zeros, respectively. The $\mathcal{Z} \left(1 - \Gamma_S \Gamma_{in} \right)$ indicates the existence of the RHP zeros in the characteristic equation, which are the RHP poles of the closed-loop gains that imply the system instability. Since $\mathcal{P} \left(Z_S + Z_{in} \right) = \mathcal{P} \left(Z_S \right) + \mathcal{P} \left(Z_{in} \right)$, and Z_0 has the

positive real value indicating $\mathcal{P}(Z_0) = 0$, $\mathcal{Z}(1 - \Gamma_S\Gamma_{in})$ can be derived as

$$\begin{aligned}\mathcal{Z}(1 - \Gamma_S\Gamma_{in}) = \mathcal{N}_{1-\Gamma_S\Gamma_{in}} + \mathcal{P}(Z_S) + \mathcal{P}(Z_{in}) \\ + \mathcal{Z}(Z_S + Z_0) + \mathcal{Z}(Z_{in} + Z_0)\end{aligned} \tag{3.18}$$

Thus, the number of RHP zeros in $1 - \Gamma_S\Gamma_{in}$ depends on 1) the encirclement of $\mathcal{N}_{1-\Gamma_S\Gamma_{in}}$, 2) the number of RHP poles in Z_S and Z_{in}, 3) the number of RHP zeros in $Z_S + Z_0$ and $Z_{in} + Z_0$. Therefore, the other two trajectories, $\mathcal{N}_{1-\Gamma_S}$ and $\mathcal{N}_{1-\Gamma_{in}}$, can be used to derive $\mathcal{Z}(1 - \Gamma_S\Gamma_{in})$, which are given as

$$\begin{aligned}\mathcal{N}_{1-\Gamma_{in}} &= \mathcal{Z}\left(\frac{2Z_0}{Z_{in} + Z_0}\right) - \mathcal{P}\left(\frac{2Z_0}{Z_{in} + Z_0}\right) \\ &= \mathcal{P}(Z_{in}) - \mathcal{Z}(Z_{in} + Z_0)\end{aligned} \tag{3.19}$$

$$\mathcal{N}_{1-\Gamma_S} = \mathcal{P}(Z_S) - \mathcal{Z}(Z_S + Z_0)$$

Equation (3.18) can then be written as

$$\mathcal{Z}(1 - \Gamma_S\Gamma_{in}) = \mathcal{N}_{1-\Gamma_S\Gamma_{in}} - \mathcal{N}_{1-\Gamma_S} - \mathcal{N}_{1-\Gamma_{in}} + 2\mathcal{P}(Z_S) + 2\mathcal{P}(Z_{in}) \tag{3.20}$$

As discussed in Chapter 3.1, the impedance seen from the PCC in a multi-VSC system is the combination of the grid impedance and the input impedance of other VSCs including the control dynamics, where the presence of RHP poles should be considered to assess the system stability. Thus, two conditions 1) Z_S and Z_{in} are individually stable, 2) Z_S or Z_{in} contains RHP poles, are discussed as follows:

3.3.1 Stable Z_S and Z_{in}

Since Z_S and Z_{in} are individually stable, which mean $\mathcal{P}(Z_S) = \mathcal{P}(Z_{in}) = 0$, equation (3.20) can be simplified to

$$\mathcal{Z}(1 - \Gamma_S\Gamma_{in}) = \mathcal{N}_{1-\Gamma_S\Gamma_{in}} - \mathcal{N}_{1-\Gamma_S} - \mathcal{N}_{1-\Gamma_{in}} \tag{3.21}$$

where the system is stable if and only if equation (3.21) is equal to zero.

3.3.2 Unstable Z_S or Z_{in}

For the unstable Z_S or Z_{in} conditions, the number of RHP poles in Z_S and Z_{in}, which are $\mathcal{P}(Z_S)$ and $\mathcal{P}(Z_{in})$, are either zero or positive constant. Yet, $\mathcal{Z}(Z_S + Z_0)$ and $\mathcal{Z}(Z_{in} + Z_0)$ may be changed with different values of Z_0. Therefore, equation (3.20) is rewritten with (3.19) as

$$\mathcal{Z}(1 - \Gamma_S\Gamma_{in}) = \mathcal{N}_{1-\Gamma_S\Gamma_{in}} + \mathcal{N}_{1-\Gamma_S} + \mathcal{N}_{1-\Gamma_{in}} + 2\mathcal{Z}(Z_S + Z_0) + 2\mathcal{Z}(Z_{in} + Z_0) \tag{3.22}$$

where the system is stable if and only if (3.22) is equal to zero. Thus, in order to derive the exact number of $\mathcal{Z}\left(1-\Gamma_S\Gamma_{in}\right)$ using only the trajectories of $\mathcal{N}_{1-\Gamma_S\Gamma_{in}}$, $\mathcal{N}_{1-\Gamma_S}$, and $\mathcal{N}_{1-\Gamma_{in}}$, $\mathcal{Z}\left(Z_S+Z_0\right)$ and $\mathcal{Z}\left(Z_{in}+Z_0\right)$ should be equal to zero, where the following closed-loop gain with the characteristic equation of Z_S+Z_0 is considered.

$$G_{cl}=\frac{Z_SZ_0}{Z_S+Z_0}=\frac{Z_S}{1+\frac{1}{Z_0}Z_S} \tag{3.23}$$

and the impedance Z_S can be presented as the ratio of two polynomials as

$$Z_S=\frac{N\left(s\right)}{D\left(s\right)} \tag{3.24}$$

and the closed-loop gain, G_{cl} can be derived as

$$G_{cl}=\frac{N\left(s\right)}{D\left(s\right)+\frac{1}{Z_0}N\left(s\right)} \tag{3.25}$$

where the poles of G_{cl} are the roots of the characteristic equation given as

$$D\left(s\right)+\frac{1}{Z_0}N\left(s\right)=0 \tag{3.26}$$

where the roots of (3.26) vary from the zeros of Z_S, $N\left(s\right)=0$, to the poles of Z_S, $D\left(s\right)=0$, with increasing the value of Z_0 from 0 to ∞ [61], and the trajectories of the roots are the root locus of $1+\frac{1}{Z_0}Z_S$. Thus, even if impedance Z_S contains RHP poles, as long as there exists a gain of $\frac{1}{Z_0}$ making the roots of (3.26) move into the left half plane, the number of $\mathcal{N}_{1-\Gamma_S}$ has to change accordingly [62], i.e., $\mathcal{N}_{1-\Gamma_S}$ has clockwise encirclement since equation (3.19) becomes positive. To that end, if $\mathcal{Z}\left(Z_S+Z_0\right)=\mathcal{Z}\left(Z_{in}+Z_0\right)=0$, equation (3.22) can be simplified as

$$\mathcal{Z}\left(1-\Gamma_S\Gamma_{in}\right)=\mathcal{N}_{1-\Gamma_S\Gamma_{in}}+\mathcal{N}_{1-\Gamma_S}+\mathcal{N}_{1-\Gamma_{in}} \tag{3.27}$$

To be noticed that, the system stability analysis is achieved by checking the value of $\mathcal{Z}\left(1-\Gamma_S\Gamma_{in}\right)$, which is equal to either 0 or positive real constant. Thus, the system stability criterion can be summarized with following steps:

1. Check the value of $\mathcal{N}_{1-\Gamma_S\Gamma_{in}}-\mathcal{N}_{1-\Gamma_S}-\mathcal{N}_{1-\Gamma_{in}}$.
   - $>$ 0: According to (3.20), $\mathcal{Z}\left(1-\Gamma_S\Gamma_{in}\right)$ is positive, the system is unstable.
   - $=$ 0: $\mathcal{Z}\left(1-\Gamma_S\Gamma_{in}\right)$ might be equal to $2\mathcal{P}\left(Z_S\right)+2\mathcal{P}\left(Z_{in}\right)$. System stability is unknown, move to Step 2.

- $<$ 0: Either $\mathcal{P}(Z_S)$ or $\mathcal{P}(Z_{in})$ are positive, which indicates usnstable subsystems. Thus, the system is unstable [62].

2. Check the value of $\mathcal{N}_{1-\Gamma_S\Gamma_{in}} + \mathcal{N}_{1-\Gamma_S} + \mathcal{N}_{1-\Gamma_{in}}$
   - $>$ 0: According to (3.22), $\mathcal{Z}(1-\Gamma_S\Gamma_{in})$ is positive, the system is unstable.
   - $=$ 0: $\mathcal{P}(Z_S)+\mathcal{P}(Z_{in})$ might be equal to $\mathcal{Z}(Z_S+Z_0)+\mathcal{Z}(Z_{in}+Z_0)$, system stability is yet unknown, move to Step 3.
   - $<$ 0: $\mathcal{Z}(Z_S+Z_0)+\mathcal{Z}(Z_{in}+Z_0)$ is positive. Change the value of Z_0, and then re-plot $-\Gamma_S\Gamma_{in}$, $-\Gamma_S$, and $-\Gamma_{in}$, repeat Step 2.
3. Check the values of $\mathcal{N}_{1-\Gamma_S}$ and $\mathcal{N}_{1-\Gamma_{in}}$ individually.
   - Both $\mathcal{N}_{1-\Gamma_S}$ and $\mathcal{N}_{1-\Gamma_{in}}$ are equal to zero, the system is stable.
   - One of $\mathcal{N}_{1-\Gamma_S}$ and $\mathcal{N}_{1-\Gamma_{in}}$ is positive and the other is negative, which indicates usnstable subsystems. Thus, the system is unstable [62].

Remark (Stability criterion to analyze the system with potential unstable subsystems)
The conditions with stable subsystems and potential unstable subsystems are discussed using the summarized stability criterion. The system stability can be analyzed using three trajectories of reflection coefficients, $-\Gamma_S$, $-\Gamma_{in}$, and $-\Gamma_S\Gamma_{in}$, where it can analyze the system without the prior knowledge of the RHP zeros and poles in the impedances. Furthermore, the relative stability indices, such as phase margin and gain margin, can still be defined in the SISO open-loop gain $-\Gamma_S\Gamma_{in}$.

3.4 Stability Analysis for Multi-VSC System

The reflection coefficient stability criterion described in Chapter 3.3 require no prior knowledge of the RHP zeros and poles in the impedances, which has the advantage to analyze the system stability in the multi-VSC system. To demonstrate the system stability analysis process, a 3-bus system with two VSCs as shown in Fig. 3.3 is used as the test system in [C2], [C3], and [J2]. In the system, there exist two VSCs, VSC 1 and VSC 2, which are parallel-connected at Bus 3 via two grid impedances Z_{g1} and Z_{g2}, where the single-line diagram and the small-signal control block diagram of VSC can be found in Fig. 2.1 and Fig. 2.2. Then, these two subsystems connect to the ideal voltage source v_g through another grid impedance Z_{g3}. A stability analysis procedure for multi-VSC system with impedance model using 4 steps has

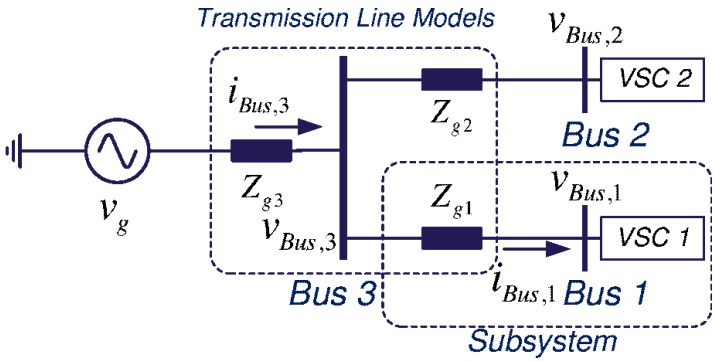

Fig. 3.3: System configuration with multi-grid-connected VSCs. Source: [J2].

been first introduced in [C3], which has then been refined as procedure with 6 steps in [J2]. The six steps are given below and the actions for analyzing the 3-bus system in Fig. 3.3 are followed:

Step 1: Selecting a system-shared characteristic impedance Z_0

The details of the selection of characteristic impedance Z_0 can be found in [J2], where the importance has been explained in Chapter 3.3 regarding the reflection coefficient stability criterion. In the multi-VSC system, the input admittances of VSCs are frequency-dependent and are varied with different operating points, which cannot be characterized using a constant value of the impedance. Therefore, the value of characteristic/surge impedance of transmission line is used to characterized the system.

> **Action:** The value of 40 Ω, which is the value of characteristic/surge impedance of typical underground cables [22], is chosen for the multi-VSC system shown in Fig. 3.3. For an overhead transmission line, the value of characteristic/surge impedance is around 400 Ω [22].

Step 2: Acquiring two-port network representations of all components in the system

In Fig. 3.3, the system includes grid impedances and 2 VSCs. It is suggested to transform all the components in the system to two-port network representations for following two purposes:

1) Capture the asymmetrical control dynamics of VSCs with the MIMO impedance-model.

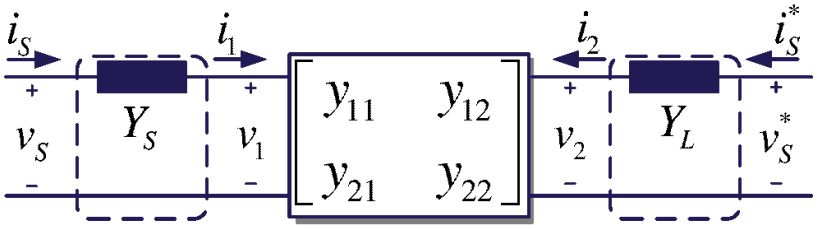

Fig. 3.4: Open the circuit of the two-port network shown in Fig. 2.6. Source: [J2].

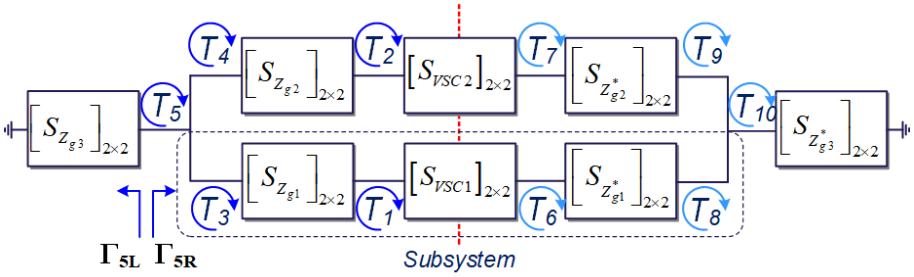

Fig. 3.5: Single-line diagram of a 3-bus system shown in Fig. 3.3. Source: [J2].

2) Retain the interactions between the grid impedance and VSCs, which is asymmetrical, in which, the two-port network representations can be either theoretical derivations [11] or measurement results [54].

Action: The subsystems circled in Fig. 3.3 can be represented as Fig. 3.4, which contains three cascaded two-port networks by opening the circuit like in Fig. 2.6, where the admittance Y_S can be described as an individual two-port network terminated with v_S and v_1, and Y_L forms another two-port network terminated with v_2 and v_S^*. For describing the cascaded network or the transmission line model, which is the main contribution of the grid impedance, the ABCD-paramter representation is generally used [22]. Thus, the system and control parameters of Fig. 3.3 are listed in Table 3.1 [J2].

Step 3: Applying the conversions between S-parameter and other electrical parameters

Since the impedances seen at each bus are the combination of grid impedances and the input admittance of VSCs, where the possibility of RHP-pole presence cannot be ignored, the reflection coefficient stability criterion is needed to be applied in the analysis. To be noticed, the Y-to-S-parameter conversion is explained in (3.7), where ABCD-to-S-parameter conversion can be found

Table 3.1: System and control parameters of the systems in Fig. 3.3. Source: [J2]

Symbol	Parameter Description	Value
v_g	Grid voltage	400 V_{rms}
i_d^{ref}	d-axis current command of VSC 1 and VSC 2	11.5 A
i_q^{ref}	q-axis current command of VSC 1 and VSC 2	0 A
Z_{g1}	Grid impedance Z_{g1}	4 mH
Z_{g2}	Grid impedance Z_{g2}	4 mH
Z_{g3}	Grid impedance Z_{g3}	11 mH
K_{cp}	Proportional gain in the ac current controllers of VSC 1 and VSC 2	18.3 Ω
K_{ci}	Integral gain in the ac current controllers of VSC 1 and VSC 2	6400 $\Omega\,\mathrm{s}^{-1}$
$K_{pp,1}$	Proportional gain in PLL of VSC 1	1 (V s)
$K_{pp,2}$	Proportional gain in PLL of VSC 2	1 (V s)
$K_{pi,1}$	Integral gain in PLL of VSC 1	100 rad/(V s^2)
$K_{pi,2}$	Integral gain in PLL of VSC 2	250 rad/(V s^2)

in [J2]. The other electrical parameters (Z-, H-, and G-) to S-parameter conversion have been specified in [63].

Action: The system depicted in Fig. 3.3 can be described as two-port networks connections shown like in Fig. 3.5.

Step 4: Deriving the SISO open-loop gains on each bus

The SISO open-loop gains are derived from the reflection coefficients on both sides of the bus, which can be derived using the *signal flow graph* reduction process in [J2]. Since the analysis using the reflection coefficients is adopted in the field of RF/Microwave circuit for decades, some mature tools have already been developed and widely used in those fields [64].

Action: In the validation, the reflection coefficients are derived using the computer-aided software, NI AWR Design Environment™ [64], and the results are plotted in the complex plane. Open-loop gains, T_1, T_2, T_3, T_4, T_5, and T_{10} in Fig. 3.5 are plotted from Fig. 3.6 to Fig. 3.11, where the relative stability margins are given in Table 3.2. To be noticed that, the NI AWR Design Environment™ [64] tool is developed for high frequency RF/Microwave circuit design, which the open-loop gains T_1, T_2, T_3, T_4, T_5,

and T_{10} cannot be plotted with the negative-frequency vectors. Therefore, the frequency vectors are shifted with an offset to ensure that the whole frequency range locates in the positive frequency range, i.e. the sweeping minimum frequency, 0.1 Hz, and sweeping maximum frequency, 1000 Hz, in Fig. 3.6 to Fig. 3.11 are actually -500 Hz to 500 Hz.

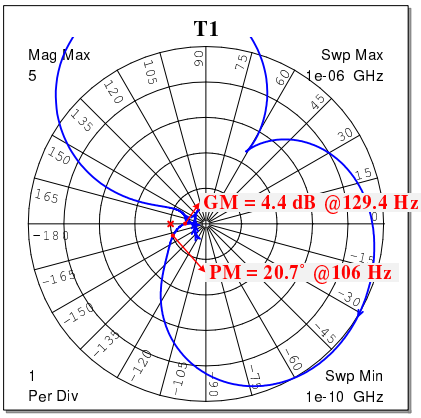

Fig. 3.6: Open-loop gain T_1 in Fig. 3.5. Source: [J2].

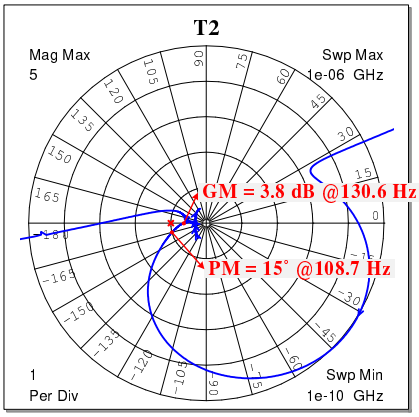

Fig. 3.7: Open-loop gain T_2 in Fig. 3.5. Source: [J2].

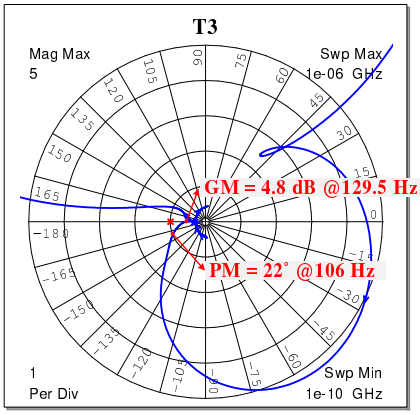

Fig. 3.8: Open-loop gain T_3 in Fig. 3.5. Source: [J2].

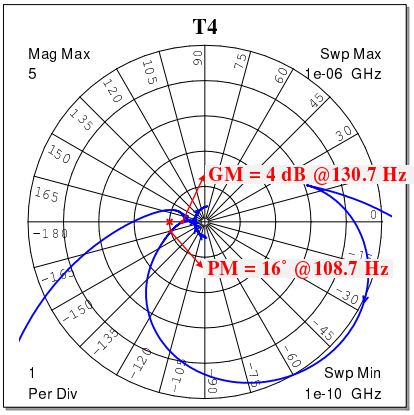

Fig. 3.9: Open-loop gain T_4 in Fig. 3.5. Source: [J2].

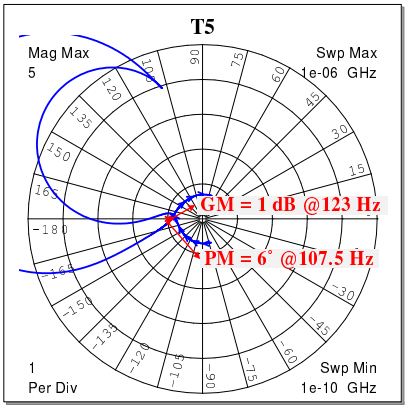

Fig. 3.10: Open-loop gain T_5 in Fig. 3.5. Source: [J2].

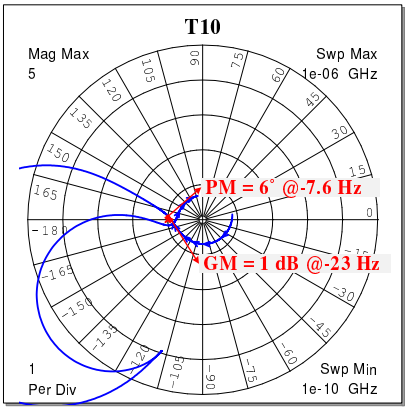

Fig. 3.11: Open-loop gain T_{10} in Fig. 3.5. Source: [J2].

Table 3.2: Gain and phase margin in each open-loop gain. Source: [J2]

Open-loop gain	Gain margin	Phase margin
T_1	4.4 dB at 129.4 Hz	20.7° at 106 Hz
T_2	3.8 dB at 130.6 Hz	15° at 108.7 Hz
T_3	4.8 dB at 129.5 Hz	22° at 106 Hz
T_4	4 dB at 130.7 Hz	16° at 108.7 Hz
T_5	1 dB at 123 Hz	6° at 107.5 Hz
T_{10}	1 dB at -23 Hz	6° at -7.6 Hz

Step 5: Identifying the sensitive SISO open-loop gain

The SISO open-loop gain of the most sensitive bus has the minimum phase and/or gain margins, which can be used to indicate the risk of instability in the system, e.g. the most gain sensitive bus, and the most phase sensitive bus. Because the frequency response of the open-loop gains on both sides of the red dashed line in Fig. 3.5 are frequency-shifted with two times the fundamental frequency [11], just one side of the open-loop gains need to be analyzed. Then, the frequency coupling phenomenon can be predicted by the SISO open-loop gain pair, e.g. (T_5, T_{10}). To be noticed, T_3, T_4, and T_5 are all the open-loop gains on Bus 3, which have different combinations of the components. The details are explained in [J2].

Action: In Table 3.2, SISO open-loop gains T_5 and T_{10}, which have the minimum gain margin of 1 dB and the minimum phase margin of 6° at the same time. Thus, the SISO open-loop gains T_5 and T_{10} can be distinguished as the critical SISO open-loop gain pair that may cause the system instability.

Step 6: Examining the resonance condition at the sensitive bus

For marginally stable system, the SISO open-loop gain does not encircle but cross the critical point $(-1, 0)$, where the resonance frequency can be readily identified. Yet, when the system is close to marginally stable, the gain margin and phase margin exist at different frequencies such as the case specified in Table 3.2. The frequency spectra will then be separated into three regions. To employ the damping solutions, the correct resonance frequency prediction is important. Since a passive system is stable, the resonance conditions can be defined identifying the lack of passivity with the *negative-resistance model* [65].

Like the two-port network has different forms, the resonance condition has impedance form, admittance form, and reflection coefficient form. For

better showing the system lacking of passivity, the SISO open-loop gain, $T_5 = -\Gamma_{5L}\Gamma_{5R}$ in Fig. 3.5 are converted to the admittance form given as

$$\begin{aligned} Y_{5L} &= \frac{1}{Z_0}\frac{1-\Gamma_{5L}}{1+\Gamma_{5L}} \\ Y_{5R} &= \frac{1}{Z_0}\frac{1-\Gamma_{5R}}{1+\Gamma_{5R}} \end{aligned} \tag{3.28}$$

where Y_{5L} and Y_{5R} are complex number given as

$$\begin{aligned} Y_{5L} &= G_{5L} + jB_{5L} \\ Y_{5R} &= G_{5R} + jB_{5R} \end{aligned} \tag{3.29}$$

where details are discussed in [J2], and the resonance condition is given as

$$\begin{aligned} G_{5L}\left(\omega_f\right) + G_{5R}\left(\omega_f\right) &< 0 \\ B_{5L}\left(\omega_f\right) + B_{5R}\left(\omega_f\right) &= 0 \end{aligned} \tag{3.30}$$

Thus, when the system satisfies the resonance condition, it indicates the system loses its passivity, which causes the resonance in the system.

Action: The reflection coefficient of Γ_{5L} and Γ_{5R} are transformed into the admittance form of Y_{5L} and Y_{5R} using equation (3.28), where the resonance condition in (3.30) is examined as shown in Fig. 3.12. The system

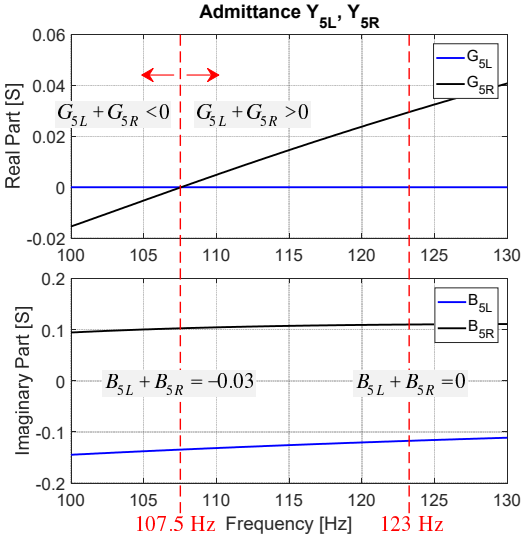

Fig. 3.12: Admittance Y_{5L} and Y_{5R} shown in Fig. 3.5. Source: [J2].

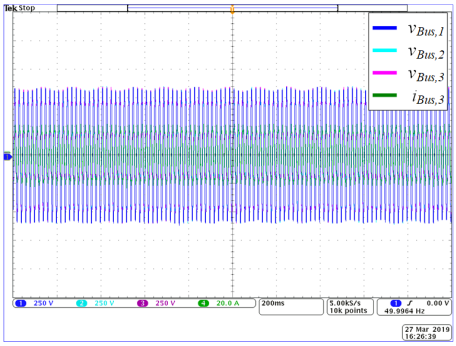

Fig. 3.13: Voltage waveforms on each bus and the total output current (X-axis: 200 ms/div, Y-axis: $v_{Bus,1}$, $v_{Bus,2}$, $v_{Bus,3}$: 250 V/div, $i_{Bus,3}$: 20 A/div). Source: [J2].

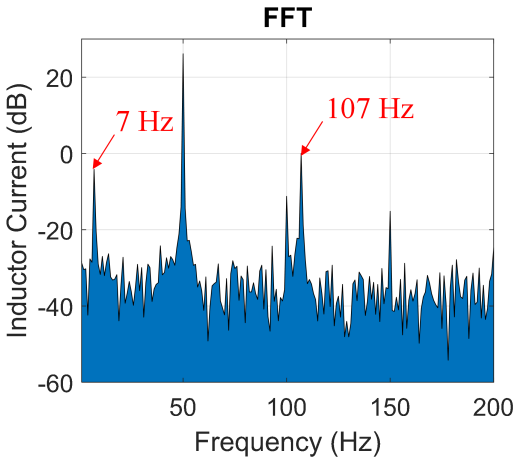

Fig. 3.14: Frequency spectrum of the current $i_{Bus,3}$ in Fig. 3.13. Source: [J2].

is non-passive below 107.5 Hz, which indicates the possible resonance frequencies. Thus, the system in Fig. 3.3 using the parameters listed in Table 3.1 has been tested with experiment, where the time domain waveforms and the frequency spectrum of the current are shown in Fig. 3.13 and Fig. 3.14, respectively. Two resonances are observed in Fig. 3.14, where the resonance at 107 Hz is predicted by Fig. 3.17.

Discussion

The stability analysis procedure in Chapter 3.4 focuses on identifying the sensitive bus and the resonance frequency in the system, where the use of reflection coefficient stability criterion specified in Chapter 3.3 is discussed

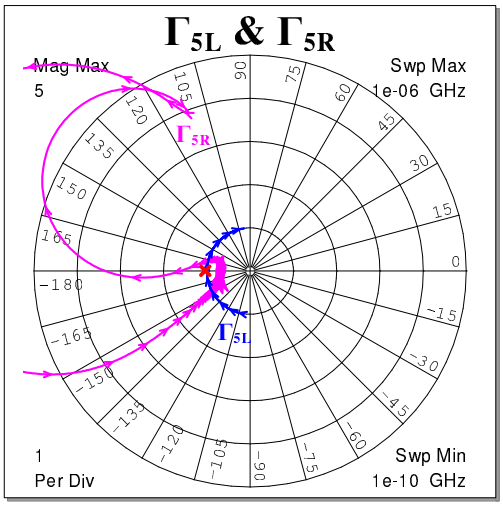

Fig. 3.15: Reflection coefficient Γ_{5L} and Γ_{5R} with $Z_0 = 40\ \Omega$.

here. In order to apply reflection coefficient stability criterion, the other two trajectories, $-\Gamma_{5L}$ and $-\Gamma_{5R}$, are plotted in Fig. 3.15, where $\mathcal{N}_{1-\Gamma_{5L}} = 0$ and $\mathcal{N}_{1-\Gamma_{5R}} = -1$.

For $Z_0 = 40\ \Omega$, the stability criterion is applied using the following steps:

1. The encirclement $\mathcal{N}_{1-\Gamma_{5L}\Gamma_{5R}} - \mathcal{N}_{1-\Gamma_{5L}} - \mathcal{N}_{1-\Gamma_{5R}} = 0$, which the system stability is unknown.
2. $\mathcal{N}_{1-\Gamma_{5L}\Gamma_{5R}} + \mathcal{N}_{1-\Gamma_{5L}} + \mathcal{N}_{1-\Gamma_{5R}} = -2$, $\mathcal{Z}\left(Z_{5L} + Z_0\right) + \mathcal{Z}\left(Z_{5R} + Z_0\right) = 1$. Thus, the value of Z_0 is changed to 4 Ω, and then the trajectories of $-\Gamma_{5L}\Gamma_{5R}$, $-\Gamma_{5L}$, and $-\Gamma_{5R}$ are re-plotted in Fig. 3.16 and Fig. 3.17.
3. Then, $\mathcal{N}_{1-\Gamma_{5L}\Gamma_{5R}} + \mathcal{N}_{1-\Gamma_{5L}} + \mathcal{N}_{1-\Gamma_{5R}}$ becomes zero.
4. Since $\mathcal{N}_{1-\Gamma_{5L}} = \mathcal{N}_{1-\Gamma_{5R}} = 0$, the system is stable.

Even though the reflection coefficient stability criterion indicates the system in Fig. 3.3 is stable using the parameters listed in Table 3.1. The relative stability indices given in Table 3.2 explain that the system resonates due to the lack of margin, and resonance frequencies are predicted with the resonance condition.

3.5 Summary

In this chapter, for the multi-VSC system, the stability analysis method based on the two-port network modeling with the impedance-model of VSC specified in Chapter 2.3 cannot be directly used without the prior knowledge of

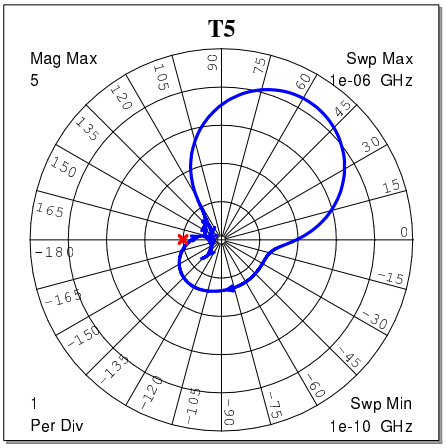

Fig. 3.16: Open-loop gain T_5 with $Z_0 = 4\ \Omega$.

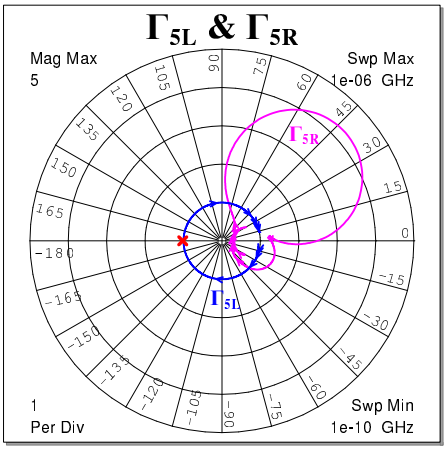

Fig. 3.17: Reflection coefficient Γ_{5L} and Γ_{5R} with $Z_0 = 4\ \Omega$.

the RHP zeros and poles in the impedances. Thus, other form of two-port network, which is the two-port network with S-parameters, is introduced in Chapter 3.2. Based on it, the reflection coefficient stability criterion has been proposed for the multi-VSC system, which does not require the subsystems to be stable. To that end, a stability analysis procedure for multi-VSC systems using impedance model has been suggested along with case study, where the relative stability at each bus can be defined, the most sensitive bus can be determined, and aswell as the potential resonance frequency of the system can be predicted.

Related Publications

[C2] **S.-F. Chou**, X. Wang, and F. Blaabjerg, "Extensions to Two-Port Network Modeling Method and Analysis of Multiple-VSC-Based Systems," *2019 20th Workshop on Control and Modeling for Power Electronics (COMPEL)*, Toronto, ON, Canada, 2019, pp. 1-8.

[C3] **S.-F. Chou**, X. Wang, and F. Blaabjerg, "Stability Analysis of Grid-Connected VSCs Based on S-parameters and Reflection Coefficient," *2019 IEEE Energy Conversion Congress and Exposition (ECCE)*, Baltimore, MD, USA, 2019, pp. 5171-5178.

[J2] **S.-F. Chou**, X. Wang, and F. Blaabjerg, "Reflection Coefficient Stability Criterion for Multi-Bus Multi-VSC Power Systems," in *IEEE Access*, vol. 8, pp. 111186-111199, 2020.

Chapter 4

Improved Resonance Mode Analysis for VSC-Based Power System

4.1 Background

As described in Chapter 3, the stability in the multi-VSC system can be readily analyzed, and the relative stability can be defined at each bus in the system using the impedance models. Through identifying the sensitive bus, the damping solution can be determined. However, the method specified in previous chapter provides only the qualitatively information about the stability, where it cannot provide the quantitative information about the resonance modes of system, nor the contribution of VSCs to the resonance mode.

To investigate the influence of components in the system, such as the shunt capacitors and transformers, on the resonance modes, the harmonic resonance mode analysis (RMA) method [40] uses the nodal admittance matrix of the power system to analyze the resonance mode for the conventional power system, where the eigenvalues of the nodal admittance matrix depict the frequencies that system approaches singularity. Then, the impact of the network components on the resonance mode can be quantitatively defined with the resonance peak sensitivity analysis [41]. Since the RMA method requires only the nodal admittance matrix, which can be measured with the frequency scan [66], it aligns well with the impedance-based modeling method.

Thus, the RMA method has been implemented into various multiple-VSC power systems, e.g. in railway networks [42], in microgrids [43], and in wind power plants [44]. However, in these studies, the asymmetrical control dy-

namics of the VSCs are ignored, which may fail to predict the low-frequency resonance modes [11, 32, 33]. In addition, the focus of the existed sensitivity analysis methods are either on the resonance peak magnitude [40, 41] or on the resonance frequency [49], where the damping characteristic of the resonance is ignored.

This chapter discusses first the damping of the resonance in the multi-VSC system in a multi-bus test system with two VSCs served as current sources. Then, to provide guideline for damping enhancement, the modal quality factor sensitivity analysis is introduced. Along with the resonance peak and resonance frequency sensitivities, the impacts of the control parameters in VSCs on the resonance modes can be quantitatively defined. Finally, the nodal admittance matrix of the system incorporates the MIMO impedance models of VSCs is systematically derived using the graph theory [67], and is further analyzed with the modal quality factor sensitivity analysis through the case study.

4.2 Quality Factor in Resonance Mode Analysis

To demonstrate the importance of the quality factor (damping characteristic) in the resonance mode analysis, the resonance mode analysis method in [40] is firstly introduced in brief. In the power system, the relationship between the voltage vector, $[V_\omega]$ and current injection vector, $[I_\omega]$ at different buses can be characterized with the nodal admittance matrix $[Y_\omega]$, which is varied with the frequency points ω as given as

$$[V_\omega] = [Y_\omega]^{-1} [I_\omega] \tag{4.1}$$

Since the vectors, $[V_\omega]$ and $[I_\omega]$ have the same dimensions, which leads to a square matrix of $[Y_\omega]$ that can be diagonalized with the eigenvalue analysis as given as

$$[Y] = [L] [\Lambda] [T] \tag{4.2}$$

where ω is discarded for simplification, but keep in mind that $[Y]$, $[V]$, and $[I]$ are frequency-dependent. The $[L]$ and $[T]$ are the left and right eigenvector matrices of $[Y]$, respectively. Since $[L] = [T]^{-1}$, with the modal voltage vector, $[U] = [T] [V]$, and the modal current vector, $[J] = [T] [I]$, the equation (4.1) can be written as

$$[U] = [\Lambda]^{-1} [J] \tag{4.3}$$

where $[\Lambda]^{-1} = diag\left(\lambda_1^{-1}, \cdots, \lambda_k^{-1}, \cdots\right)$, and then, the relationship between the first modal voltage, U_1, and the first modal current, J_1, can be just defined with λ_1^{-1}, which is also called the modal impedance of mode 1, $Z_{m,1}$. Thus, if one of the eigenvalues approaches singular, the corresponding modal

Table 4.1: Parameters used in experiment and case studies. Source: [J3]

Symbol	Parameter Description	Value
v_g	Grid voltage	400 V_{rms}
P_1,P_2	Output power of VSCs	3.5 kW
f_1	Fundamental frequency	50 Hz
T_s	Sampling period	100 µs
L_1	Converter side inductor	3 mH
L_2	Grid side inductor	1 mH
$C_{f,1}$	Filter capacitor of VSC 1	10 µF
$C_{f,2}$	Filter capacitor of VSC 2	15 µF
y_{12}	Impedance of line 1	1 mH
y_{23}	Impedance of line 2	4 mH
y_{31}	Impedance of line 3	2 mH
y_g	Grid impedance	1.5 mH
K_r	Resonant gain in CC	1000 Ω/s
$K_{p,1}$	Proportional gain in CC of VSC 1	25 Ω
		28 Ω
$K_{p,2}$	Proportional gain in CC of VSC 2	15.5 Ω

impedance approaches infinite leading to an unstable system, i.e., a small current injection can excite a large voltage. Due to the singularity of the modal impedances, the magnitude of the modal impedance becomes the main focus in the previous researches [40, 41].

In the conventional resonance mode analysis, the network contains only the passive components, e.g., resistors, capacitors, and inductors. Yet, due to the control dynamics, the input admittance of the VSC may have negative resistance characteristics [25], which is not considered. Therefore, the negative-resistance characteristic of the input admittance of VSCs is considered in [J3] with the system shown in Fig. 4.1, which has two grid-connected VSCs connected at Bus 1 and Bus 3 and the transmission lines between buses are named as Line 1, Line 2, and Line 3.

The details of the control diagram of VSCs and the derivation of the input admittances can be found in [J3]. The PR current controllers are implemented in the $\alpha\beta$-frame and only the dynamic of current control loop is considered. It means that by connecting the dc sides of VSCs to the ideal dc voltage sources to eliminate the influence of dc bus control dynamics, and the bandwidth of the PLL, which is used to generate the current command in the $\alpha\beta$-frame, is set to 0.5 Hz to avoid coupling to the current control. With the input admittance of VSCs, y_{clg1} and y_{clg2}, and modeling the transmission lines as admittances, y_{12}, y_{23}, and y_{31}, the network in Fig. 4.2 is derived from Fig. 4.1,

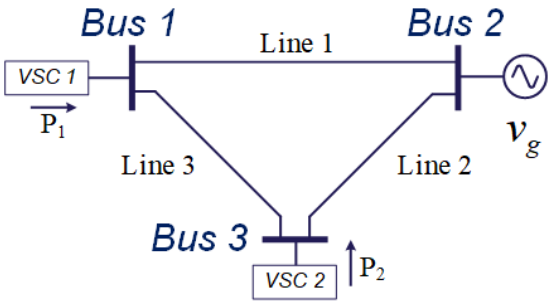

Fig. 4.1: 3-bus test system configuration with two voltage source converters. Source: [J3].

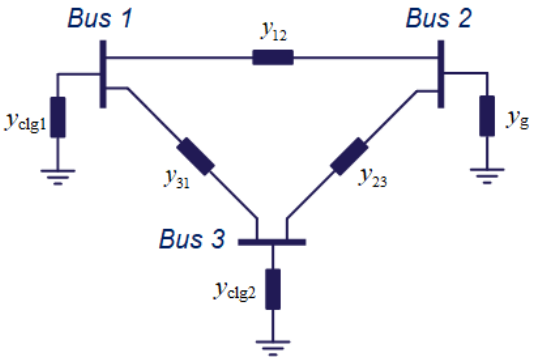

Fig. 4.2: The nodal admittance network representation of Fig. 4.1. Source: [J3].

where its nodal admittance matrix is given as

$$[Y] = \begin{bmatrix} y_{clg1} + y_{12} + y_{31} & -y_{12} & -y_{31} \\ -y_{12} & y_g + y_{12} + y_{23} & -y_{23} \\ -y_{31} & -y_{23} & y_{clg2} + y_{23} + y_{31} \end{bmatrix} \tag{4.4}$$

where $[Y]$ is a 3×3 matrix, and there are 3 modal impedances, $Z_{m,1}$, $Z_{m,2}$, and $Z_{m,3}$, corresponding to the eigenvalues of $[Y]$. The following cases show that the quality factor and the phase information of resonance modes are as important as its magnitude.

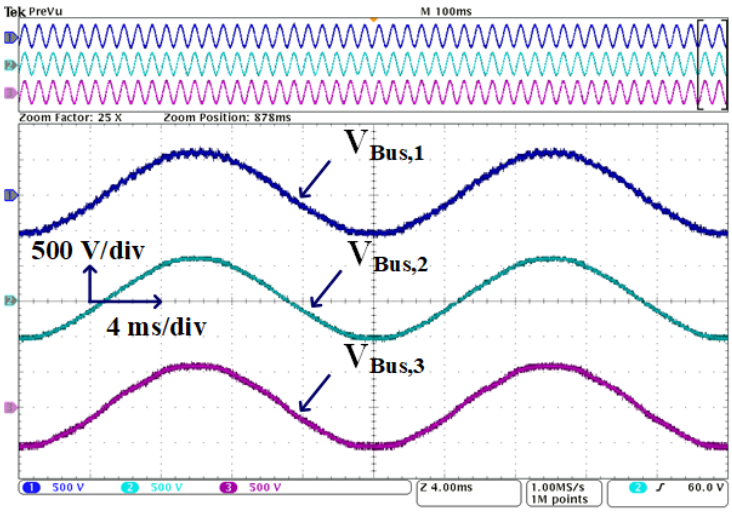

Fig. 4.3: Experimental waveforms of bus voltages in Fig. 4.1 with $K_{p,1} = 25\ \Omega$. Source: [J3].

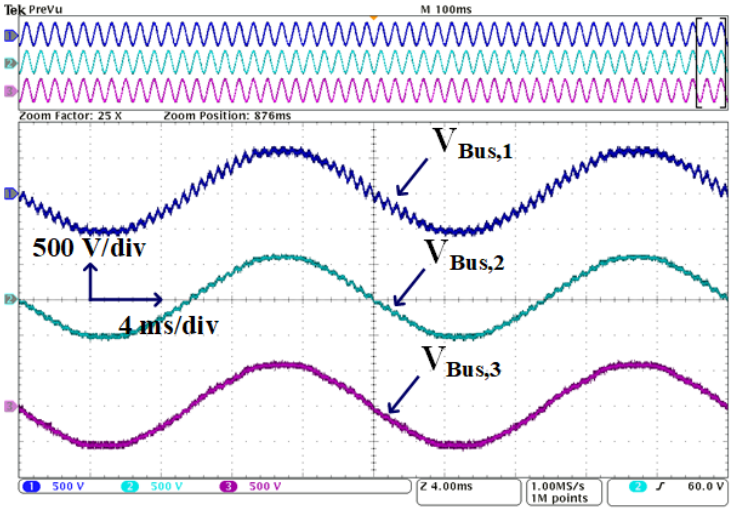

Fig. 4.4: Experimental waveforms of bus voltages in Fig. 4.1 with $K_{p,1} = 28\ \Omega$. Source: [J3].

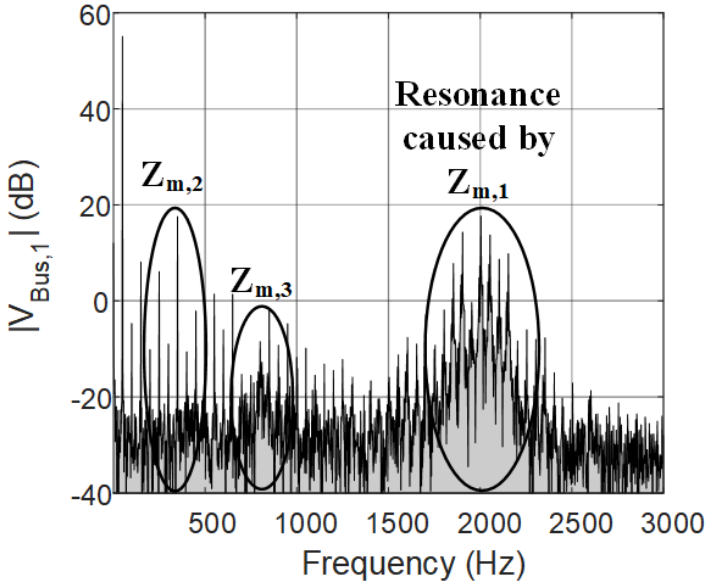

Fig. 4.5: FFT spectrum of $V_{Bus,1}$ in Fig. 4.3. Source: [J3].

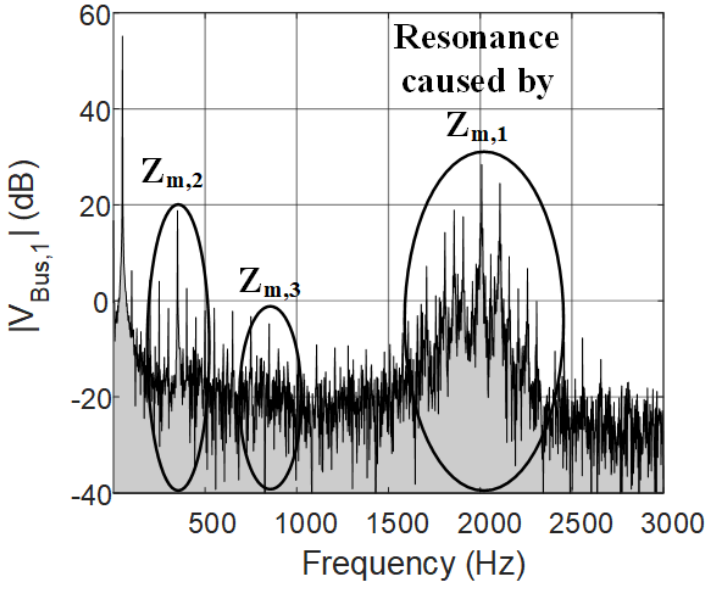

Fig. 4.6: FFT spectrum of $V_{Bus,1}$ in Fig. 4.4. Source: [J3].

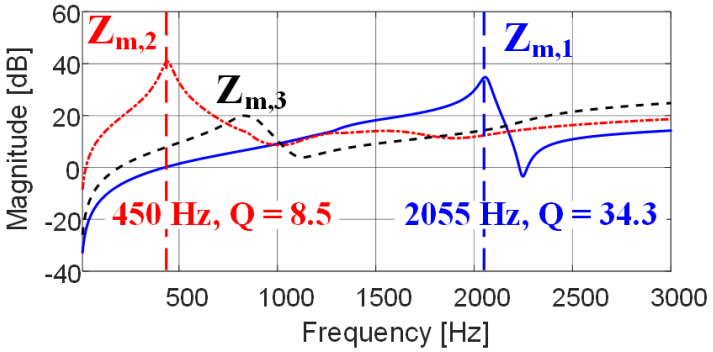

Fig. 4.7: Magnitude-frequency plot of the modal impedacne, Z_m, in the case of Fig. 4.3. Source: [J3].

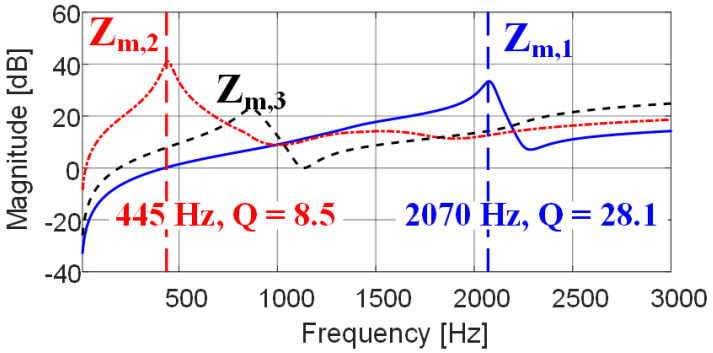

Fig. 4.8: Magnitude-frequency plot of the modal impedacne, Z_m, in the case of Fig. 4.4. Source: [J3].

The parameters used in the case studies are listed in Table 4.1, where the detailed experimental setup is described in [J3]. The measured voltage waveforms with $K_{p,1} = 25\ \Omega$ and $K_{p,1} = 28\ \Omega$ are shown in Fig. 4.3 and Fig. 4.4, respectively, where the frequency-domain spectra of the bus voltage at Bus 1, $V_{Bus,1}$ are plotted in Fig. 4.5 and Fig. 4.6. The frequency spectra show that the voltage harmonics around 2 kHz in the case with $K_{p,1} = 28\ \Omega$ is higher than the case with $K_{p,1} = 25\ \Omega$. However, the magnitude-frequency plots of the modal impedances, $Z_{m,1}$, $Z_{m,2}$, and $Z_{m,3}$, which are shown in Fig. 4.7 and Fig. 4.8, have a different conclusion since the magnitude of resonance mode 1 in the case with $K_{p,1} = 25\ \Omega$ is higher than the magnitude of resonance mode 1 in the case with $K_{p,1} = 28\ \Omega$. The conventional RMA method may conclude that the case with $K_{p,1} = 25\ \Omega$ is closer to instability than the case with $K_{p,1} = 28\ \Omega$, which is not correct.

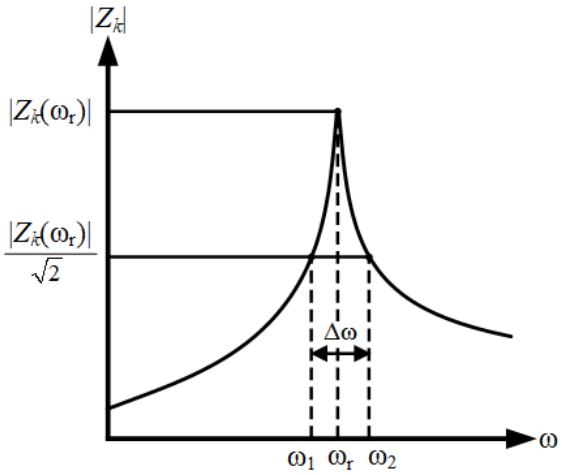

Fig. 4.9: Modal impedance Z_k plotted in the magnitude-frequency plot.. Source: [J4].

4.2.1 Modal Quality Factor

Peak-Picking Method

The derivation of quality factor, Q, is explained first. To plot a modal impedance Z_k in the magnitude-frequency plot as shown in the schematic diagram in Fig. 4.9, which is generally used in the conventional RMA method [40,41,49], is called the *Peak-Picking* method in the *Modal Analysis* [68]. In the *Peak-Picking* method, the Q is derived with the *Half-Power* method, which firstly identifies the frequency with the largest impedance magnitude, ω_k. Then, the other two frequency points, ω_1 and ω_2, with the values are equal to half of $|Z_k(\omega_k)|$, are identified. The quality factor Q can then be estimated as

$$Q \approx \frac{\omega_k}{\omega_2 - \omega_1} = \frac{\omega_k}{\Delta\omega} \tag{4.5}$$

where $\Delta\omega$ is also called the resonance bandwidth. Using (4.5), the Q identified in Fig. 4.7 and Fig. 4.8 are 34.3 and 28.1, respectively. However, the Q derived in this method is always positive because of the magnitude-frequency plot shows only part of the information about how the impedance change along the frequency.

Circle-Fit Method

Alternatively, the Z_k can be plotted in the polar plot as shown in the schematic diagram in Fig. 4.10, where this method is called *Circle-Fit* method. The general principle of *Circle-Fit* method is illustrated as follows: Since the modal

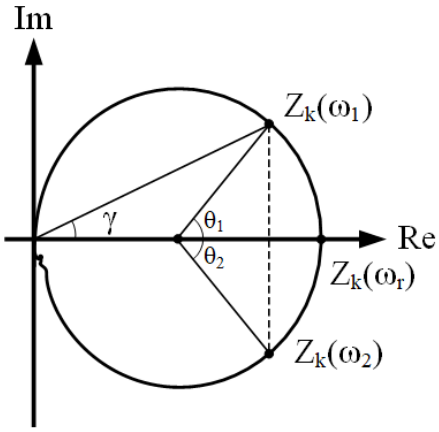

Fig. 4.10: Modal impedance Z_k plotted in the polar plot. Source: [J4].

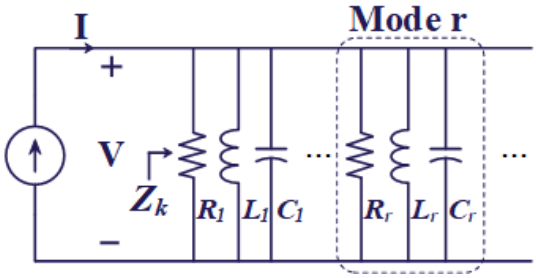

Fig. 4.11: Modal impedance Z_k represented as multiple parallel *RLC* circuits. Source: [J4].

impedances are linear combinations of the entries in the nodal admittance matrix, Z_k may contain multiple resonance modes in the wide frequency range. Thus, each resonance mode is represented as a RLC second-order circuit, and then Z_k can be represented by multiple paralleled RLC circuits to cover the dynamics in the wide frequency range as shown in Fig. 4.11. Even if Z_k consists of multiple resonance modes, each resonance mode dominates the dynamics of Z_k in the specific frequency range [40]. To be noticed that, the values of the resistances in Fig. 4.11, R_1 and R_r can be negative if the VSCs are in the system due to the negative-resistance characteristic of VSCs' control dynamics described in [J3].

The analytic equation of Fig. 4.11 can be derived as [68]

$$Z_k(\omega) = \sum_{r=1}^{N} \frac{j\omega A_r}{\omega_{k,r}^2 - \omega^2 + \frac{\omega_{k,r}^2}{Q_r} j} \tag{4.6}$$

where Q_r is the quality factor, $\omega_{k,r}$ is the resonance frequency, and A_r is the modal complex constant of the r^{th} resonance mode in Z_k. Since the r^{th} mode dominates the dynamics around $\omega_{k,r}$, equation (4.6) can be written as

$$Z_k(\omega) = \frac{j\omega A_r}{\omega_{k,r}^2 - \omega^2 + \frac{\omega_{k,r}^2}{Q_r} j} + \sum_{\substack{S=1 \\ S \neq r}}^{N} \frac{j\omega A_s}{\omega_{k,s}^2 - \omega^2 + \frac{\omega_{k,s}^2}{Q_s} j} \tag{4.7}$$

where the summation term can be estimated as a complex number, B_k, since the r^{th} mode dominates the dynamics around $\omega_{k,r}$. Thus, equation (4.6) can be simplified as

$$Z_k(\omega) \approx \frac{j\omega A_r}{\omega_{k,r}^2 - \omega^2 + \frac{\omega_{k,r}^2}{Q_r} j} + B_k \tag{4.8}$$

where B_k can be neglected considering the dominance of the r^{th} mode, and $s = j\omega$. Equation (4.8) can be written as

$$Z_k(s) \approx \frac{A_r}{s^2 + \frac{\omega_{k,r}}{Q_r} s + \omega_{k,r}^2} \tag{4.9}$$

where the relationships between quality factor Q_r, damping ratio ζ_r, and exponential attenuation time constant τ_r are given as

$$Q_r = \frac{1}{2\zeta_r} = \frac{\tau_r \omega_{k,r}}{2} \tag{4.10}$$

where Q_r and ζ_r are defined at frequency $\omega_{k,r}$, which are useful in the frequency domain analysis. On the other hand, τ_r can be used to estimate the time that resonance sustain in the system, which is derived as

$$\tau_r = \frac{2Q_r}{\omega_{k,r}} = \frac{1}{\pi} \frac{Q_r}{f_{k,r}} \tag{4.11}$$

where $f_{k,r}$ represents the resonance frequency in Hz. The resonance decays with the envelope of $e^{-\frac{t}{\tau_r}}$, i.e. the resonance decays to 36.8% of its initial value after one time constant, $1/e \approx 0.368$ [J4].

Remark (Importance of quality factor in resonance mode analysis)
It is worth noting that the magnitude of A_r is determined by $\left|Z_k(\omega_{k,r})\right|$, $\omega_{k,r}$, and Q_r given as

$$|A_r| = \left|Z_k(\omega_{k,r})\right| \frac{\omega_{k,r}}{Q_r} \tag{4.12}$$

where the $\left|Z_k(\omega_{k,r})\right|$ describes the resonance magnitude, $\omega_{k,r}$ represents the resonance frequency, and Q_r describes the damping characteristic of the resonance, these parameters are all important when analyzing a resonance mode.

Since the second-order system has the circularity on the complex plane [68] as shown in Fig. 4.10, $\tan\gamma$ can be derived from (4.8) neglecting B_k as

$$\tan\gamma = \tan\frac{\theta}{2} = \frac{\mathrm{Im}\left(Z_k\right)}{\mathrm{Re}\left(Z_k\right)} = \frac{\omega_k^2 - \omega^2}{\frac{\omega_k^2}{Q}} \tag{4.13}$$

where γ is the inscribed angle, θ is the central angle, and $\gamma = \frac{\theta}{2}$. Thus, Q can be calculated by two frequency points on the circle that one point is before the ω_k and the other one is after ω_k as given as

$$Q = \frac{\omega_k^2}{\omega_2^2 - \omega_1^2}\left(\tan\frac{\theta_2}{2} + \tan\frac{\theta_1}{2}\right) \tag{4.14}$$

By taking the points $\omega_1 = \omega_k - \Delta\omega$ and $\omega_2 = \omega_k + \Delta\omega$, the Q can be derived using the small angle approximation of tan as

$$Q = \frac{\omega_k^2}{\left(\omega_k + \Delta\omega\right)^2 - \left(\omega_k - \Delta\omega\right)^2}\left(\tan\frac{\Delta\theta}{2} + \tan\frac{\Delta\theta}{2}\right) \approx \frac{\omega_k}{4}\frac{\Delta\theta}{\Delta\omega} = -\frac{\omega_k}{2}\frac{\Delta\gamma}{\Delta\omega} \tag{4.15}$$

where the Q is determined at the frequency ω_k and the direction of Z_k in Fig. 4.10 is clockwise, which means that the frequency change, $\Delta\omega$, leads to the phase change in the Z_k, $-2\Delta\gamma$.

Remark (Importance of phase information on the quality factor of resonance mode)
It is clear depicted in (4.15) that the magnitude-frequency plot is not enough to derive the quality factor, which also requires the phase information of the modal impedance.

Since the Q have to be determined at frequency point ω_k, the value of ω_k is required to derive first, where a sophisticated MATLAB/SciLab-based toolbox for the experimental modal analysis developed in [69], which uses the experimental data to derive the resonance frequency and quality factor, is used to plot the modal impedances in the polar plots as shown in Fig. 4.12 and Fig. 4.13. Thus, the quality factors of $Z_{m,1}$ can be derived as 32.6 in the case with $K_{p,1} = 25\ \Omega$ and -28.4 in the case with $K_{p,1} = 28\ \Omega$ using (4.15). The Q derived in the case of $K_{p,1} = 28\ \Omega$ is negative due to the direction of modal impedance $Z_{m,1}$ is counterclockwise, which cannot be explained in the magnitude-frequency plot. To be noticed that negative value of quality factor exists in the system containing active components, e.g. the current amplifier [70], where the VSCs with the negative-resistance characteristics serve as the active components in the power system.

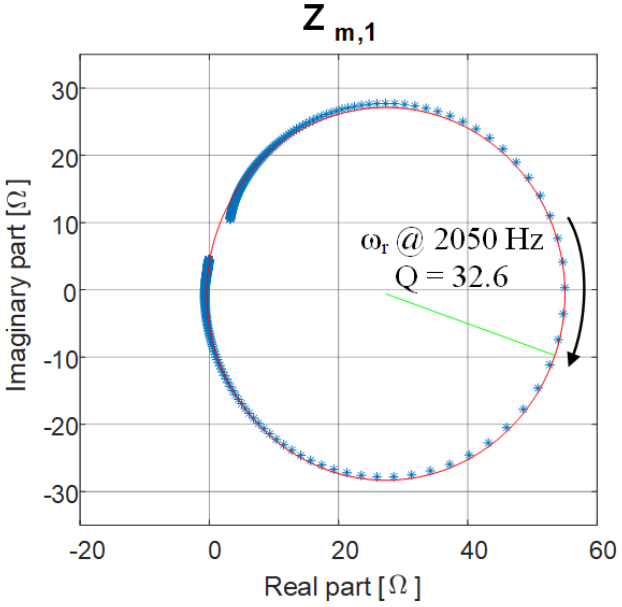

Fig. 4.12: Polar plot of the modal impedacne, Z_m, in the case of Fig. 4.3.

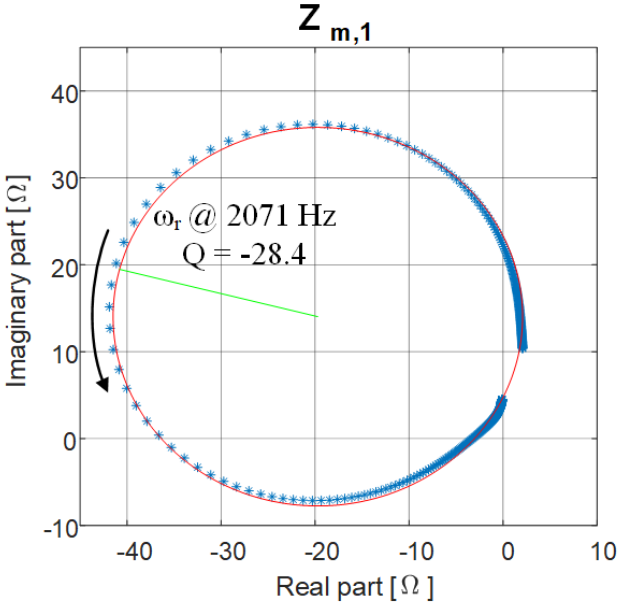

Fig. 4.13: Polar plot of the modal impedacne, Z_m, in the case of Fig. 4.4.

4.3 Modal Quality Factor Sensitivity Analysis

As discussed in Chapter 4.2.1, the resonance magnitude $\left|Z_k\left(\omega_{k,r}\right)\right|$, the resonance frequency $\omega_{k,r}$, and the quality factor Q_r are all important at analyzing a resonance mode, where the previous researches have already examined the modal sensitivity on the impact of one network component, α, e.g. shunt capacitors, to the magnitude [41] and to the frequency [49]. Yet, the modal sensitivity of the quality factor is overlooked, and it becomes the focus in this PhD project. The modal impedance magnitude sensitivity [41], modal frequency sensitivity [49], and modal quality factor sensitivity indices can be defined as

$$\begin{aligned}\frac{d\left|Z_k\right|}{d\alpha} &= \lim_{\Delta\alpha\to 0}\frac{\Delta\left|Z_k\right|}{\Delta\alpha}\\ \frac{d\omega_k}{d\alpha} &= \lim_{\Delta\alpha\to 0}\frac{\Delta\omega_k}{\Delta\alpha}\\ \frac{dQ}{d\alpha} &= \lim_{\Delta\alpha\to 0}\frac{\Delta Q}{\Delta\alpha}\end{aligned} \tag{4.16}$$

where $Z_k = \frac{1}{\lambda_k}$. The modal impedance magnitude sensitivity [41] and modal frequency sensitivity [49] are given as

$$\begin{aligned}\frac{d\left|Z_k\right|}{d\alpha} &= \left.\frac{\partial\left|Z_k\right|}{\partial\alpha}\right|_{\omega=\omega_k} = -\frac{1}{\left|\lambda_k\right|^2}\left.\frac{\partial\left|\lambda_k\right|}{\partial\alpha}\right|_{\omega=\omega_k}\\ \frac{d\omega_k}{d\alpha} &= -\frac{\dfrac{\partial^2\left|\lambda_k\right|}{\partial\omega\partial\alpha}}{\dfrac{\partial^2\left|\lambda_k\right|}{\partial\omega^2}}\end{aligned} \tag{4.17}$$

From (4.15), the modal quality factor sensitivity can be derived as

$$\frac{dQ}{d\alpha} = -\frac{\omega_k}{2}\left.\frac{\partial^2\gamma}{\partial\omega\partial\alpha}\right|_{\omega=\omega_k} \tag{4.18}$$

where γ can be derived from the real part and imaginary part of Z_k as

$$\gamma = \arctan\left(\frac{\mathrm{Im}\left(Z_k\right)}{\mathrm{Re}\left(Z_k\right)}\right) \tag{4.19}$$

where Z_k can be written with eigenvalue $\lambda_k = \lambda_r + j\lambda_i$ as

$$Z_k = \frac{1}{\lambda_k} = \frac{1}{\lambda_r + j\lambda_i} = \frac{\lambda_r}{\lambda_r^2+\lambda_i^2} - j\frac{\lambda_i}{\lambda_r^2+\lambda_i^2} \tag{4.20}$$

Thus, the modal quality factor sensitivity can then be derived as

$$\begin{aligned}\frac{dQ}{d\alpha} &= -\frac{\omega_k}{2}\frac{\partial}{\partial\alpha}\left(\frac{\arctan\left(-\frac{\lambda_i}{\lambda_r}\right)}{\partial\omega}\right) \\ &= -\frac{\omega_k}{2}\frac{\partial}{\partial\alpha}\left(\frac{\arctan\left(-\frac{\lambda_i^{\omega_k+\Delta\omega}}{\lambda_r^{\omega_k+\Delta\omega}}\right)-\arctan\left(-\frac{\lambda_i^{\omega_k-\Delta\omega}}{\lambda_r^{\omega_k-\Delta\omega}}\right)}{2\Delta\omega}\right)\end{aligned} \tag{4.21}$$

where the quality factor sensitivity at ω_k can be derived with two frequency points, $\omega_k + \Delta\omega$ and $\omega_k - \Delta\omega$.

$$\begin{aligned}\frac{dQ}{d\alpha} =& \frac{\omega_k}{4\Delta\omega}\left(\frac{\lambda_i^{\omega_k-\Delta\omega}}{\left|\lambda_k^{\omega_k-\Delta\omega}\right|^2}\frac{\partial\lambda_r^{\omega_k-\Delta\omega}}{\partial\alpha} - \frac{\lambda_r^{\omega_k-\Delta\omega}}{\left|\lambda_k^{\omega_k-\Delta\omega}\right|^2}\frac{\partial\lambda_i^{\omega_k-\Delta\omega}}{\partial\alpha}\right) \\ &- \frac{\omega_k}{4\Delta\omega}\left(\frac{\lambda_i^{\omega_k+\Delta\omega}}{\left|\lambda_k^{\omega_k+\Delta\omega}\right|^2}\frac{\partial\lambda_r^{\omega_k+\Delta\omega}}{\partial\alpha} - \frac{\lambda_r^{\omega_k+\Delta\omega}}{\left|\lambda_k^{\omega_k+\Delta\omega}\right|^2}\frac{\partial\lambda_i^{\omega_k+\Delta\omega}}{\partial\alpha}\right)\end{aligned} \tag{4.22}$$

According to (4.11), the damping characteristic of system can be enhanced by reducing τ that indicates higher resonance decaying rate, where τ is proportional to Q. Thus, the aim is to decrease the quality factor with the change of system component α. From (4.22), to reduce Q of the modal impedance at ω_k means to reduce the slope of angle at ω_k, which is equal to reduce the difference between $\angle Z_k(\omega_k - \Delta\omega)$ and $\angle Z_k(\omega_k + \Delta\omega)$.

To derive $\frac{\partial\lambda_k}{\partial\alpha}$ corresponding to the entry in the nodal admittance matrix $[Y]$ in (4.2), $[Y]$ can be presented with its left and right eigenvectors, t_k and l_k, of λ_k [41] as

$$\frac{\partial\lambda_k}{\partial\alpha} = t_k\frac{\partial[Y]}{\partial\alpha}l_k \tag{4.23}$$

where if α is the (i,j) entry in $[Y]$, the eigenvalue sensitivity to α can be derived as

$$\frac{\partial\lambda_k}{\partial\alpha} = \frac{\partial\lambda_k}{\partial y_{ij}} = t_k\frac{\partial[Y]}{\partial y_{ij}}l_k = t_{ki}l_{jk} \tag{4.24}$$

Thus, the sensitivity matrix, S_λ, has been defined in [41] as

$$S_\lambda = l_k t_k \tag{4.25}$$

where it means that the eigenvalue sensitivity to y_{ij} is the (j,i) entry in S_λ given as

$$\frac{\partial\lambda}{\partial y_{ij}} = S_{\lambda,ji} \tag{4.26}$$

In the nodal admittance matrix $[Y]$, the components can be categorized as shunt components, y_{sh}, at bus i or series components, y_{se}, between buses i and j, wher the sensitivity to the shunt and series components are given here for easily following as [41]

$$\frac{\partial \lambda}{\partial y_{sh}} = S_{\lambda,ii} \tag{4.27}$$

$$\frac{\partial \lambda}{\partial y_{se}} = S_{\lambda,ii} + S_{\lambda,jj} - S_{\lambda,ij} - S_{\lambda,ji} \tag{4.28}$$

Thus, for the shunt components, $S_{\lambda,ii} = S_r + jS_i$, $y_{sh} = G + jB$

$$\begin{aligned} \frac{\partial \lambda_r}{\partial G} &= S_r & \frac{\partial \lambda_i}{\partial G} &= S_i \\ \frac{\partial \lambda_r}{\partial B} &= -S_i & \frac{\partial \lambda_i}{\partial B} &= S_r \end{aligned} \tag{4.29}$$

Then, the modal quality sensitivity can be quantitatively derived using (4.29 into (4.22). For the series components, the complex number of (4.28) should be derived, where their values can be utilized in (4.22) to derive the modal quality sensitivity index.

4.4 Case Study of Multi-VSC System

The case in Chapter 4.2 is used to bring attention to the negative-resistance characteristics of VSCs. Yet, to fully explore the possible values of ω_k, λ_r, and λ_i and to show the effectiveness of using the modal quality sensitivity index in (4.22) in the multi-VSC systems, the case with the system shown as Fig. 3.3 in Chapter 3.4 is employed to show the impact of changing the control parameters in the VSCs to the resonances and it is illustrated in Fig. 4.14 .

The nodal admittance matrix, which can preserve the asymmetrical control dynamics of VSCs, is required. The two-port network with Y-parameters elaborated in Chapter 2.2 is used. For each two-port network with Y-parameters, the two-port network contains four elements, e.g., two admittances and two voltage-controlled current sources, the number of components in the multi-VSC system increases rapidly with the number of VSCs and the transmission lines. Thus, the graph theory is applied to derive the nodal admittance matrix composed of two-port networks detailed in [C4]

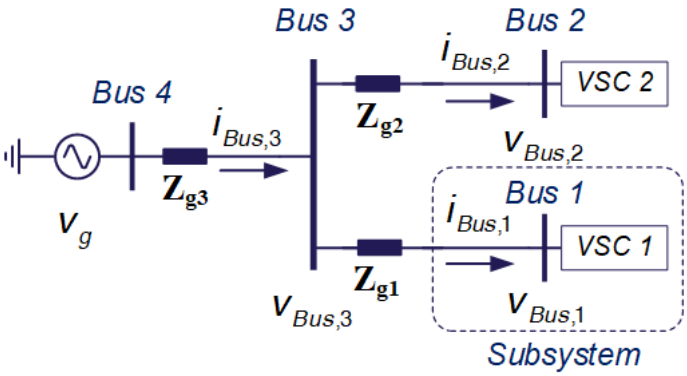

Fig. 4.14: System configuration with multi-grid-connected VSCs shown in Fig. 3.3. Source: [J4]

The small signal model of the system in Fig. 4.14 can be described with the two-port networks with Y-parameters as shown in Fig. 4.15. To describe a directed graph G with the graph theory [67], the graph should be defined as the composition of a set of vertices V connected by a set of edges E, where the vertices and edges in Fig. 4.15 are defined as

- V: Voltage vectors $v_{Bus,1}$, $v_{Bus,2}$, $v_{Bus,3}$, $v_{Bus,4}$, and ground
  - Bus 1: Vertices v_5 and v_6
  - Bus 2: Vertices v_7 and v_8
  - Bus 3: Vertices v_2 and v_4
  - Bus 4: Vertices v_1 and v_3
  - Ground: Vertex v_9
- E: Two-port networks of the grid impedances and VSCs, e_1 to e_8
  - Z_{g3}: e_1 and e_2
  - Z_{g2}: e_5 and e_6
  - Z_{g1}: e_3 and e_4
  - VSC 1: e_7
  - VSC 2: e_8

where the two-port network is further defined with two sub-edges since it has two terminals, e.g., $e_{7,1}$ and $e_{7,2}$ represent the two terminals of $[Y_{VSC1}]$. Then, the nodal admittance matrix of the system can be derived with two matrices, which are the oriented incidence matrix, $[B_G]$, and the elementary admittance matrix, $[Y_E]$, as

$$[Y] = [B_G]\,[Y_E]\left[B_G^T\right] \tag{4.30}$$

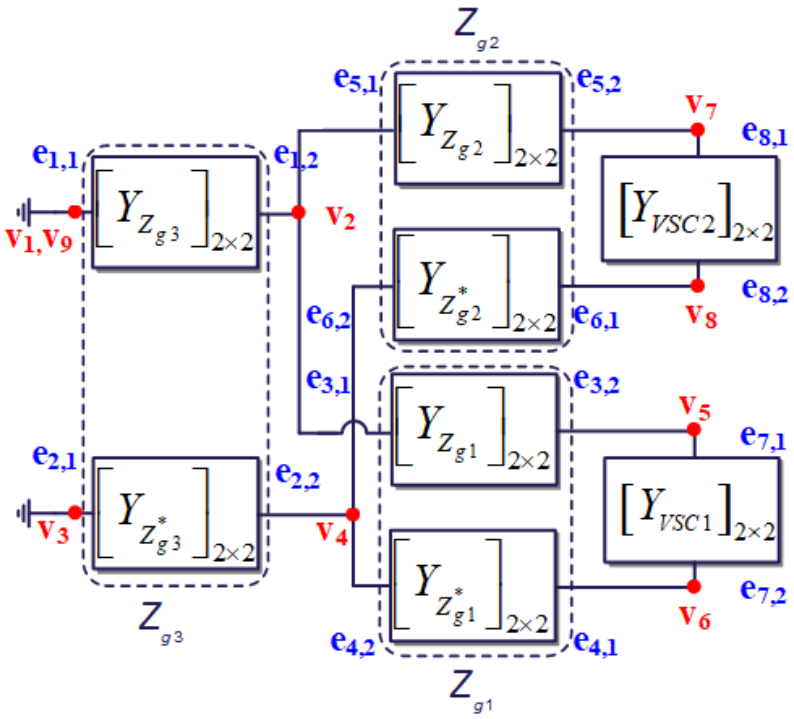

Fig. 4.15: Two-port network connections of the system shown in Fig. 3.3. Source: [J4]

where the (i, j) entry of $[B_G]$ is defined as

- $+1$, if vertex v_j is the target vertex of edge e_i.
- -1, if vertex v_j is the source vertex of edge e_i.
- 0, otherwise

Since for the two-port network with Y-parameters, the current is defined flow into the terminals, i.e., the entries in the rows except for v_9 are either $+1$ or 0, and the entries in the 9^{th} row are either -1 or 0. The example of edges $e_{1,1}$ and $e_{1,2}$ are given as

$$[B_G] = \begin{array}{c} \\ v_1 \\ v_2 \\ \vdots \\ v_9 \end{array} \begin{array}{c} \begin{array}{cccc} e_{1,1} & e_{1,2} & \cdots & \cdots \end{array} \\ \begin{bmatrix} 0 & \cdots & \cdots & \cdots \\ \vdots & +1 & \cdots & \vdots \\ \vdots & \vdots & \ddots & \vdots \\ 0 & -1 & \cdots & \cdots \end{bmatrix} \end{array} \tag{4.31}$$

Table 4.2: Operating points and control parameters of the systems in Fig. 4.14 for case studies. Source: [J4].

Symbol	Parameter Description	Value
$i_{d,1}^{ref}$	d-axis current command of VSC 1 VSC 2	11.5 A
$i_{d,2}^{ref}$	d-axis current command of VSC 2	7 A→11.5 A (Step change)
i_{q}^{ref}	q-axis current command of VSC 1 and VSC 2	0 A
$K_{pp,1}$	Proportional gain in PLL of VSC 1	1 rad/(V s)
$K_{pi,1}$	Integral gain in PLL of VSC 1	100 rad/(V s^2)
$K_{pp,2}$	Proportional gain in PLL of VSC 2	1 rad/(V s) or 1.1 rad/(V s)
$K_{pi,2}$	Integral gain in PLL of VSC 2	250 rad/(V s^2) or 225 rad/(V s^2)

where the detailed oriented incidence matrix can be found in [C4].

The elementary matrix, $[Y_E]$, is rather simple, which is the direct sum of the two-port network admittance matrices given as

$$[Y_E] = \left[Y_{Z_{g3}}\right] \oplus \left[Y_{Z_{g3}^*}\right] \oplus \left[Y_{Z_{g1}}\right] \oplus \left[Y_{Z_{g1}^*}\right] \\ \left[Y_{Z_{g2}}\right] \oplus \left[Y_{Z_{g2}^*}\right] \oplus [Y_{VSC1}] \oplus [Y_{VSC2}] \tag{4.32}$$

The following two simplifications can be applied to $[B_G]$ with basic matrix operations: 1) The last row, v_9, can be eliminated by row reduction since the sum of the full column in $[B_G]$ is equal to zero. 2) The buses v_1 and v_3 are connected to ideal voltage source in Fig. 4.14, where they are connected to the ground, which is v_9, in the small-signal model in Fig. 4.15, so they can also be discarded with the row reduction. Finally, the resulting nodal admittance matrix is a 6×6 matrix instead of a 9×9 matrix. Because the asymmetrical control dynamics of the VSCs are preserved in the two-port network representations, the nodal admittance matrix also inherits these dynamics.

In the experiments and the theoretical analysis, the parameters in Table 3.1 and Table 4.2 are used in the system in Fig. 4.14. To show the damping characteristics of the system, a step change of the d-axis current command from 7 A→11.5 A is applied in experiments. Three cases are studied with different value of $K_{pp,2}$ or $K_{pi,2}$, where $K_{pp,1} = 1$ rad/(V s) and $K_{pi,1} = 250$ rad/(V s^2) are kept the same in all cases. The cases are as follows:

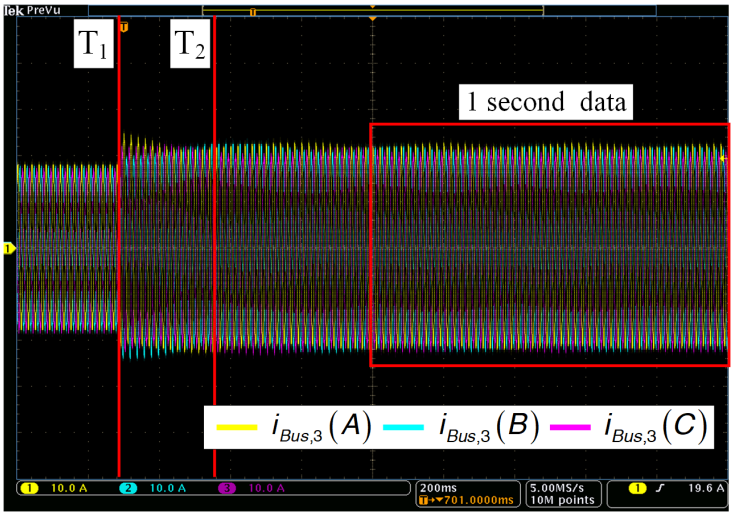

Fig. 4.16: Three phase current waveforms on Bus 3 in Fig. 4.14 (X-axis: 200 ms/*div*, Y-axis: 10 A/*div*). Source: [J4].

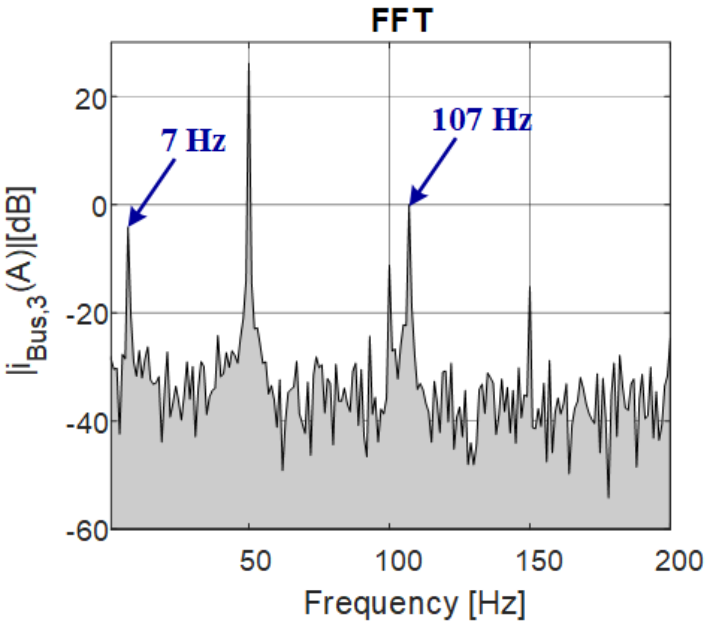

Fig. 4.17: Frequency spectrum of the current $i_{Bus,3}(A)$ in Fig. 4.16. Source: [J4].

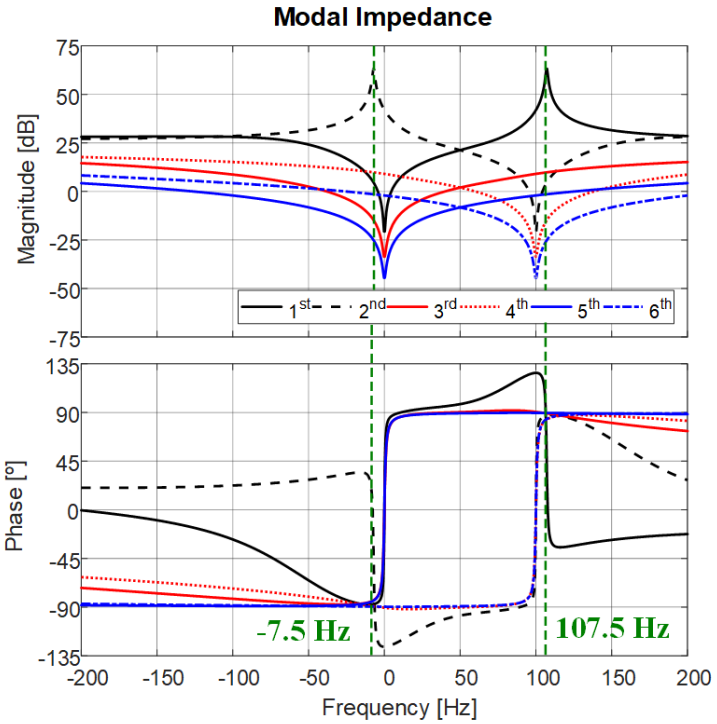

Fig. 4.18: Modal Impedances in the Fig. 4.15 using the parameters in Table 3.1. Source: [J4].

Case I: $K_{pp,2} = 1$ rad/(V s) **and** $K_{pi,2} = 250$ rad/(V s^2)

Fig. 4.16 shows the transient response of three phase current waveforms at Bus 3, $i_{Bus,3}(A)$, $i_{Bus,3}(B)$, and $i_{Bus,3}(C)$ in Fig. 4.14, where a step change of $i_{d,2}^{ref}$ from 7 A to 11.5 A is applied at the time constant T_1. A low frequency resonance can be observed, where the last 1 second data in Fig. 4.16 are used to derive the frequency spectrum of $i_{Bus,3}(A)$ with discrete Fourier transform (DFT) illustrated in Fig. 4.17. Two resonance frequencies, 7 Hz and 107 Hz are identified. By deriving the nodal admittance matrix using (4.30) and applying the eigenvalue analysis, the six modal impedances are derived, and they are plotted in Fig. 4.18 with two critical modes identified at 107.5 Hz in the 1^{st} modal impedance and -7.5 Hz in the 2^{nd} modal impedance validating the experimental results.

To investigate the quality factors of the resonances, the 1^{st} and 2^{nd} modal impedances are plotted in the polar plots shown in Fig. 4.19 and Fig. 4.20, which are 86.5 and 6, respectively. Thus, with (4.11), the exponential attenuation time constants of 1^{st} resonance mode and 2^{nd} resonance mode, τ_1 and

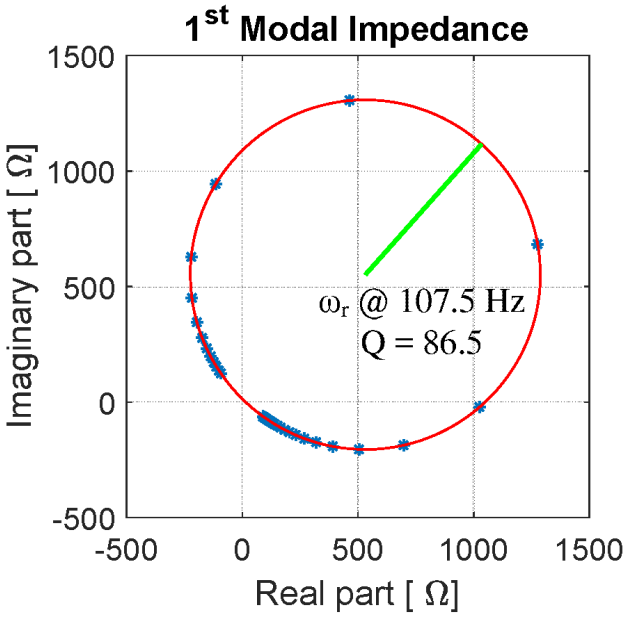

Fig. 4.19: Polar plot of the modal impedacne, Z_m, in the case of Fig. 4.3.

τ_2 can be calculated as

$$\tau_1 = \frac{1}{\pi}\frac{86.5}{107.5} \cong 0.26 \text{ s}$$
$$\tau_2 = \frac{1}{\pi}\frac{6}{7.5} \cong 0.255 \text{ s} \tag{4.33}$$

where two modes have similar exponential attenuation time constants of 0.26 s, and the time constant $T_2 = T_1 + 0.26$ s is shown in Fig. 4.16.

To enhance the damping characteristic of these resonance modes and to determine the component on which bus has the greatest impact on the resonance, the participation factors (PF) are derived at each bus for both modes and they are listed in Table 4.3, where the description of PF can be found in [J4]. The PFs for the 1^{st} mode and the 2^{nd} mode can be ordered as followed:

- For the 1^{st} mode at 107.5 Hz, $v_7 > v_5 > v_2 \gg v_4 = v_6 = v_8$.
- For the 2^{nd} mode at -7.5 Hz, $v_8 > v_6 > v_4 \gg v_2 = v_5 = v_7$.

Thus, the components having the greatest impact to the 1^{st} mode are connected to v_7, and the components having the greatest impact to the 2^{nd} mode are connected to v_8, where the admittance matrix, $[Y_{VSC2}]$, is connected to both v_7 and v_8. Therefore, the entries in the matrix of $[Y_{VSC2}]$ are further investigated with the modal sensitivity analysis.

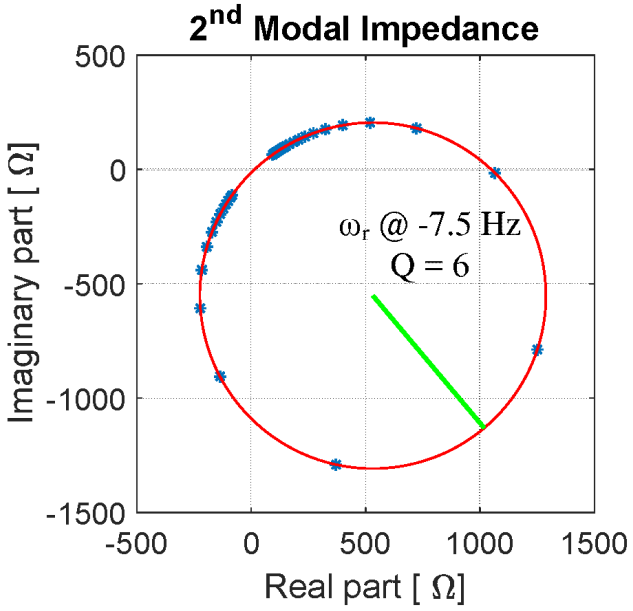

Fig. 4.20: Polar plot of the modal impedacne, Z_m, in the case of Fig. 4.4.

Table 4.3: Participation factors of the 1^{st} and 2^{nd} modes depicted in Fig. 4.18. Source: [J4].

		Participation Factors	
Bus		1^{st} mode at 107.5 Hz	2^{nd} mode at -7.5 Hz
Bus 1	v_5	0.3606	0.0001
	v_6	0.0001	0.3605
Bus 2	v_7	0.3724	0.0001
	v_8	0.0001	0.3725
Bus 3	v_2	0.2655	0.0001
	v_4	0.0001	0.2653

To investigate how the elements in $[Y_{VSC2}]$ impacting the system, the symbolic analytic equations of the entries of $[Y]$ can be derived using (4.30), where four entries in $[Y]$ that contain the elements in $[Y_{VSC2}]$ are given as

$$\begin{aligned}
[Y]_{55} &= [Y_{VSC2}](1,1) + \left[Y_{Z_{g2}}\right](2,2) \\
[Y]_{56} &= [Y_{VSC2}](1,2) \\
[Y]_{65} &= [Y_{VSC2}](2,1) \\
[Y]_{66} &= [Y_{VSC2}](2,2) + \left[Y_{Z^*_{g2}}\right](1,1)
\end{aligned} \tag{4.34}$$

where the eigenvalue sensitivities of λ_1 and λ_2 to the entries in $[Y_{VSC2}]$ can be derived with equations (4.25) and (4.26), and they are given in Table 4.4.

For the 1^{st} mode at 107.5 Hz with $Q = 86.5$, the eigenvalue, λ_1 and the sensitivity index to the $(5,5)$ entry in $[Y]$, $S_{\lambda_1,55}$ at $\omega = \omega_k + \Delta\omega$ and $\omega = \omega_k - \Delta\omega$ are given as

$$\begin{aligned}
\lambda_1\big|_{\omega=\omega_k+\Delta\omega} &= 6.1 \times 10^{-4} - 3.3 \times 10^{-4} j \\
\lambda_1\big|_{\omega=\omega_k-\Delta\omega} &= 3.3 \times 10^{-4} - 5.9 \times 10^{-4} j \\
S_{\lambda_{1,55}}\Big|_{\omega=\omega_k+\Delta\omega} &\cong S_{\lambda_{1,55}}\Big|_{\omega=\omega_k-\Delta\omega} = 0.3722 + 0j
\end{aligned} \tag{4.35}$$

where $\Delta\omega = 0.25 \times 2\pi$, and the imaginary part of $S_{\lambda_1,55}$ is zero, the quality factor difference caused by the changes of G or B, ΔQ_G and ΔQ_B can be derived with (4.22) as

$$\Delta Q_G = \frac{\omega_k}{4\Delta\omega} S_r \left(\frac{\lambda_i^{\omega_k-\Delta\omega}}{\left|\lambda_k^{\omega_k-\Delta\omega}\right|^2} \Delta G_{\omega_k-\Delta\omega} - \frac{\lambda_i^{\omega_k+\Delta\omega}}{\left|\lambda_k^{\omega_k+\Delta\omega}\right|^2} \Delta G_{\omega_k+\Delta\omega} \right) \tag{4.36}$$

$$\Delta Q_B = \frac{\omega_k}{4\Delta\omega} S_r \left(-\frac{\lambda_r^{\omega_k-\Delta\omega}}{\left|\lambda_k^{\omega_k-\Delta\omega}\right|^2} \Delta B_{\omega_k-\Delta\omega} + \frac{\lambda_r^{\omega_k+\Delta\omega}}{\left|\lambda_k^{\omega_k+\Delta\omega}\right|^2} \Delta B_{\omega_k+\Delta\omega} \right) \tag{4.37}$$

Table 4.4: Eigenvalue Sensitivitie of the modes for the system in Fig. 4.14. Source: [J4].

Eigenvalue Sensitivity			
λ_1 at 107.5 Hz		λ_2 at -7.5Hz	
$S_{\lambda_1,55}$	$0.3722 + 0j$	$S_{\lambda_2,55}$	$-2e^{-4} - 7e^{-4}j$
$S_{\lambda_1,56}$	$-0.0117 - 0.0137j$	$S_{\lambda_2,56}$	$-0.0093 + 0.0127j$
$S_{\lambda_1,65}$	$-0.0101 - 0.0135j$	$S_{\lambda_2,65}$	$-0.0108 + 0.0128j$
$S_{\lambda_1,66}$	$-2e^{-4} + 8e^{-4}j$	$S_{\lambda_2,66}$	$0.3721 + 0j$

However, G or B cannot be solely changed since the input admittance of VSCs represents the dynamics of controllers.

Case II: $K_{pp,2} = 1.1$ rad/(V s) **and** $K_{pi,2} = 250$ rad/(V s^2)

The second case is to increase proportional gain in PLL of VSC 2, $K_{pp,2}$, from 1 rad/(V s) to 1.1 rad/(V s), which is equal to 10% increase. Fig. 4.21 shows the real and imaginary parts of $[Y_{VSC2}]\,(1,1)$, where the changes in G and B are given as

$$\begin{aligned} \Delta G^{1-1.1}_{\omega_k+\Delta\omega} &= -1.2\times10^{-3}\ \mho \\ \Delta B^{1-1.1}_{\omega_k+\Delta\omega} &= -2.9\times10^{-3}\ \mho \\ \Delta G^{1-1.1}_{\omega_k-\Delta\omega} &= -1.1\times10^{-3}\ \mho \\ \Delta B^{1-1.1}_{\omega_k-\Delta\omega} &= -3.0\times10^{-3}\ \mho \end{aligned} \tag{4.38}$$

where the value of Q change can be calculated with (4.36) and (4.37) given as

$$\Delta Q_{cal,Kp} = \Delta Q_{G,cal} + \Delta Q_{B,cal} \cong 23.2 - 61.6 = -38.4\ (1^{st}\ mode) \tag{4.39}$$

where the $\Delta G^{1-1.1}_{\omega_k+\Delta\omega}$ and $\Delta G^{1-1.1}_{\omega_k-\Delta\omega}$ are negative that lead to the increasing of Q. Yet, the $\Delta B^{1-1.1}_{\omega_k+\Delta\omega}$ and $\Delta B^{1-1.1}_{\omega_k-\Delta\omega}$ cause the reduction of Q. Fig. 4.23 shows the 1^{st} modal impedance with $K_{pp,2} = 1.1$ derived with the model. The value of Q change, $\Delta Q_{model,Kp} = 41.9 - 86.5 = -44.6$. The difference between $\Delta Q_{cal,Kp}$ and $\Delta Q_{model,Kp}$ is caused by the change of λ_k along with the components in the system change, ΔG and ΔB. To improve the accuracy, the number of frequency scan points around ω_k should be increased, which reduces $\Delta\omega$ in (4.37) and (4.36). The exponential attenuation time constant, $\tau_{1,K_{pp,2}=1.1}$ can be calculated as

$$\tau_{1,K_{pp,2}=1.1} = \frac{1}{\pi}\frac{41.9}{107.5} \cong 120\ \text{ms} \tag{4.40}$$

To validate the theoretical analysis, Fig. 4.25 shows the transient response of three phase current waveforms with $K_{pp,2} = 1.1$ rad/(V s) and $K_{pi,2} = 250$ rad/(V s^2). Comparing with the experimental results in Fig. 4.16, the damping characteristic of system at 107.5 Hz is enhanced, where the system is settled after 120 ms.

Case III: $K_{pp,2} = 1$ rad/(V s) **and** $K_{pi,2} = 225$ rad/(V s^2)

The third case is to reduce integral gain in PLL of VSC 2, $K_{pi,2}$, from 250 rad/(V s) to 225 rad/(V s), which is equal to 10% decrease. Fig. 4.22 shows the real and

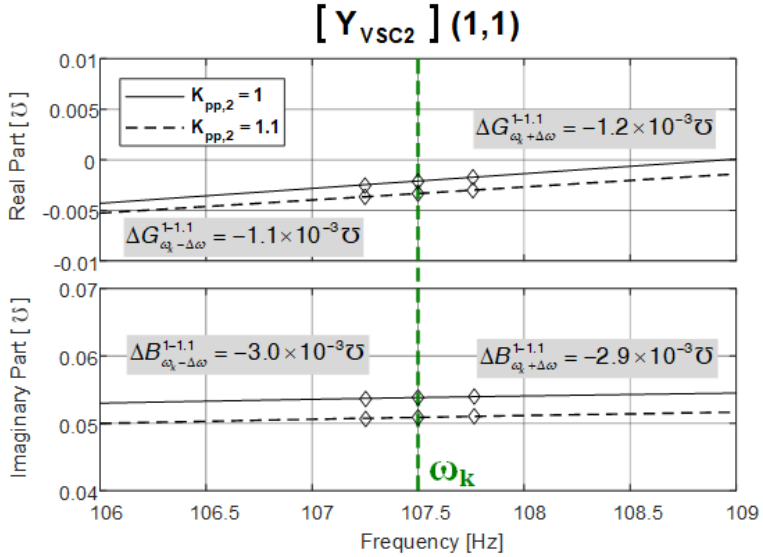

Fig. 4.21: Admittance value of $[Y_{VSC2}]$ $(1,1)$ with different proportional gains in PLL, $K_{pp,2} = 1$ and $K_{pp,2} = 1.1$. Source: [J4].

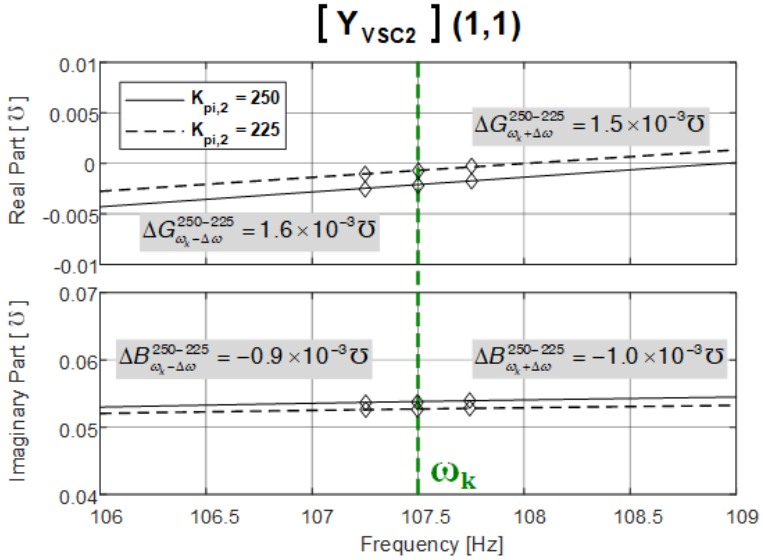

Fig. 4.22: Admittance value of $[Y_{VSC2}]$ $(1,1)$ with different integral gains in PLL, $K_{pi,2} = 250$ and $K_{pi,2} = 225$. Source: [J4].

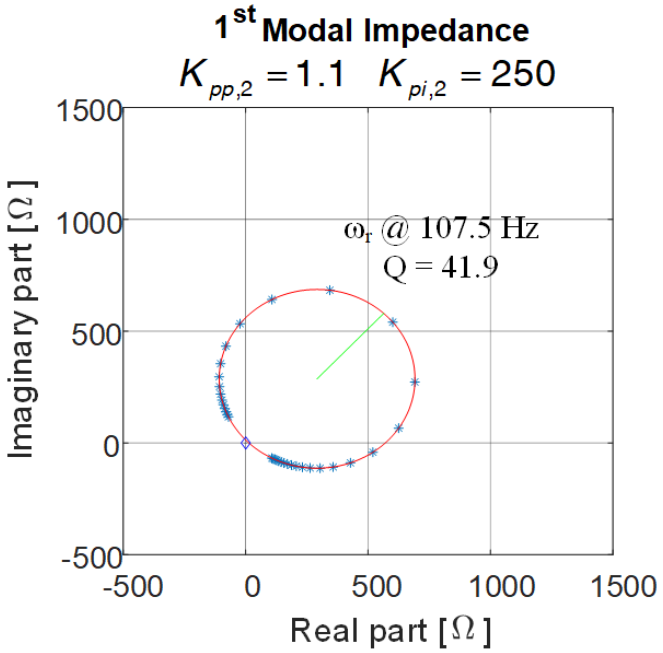

Fig. 4.23: 1^{st} modal impedance with $K_{pp,2} = 1.1$ and $K_{pi,2} = 250$. Source: [J4].

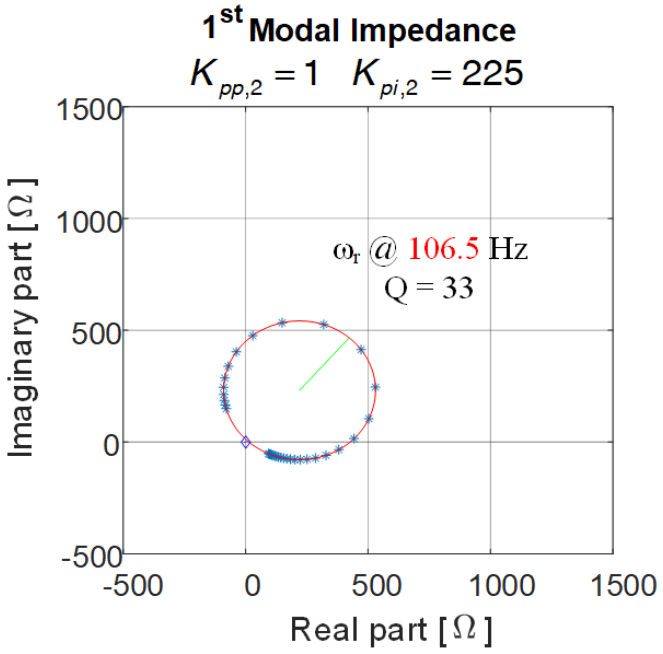

Fig. 4.24: 1^{st} modal impedance with $K_{pp,2} = 1$ and $K_{pi,2} = 225$. Source: [J4].

imaginary parts of $[Y_{VSC2}](1,1)$, where the changes in G and B are given as

$$\begin{aligned}
\Delta G^{250-225}_{\omega_k+\Delta\omega} &= 1.5\times10^{-3}\ \mho \\
\Delta B^{250-225}_{\omega_k+\Delta\omega} &= -1.0\times10^{-3}\ \mho \\
\Delta G^{250-225}_{\omega_k-\Delta\omega} &= 1.6\times10^{-3}\ \mho \\
\Delta B^{250-225}_{\omega_k-\Delta\omega} &= -0.9\times10^{-3}\ \mho
\end{aligned} \tag{4.41}$$

where the value of Q change can be calculated as

$$\Delta Q_{cal,Ki} = \Delta Q_{G,cal} + \Delta Q_{B,cal} \cong -40.8 - 24.8 = -65.6\ (1^{st}\ mode) \tag{4.42}$$

Both the increase of G and decrease of B help to improve the damping of system. The 1^{st} modal impedance with $K_{pi,2} = 225$ derived with the model is plotted in Fig. 4.24, where $\Delta Q_{model,Ki} = 33 - 86.5 = -53.5$. To be noticed that the resonance frequency is decreased from 107.5 Hz to 106.5 Hz, where the modal frequency sensitivity has been reported in [49]. The exponential attenuation time constant, $\tau_{1,K_{pi,2}=225}$ can be calculated as

$$\tau_{1,K_{pi,2}=225} = \frac{1}{\pi}\frac{33}{106.5} \cong 100\ \text{ms} \tag{4.43}$$

where experimental results with $K_{pi,2} = 225$ shown in Fig. 4.26 depict that the damping of system is further enhanced.

For the 2^{nd} mode at -7.5 Hz with $Q = 6$, the same approaches are implemented in [J4], where the same conclusion has been drawn.

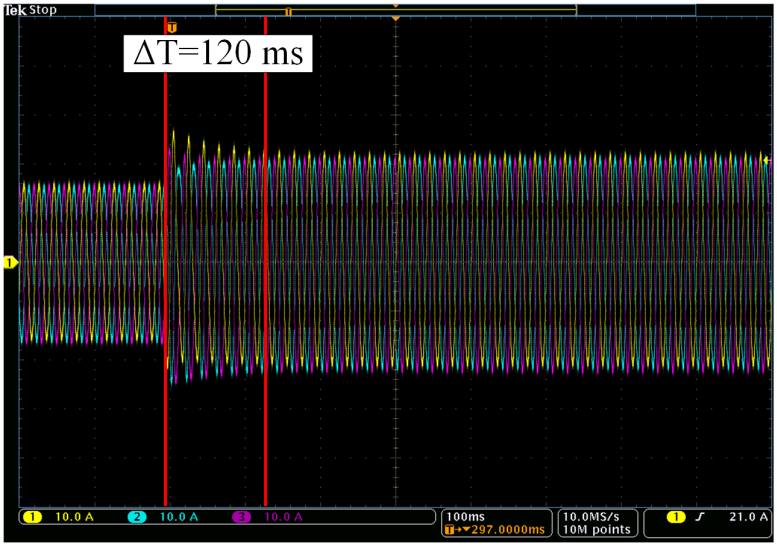

Fig. 4.25: Three phase current waveforms on Bus 3 in Fig. 4.14 with $K_{pp,2} = 1.1$ and $K_{pi,2} = 250$ (X-axis: 100 ms/div, Y-axis: 10 A/div). Source: [J4].

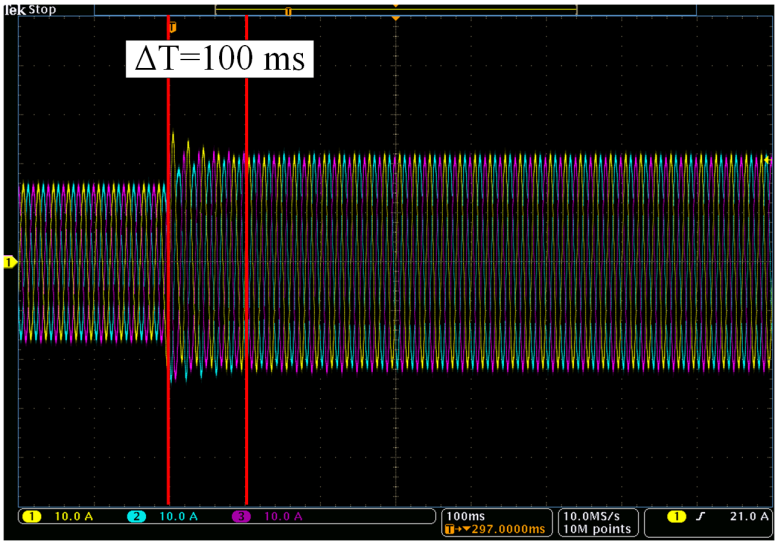

Fig. 4.26: Three phase current waveforms on Bus 3 in Fig. 4.14 with $K_{pp,2} = 1$ and $K_{pi,2} = 225$ (X-axis: 100 ms/div, Y-axis: 10 A/div). Source: [J4].

4.5 Summary

In this chapter, the resonance modes in the multi-VSC system are investigated, where the importance of the phase information of nodal admittance matrix has been elaborated as well as the quality factor of the resonance mode corresponding to the damping characteristic. To analyze the impact of parameters changing in the system on the resonance modes, the modal quality factor sensitivity index has been quantitatively defined. Finally, to preserve the asymmetrical control dynamics of the VSCs, the two-port network modeling method and the graph theory are employed to derive the nodal admittance matrix. The studied case in Chapter 3.4 is used to show the effectiveness, where the resonance can be mitigated with changing the control parameters according to the modal quality factor sensitivity index.

Related Publications

[C4] **S.-F. Chou**, X. Wang, and F. Blaabjerg, "Subsynchronous Resonance Analysis in Multi-Bus Multi-VSC Power System Based on Two-Port Network Modeling Method," *2020 IEEE Energy Conversion Congress and Exposition (ECCE)*, Detroit, MI, USA, 2020, pp. 5696-5702.

[J3] **S.-F. Chou**, X. Wang, and F. Blaabjerg, "Frequency-Domain Modal Analysis for Power-Electronic-Based Power Systems," in *IEEE Trans. Power Electrons.*, vol. 36, no. 5, pp. 4910-4914, May 2021.

[J4] **S.-F. Chou**, X. Wang, and F. Blaabjerg, "Use of Modal Quality Factor for Resonance Mode Analysis in VSC-Based Power Systems," under review in *IEEE Journal Emerg. Sel. Topics Power Electron.*, 2020.

Chapter 5

Impedance-Based Modeling of Large-Scale Power Electronics Based Power System

5.1 Background

In Chapter 3, the system stability was assessed by defining the relative stability at each bus in the multi-VSC power system. Then, the impact of parameters changing in the system on the damping characteristics of the resonance modes in the multi-VSC power system have been quantitatively defined in Chapter 4 using modal quality factor sensitivity analysis. Using the two-port network modeling method and the graph theory, the nodal admittance matrix of multi-VSC systems can preserve the asymmetrical control dynamics of VSCs. Thus, by applying the modal magnitude sensitivity analysis in [41], the modal frequency sensitivity analysis in [49], and the modal quality factor sensitivity analysis in Chapter 4, the influence of the system parameters on the resonance modes was thoroughly investigated.

For using the impedance models in the large-scale power electronic based power system, e.g. wind power plants (WPPs), the numbers of VSCs, transmission lines, and transformers become challenges to model the system using the two-port network modeling method due to the number of two-port networks increasing dramatically. For example, each VSC in Fig. 3.5 requires a two-port network to represent, and each frequency-dependent passive component, such as the grid impedances in Fig. 3.5 require two two-port

networks to represent. Thus, a frequency-dependent aggregated modeling method is necessary to convert the network containing a large number of two-port networks into an equivalent model to participate in system analysis. In the existing aggregated model of WPPs, the asymmetrical frequency-coupled dynamics of the VSCs are often neglected, where the impedance model of wind turbines in a single WPP (or even multiple WPPs) are characterized as a single SISO transfer function [58]. Furthermore, the operating conditions of the wind turbines in the aggregated models are assumed to be homogeneous, where the operating conditions highly depend on the wind speed and the active power and reactive power reference signals.

Therefore, this chapter aims to provide frequency-dependent aggregated model that can be adapted to the two-port networks of impedance model of VSCs. Thus, the aggregated model is validated on the Anholt 400 MW offshore WPP [71], where the aggregated model can preserve the asymmetrical control dynamics of VSCs in the 33 kV network for stability analysis and resonance mode analysis. The asymmetrical control dynamics of VSCs can further be brought into the 220 kV network for power system analysis. The validation is organized as an impedance-based modeling and analysis workflow for analyzing the large-scale power electronic based power system.

5.2 Frequency-Dependent Aggregated Model

The system shown in Fig. 3.3 has been represented as two-port network connections like shown in Fig. 4.15, which represents the small-signal model of the system. Since it focuses on investigating the resonance modes in the system, the buses v_1 and v_3 are connected to the ground node v_9 in Fig. 4.15, which indicates the system is connected to an ideal voltage source v_g in Fig. 3.3.

Yet, to derive the dynamic equivalent aggregated model seen into the ports of v_1 and v_3, Fig. 4.15 is revised and it is illustrated in Fig. 5.1, where the oriented incidence matrix, $[B_G]$ in (4.31) is replaced with another oriented incidence matrix $[A_G]$ given as

$$[A_G] = \begin{array}{c} \\ v_1 \\ v_2 \\ v_3 \\ \vdots \\ v_9 \end{array} \begin{array}{c} \begin{array}{ccccc} e_{1,1} & e_{1,2} & e_{1,1} & \cdots & \cdots \end{array} \\ \begin{bmatrix} +1 & \cdots & \cdots & \cdots & \cdots \\ \vdots & +1 & \cdots & \cdots & \vdots \\ \vdots & \vdots & +1 & \cdots & \vdots \\ \vdots & \vdots & \vdots & \ddots & \vdots \\ -1 & -1 & -1 & \cdots & \cdots \end{bmatrix} \end{array} \tag{5.1}$$

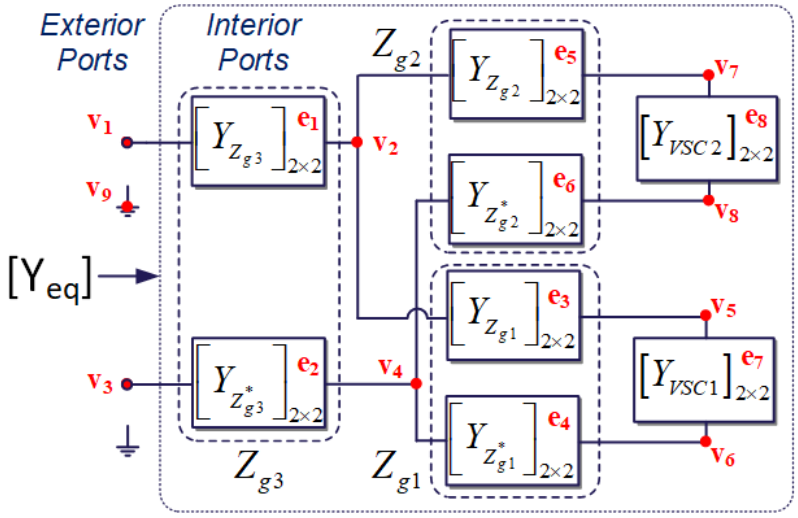

Fig. 5.1: Two-port network connections of the system shown in Fig. 3.3 for deriving the equivalent aggregated model. Source: [J5].

where the nodal admittance matrix is derived as

$$[Y] = [A_G]\,[Y_E]\,\left[A_G^T\right] \tag{5.2}$$

where the nodal admittance matrix derived in (4.30) can be simplified as a 6×6 matrix because v_1 and v_3 are zero row vectors. Thus, the nodal admittance matrix derived in (5.2) can only be simplified as an 8×8 matrix. The 8×8 matrix represents an 8-port network, where the ports can be categorized by the types of their connections, i.e.,v_1 and v_3 connect to exterior circuit called the exterior ports and the other ports are called the interior ports. The 8-port network in (5.2) is then divided into four parts given as

$$\begin{bmatrix} [i_e]_{2\times1} \\ [i_i]_{6\times1} \end{bmatrix} = \underbrace{\begin{bmatrix} [Y_{ee}]_{2\times2} & [Y_{ei}]_{2\times6} \\ [Y_{ie}]_{6\times2} & [Y_{ii}]_{6\times6} \end{bmatrix}}_{[Y]} \begin{bmatrix} [v_e]_{2\times1} \\ [v_i]_{6\times1} \end{bmatrix} \tag{5.3}$$

The electrical relationships of the equivalent circuit seen at the exterior ports can be derived letting $[i_i] = 0$ as elaborated in [J5] as

$$[i_e] = [Y_{eq}]\,[v_e] = \underbrace{\left[[Y_{ee}] - [Y_{ei}]\,[Y_{ii}]^{-1}\,[Y_{ie}]\right]}_{[Y_{eq}]}\,[v_e] \tag{5.4}$$

where $[Y_{eq}]$ is related to the entries of 4 submatrices $[Y_{ee}]$, $[Y_{ei}]$, $[Y_{ie}]$, and $[Y_{ii}]$, where the influence of these entries to the exterior port dynamics needs to be

analyzed to utilize this aggregated model in the other system. The partition transformation matrices $[T_1]$ and $[T_2]$ are given as

$$[T_1] = \begin{bmatrix} I_2 & O_{2\times 6} \end{bmatrix} \tag{5.5}$$

$$[T_2] = \begin{bmatrix} O_{6\times 2} & I_6 \end{bmatrix} \tag{5.6}$$

where $[Y_{ee}]$, $[Y_{ei}]$, $[Y_{ie}]$, and $[Y_{ii}]$ are derived as

$$\begin{aligned} [Y_{ee}]_{2\times 2} &= [T_1]\,[Y]\,[T_1]^T \quad [Y_{ei}]_{2\times 6} = [T_1]\,[Y]\,[T_2]^T \\ [Y_{ie}]_{6\times 2} &= [T_2]\,[Y]\,[T_1]^T \quad [Y_{ii}]_{6\times 6} = [T_2]\,[Y]\,[T_2]^T \end{aligned} \tag{5.7}$$

where $[Y_{ee}]$ and $[Y_{ii}]$ are square matices, $[Y_{ei}]$ and $[Y_{ie}]$ are rectangular matrices.

5.2.1 Eigenvalue and Singular Value Sensitivity Analysis

The relationships between the equivalent aggregated model $\left[Y_{eq}\right]$ and submatrices $[Y_{ee}]$, $[Y_{ei}]$, $[Y_{ie}]$, and $[Y_{ii}]$ are shown in (5.4). Yet, the admittances of VSCs are highly depend on the operating points, e.g. active power and reactive power set points. Therefore, it is necessary to quantify the influence of the admittance change in submatrices on the equivalent aggregation model in order to use the equivalent aggregation model in large-scale power electronic based power system. To quantify influence of admittance change, the sensitivity analysis in Chapter 4 can be used for the square matrices $[Y_{ee}]$ and $[Y_{ii}]$, where $\left[Y_{eq}\right]$ is related to $[Y_{ee}]$ and $[Y_{ii}]^{-1}$ in (5.4). Then, the eigenvalue decomposition of $[Y_{ii}]^{-1}$ and $[Y_{ee}]$ are given as

$$[Y_{ii}]^{-1} = \mathbf{L}_{ii}\mathbf{\Lambda}_{ii}^{-1}\mathbf{R}_{ii}^{*} \tag{5.8}$$

$$[Y_{ee}] = \mathbf{L}_{ee}\mathbf{\Lambda}_{ee}\mathbf{R}_{ee}^{*} \tag{5.9}$$

where $\mathbf{\Lambda}_{ii}^{-1}$ is the modal impedance matrix specified in Chapter 4.2. To be noticed that, $\mathbf{\Lambda}_{ii}^{-1}$ is the inverse of the eigenvalues of $[Y_{ii}]$. Since $\mathbf{\Lambda}_{ii}^{-1}$ describe the relationships between input voltage vectors and output current vectors, they are called the modal *impedances* of $[Y_{ii}]$. On the other hand, $\mathbf{\Lambda}_{ee}$ describe the relationships between input current vectors and output voltage vectors, they should be called the modal *admittances* of $[Y_{ee}]$.

Accordingly, the entries of $\left[Y_{eq}\right]$ are related to the modal impedances of $[Y_{ii}]$, but to the modal admittances of $[Y_{ee}]$, where $\left[Y_{eq}\right]$ shows singularity when $\mathbf{\Lambda}_{ii}^{-1}$ or $\mathbf{\Lambda}_{ee}$ approaches singular.

Yet, the matrices $[Y_{ei}]$ and $[Y_{ie}]$ in (5.4) are rectangular matrices, where the eigenvalue decomposition cannot be applied. Thus, the singular value

decomposition is used in [J5] to analyze the $[Y_{ei}]$ and $[Y_{ie}]$. For the $m \times n$ matrix, $\mathbf{A}$, it can be decomposed as

$$\mathbf{A}_{m\times n} = \mathbf{U}_{m\times m}\mathbf{\Sigma}_{m\times n}\mathbf{V}^*_{n\times n} \tag{5.10}$$

where the column vectors of $\mathbf{U}$ and $\mathbf{V}$ are called the left-singular vectors and right-singular vectors of $\mathbf{A}$, respectively. Thus, the $\mathbf{\Sigma}$ results into the rectangular diagonal matrix, and the diagonal k terms in $\mathbf{\Sigma}$ are called singular values, $k \leq \min\{m, n\}$. The i^{th} singular value σ_i can be derived using two supplementary matrices, $\mathbf{A}\mathbf{A}^*$ and $\mathbf{A}^*\mathbf{A}$ [J5] given as

$$\sigma_i^2(\mathbf{A}) = \lambda_i(\mathbf{A}\mathbf{A}^*) = \lambda_i(\mathbf{A}^*\mathbf{A}) \tag{5.11}$$

where the eigenvalues of $\mathbf{A}\mathbf{A}^*$ and $\mathbf{A}^*\mathbf{A}$ are non-negative real values because of $\mathbf{A}\mathbf{A}^*$ and $\mathbf{A}^*\mathbf{A}$ are Hermitian and positive semi-definite matrices. Then, σ_i is defined as the positive square root of λ_i. The influence of the network component to the dynamic equivalent aggregated model can be analyzed with (5.8) and (5.9) using the eigenvalue sensitivity index, which is derived in (4.24), where the eigenvalue sensitivity of $[Y_{ii}]$ and $[Y_{ee}]$ are given as

$$\frac{\partial \lambda_{ii,k}}{\partial \alpha} = r^*_{ii,k}\frac{\partial [Y_{ii}]}{\partial \alpha}l_{ii,k} \tag{5.12}$$

$$\frac{\partial \lambda_{ee,k}}{\partial \alpha} = r^*_{ee,k}\frac{\partial [Y_{ee}]}{\partial \alpha}l_{ee,k} \tag{5.13}$$

where α represents a network component parameter in $[Y_{ii}]$ or $[Y_{ee}]$. For the network components in $[Y_{ei}]$ or $[Y_{ie}]$, the singular value sensitivity can be similarly derived [J5] as

$$\frac{\partial \sigma_{ei,k}}{\partial \alpha} = \mathrm{Re}\left[u^*_{ei,k}\frac{\partial [Y_{ei}]}{\partial \alpha}v_{ei,k}\right] \tag{5.14}$$

$$\frac{\partial \sigma_{ie,k}}{\partial \alpha} = \mathrm{Re}\left[u^*_{ie,k}\frac{\partial [Y_{ie}]}{\partial \alpha}v_{ie,k}\right] \tag{5.15}$$

Thus, the aggregated model $\left[Y_{eq}\right]$ in (5.4) can be written as

$$\left[Y_{eq}\right] = \mathbf{L}_{ee}\mathbf{\Lambda}_{ee}\mathbf{R}^*_{ee} - \mathbf{U}_{ei}\mathbf{\Sigma}_{ei}\mathbf{V}^*_{ei}\mathbf{L}_{ii}\mathbf{\Lambda}^{-1}_{ii}\mathbf{R}^*_{ii}\mathbf{U}_{ie}\mathbf{\Sigma}_{ie}\mathbf{V}^*_{ie} \tag{5.16}$$

where the influence of the network components in the submatrices can be individually analyzed.

The modal impedances of $[Y_{ii}]$ in the system of Fig. 3.3 using the parameters in Table 3.1 with $K_{pi,2} = 250$ are plotted in Fig. 4.18, where the 1^{st} and 2^{nd} modal impedances approach singular at -7.5 Hz and 107.5 Hz. The equivalent aggregated model of the system $\left[Y_{eq}\right]$ are plotted in Fig. 5.2, where the dynamics also show the singularity at -7.5 Hz and 107.5 Hz. Then, the

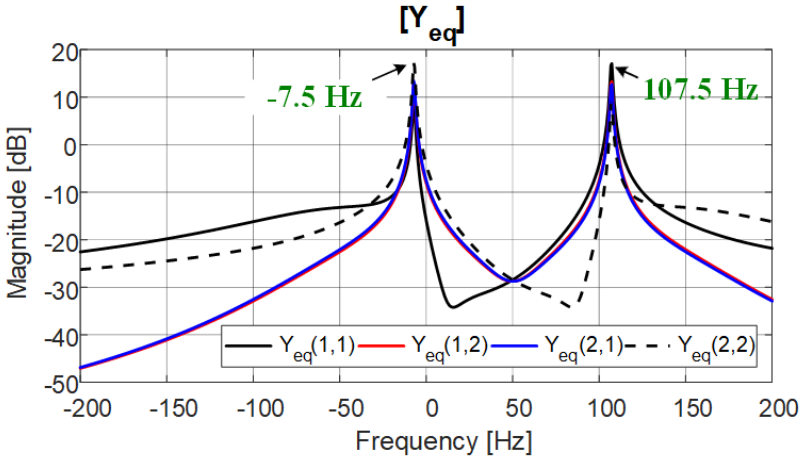

Fig. 5.2: Aggregated model of the system in Fig. 5.1, $[Y_{eq}]$, with $K_{pi,2} = 250$. Source: [J5].

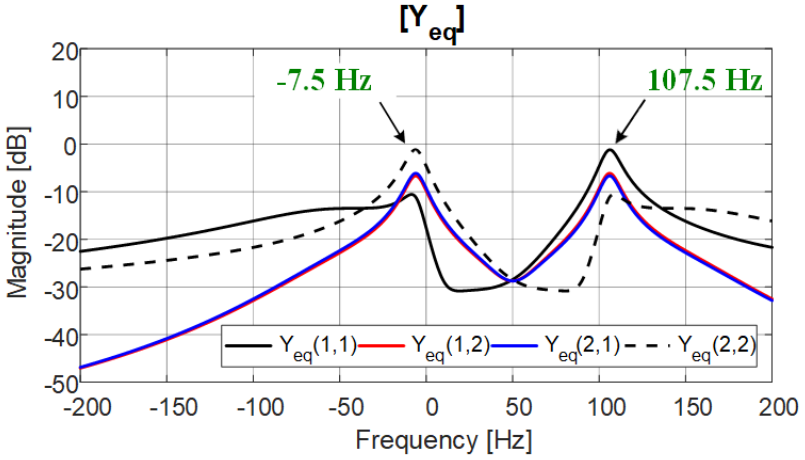

Fig. 5.3: Aggregated model of the system in Fig. 5.1, $[Y_{eq}]$, with $K_{pi,2} = 100$. Source: [J5].

equivalent aggregated model of the other case with $K_{pi,2} = 100$ are plotted in Fig. 5.3, which illustrates how the network components connected to the interior ports affect the dynamics of the equivalent aggregated model.

Remark (Eigenvalue and singular value sensitivity on the equivalent aggregated model)
Since the nodal admittance matrix in (5.2) can be partitioned as shown in (5.3), the shunt components, y_{sh}, can affect only one of the submatrices in (5.3). Then, the influence of y_{sh} can be analyzed with the corresponding matrices in (5.16) assuming the other matrices are fixed. For example, when y_{sh} connected at the interior ports $[v_i]$ changes, the submatrices, $[Y_{ee}]$, $[Y_{ei}]$, and $[Y_{ie}]$ are unaffected. However, for the series components y_{se} connected between the buses, especially connected between the interior ports $[v_i]$ and the exterior ports $[v_e]$, all 4 submatrices are affected.

5.3 Case Study with Anholt Offshore WPP

The system discussed in previous Chapters contains only two VSCs, which can hardly represent large-scale power electronic based power system. To show the effectiveness of the aggregated model, the Anholt offshore WPP is used as an example, where the physical layout of the Anholt offshore WPP is shown in Fig. 5.4.

In the Anholt offshore WPP, there are 111, Siemens SWT-3.6-120, 3.6 MW type 4 wind turbines, where the WPP is located in Kattegat with distance from shore of 21 km [71]. The 33 kV medium voltage transmission line cable network is given in Fig. 5.4, and the wind turbines are shown as the green dots. The wind turbines can be sorted into 12 wind turbine strings and they are connected to three 140 MV A, 220 kV/33 kV collector park transformers at the offshore substation [45, 72]. The copper cables used in the 33 kV transmission network can be categorized with three different cross-sections, namely 150 mm^2, 240 mm^2, and 500 mm^2, which are shown in different colors in Fig. 5.4. From the offshore substation, the WPP is connected to the shore with 24.5 km, three-core 1600 mm^2 aluminum submarine cable. Then, it is connected to 400 kV/220 kV transformer at the onshore substation with 58 km, three single-core 2000 mm^2 aluminum land cables [45], where the transformers in the analysis are with leakage impedance of 0.1 pu with the X/R ratio is equal to 10 [72].

The PCC #1 highlighted in Fig. 5.4 is chosen to apply the analysis with the aggregated model. Thus, the 220 kV/33 kV transformer, submarine cables, land cables, and 400 kV/220 kV transformer are considered as the grid impedance. In the 33 kV transmission network, the distances between the turbines are about 600 meters at the edges and about 900-1300 meters inside

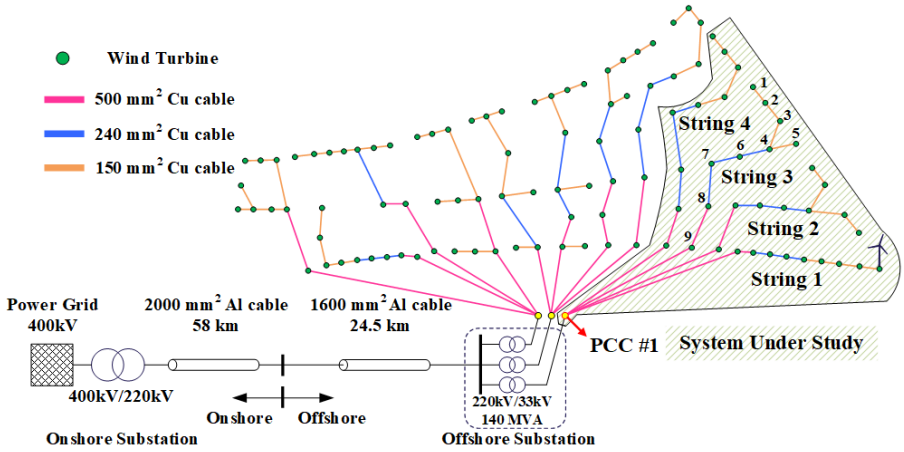

Fig. 5.4: Physical layout of the Anholt 400 MW offshore WPP with the cable connection from wind turbines to the onshore substation [71]. The system under study is highlighted. Source: [J6].

Table 5.1: Transmission line parameters in the wind farm [73]. Source: [J6].

Cross Section	Voltage rating	Material	Inductance (L_t)	Capacitance (C_t)	Resistance (R_t)
150 mm^2	35 kV	Copper	404 µH/km	0.181 µF/km	0.124 Ω/km
240 mm^2	35 kV	Copper	372 µH/km	0.214 µF/km	0.075 Ω/km
500 mm^2	35 kV	Copper	325 µH/km	0.277 µF/km	0.037 Ω/km
1600 mm^2	220 kV	Aluminum	240 µH/km	0.152 µF/km	0.019 Ω/km
2000 mm^2	220 kV	Aluminum	230 µH/km	0.139 µF/km	0.015 Ω/km

the wind farm, but the distances between turbines may not represent the cable length used in the network, where the total length of cable is around 160 km [71]. Furthermore, due to the limited cable information of transmission line, the passive component parameters of the 33 kV copper transmission cables and 220 kV aluminum transmission cables are listed in Table 5.1 [73] for the analysis, which are assumed to be similar to the practical cables used in the WPP.

The wind turbine symbol shown at the end of wind turbine String 1 in Fig. 5.4 is further illustrated in Fig. 5.5 [45], where the grid side VSC connecting to a 4 MV A, 33 kV/690 V step-up wind turbine (WT) transformers to the 33 kV network. To include the asymmetrical dynamics of VSCs while keeping the impedance model of the VSC simple, only the basic ac current control loop using PI controller (CC(PI)) for regulating the output current in the dq-frame and the phase-locked loop (PLL) for grid synchronization are considered. Thus, it is assumed that the dc link capacitor, C_{dc}, is large enough to ignore the dynamics of the dc link, where the input power, P_{in}, delivering to C_{dc} becomes an ideal dc source, v_{dc}. The ac side of the VSCs connect to

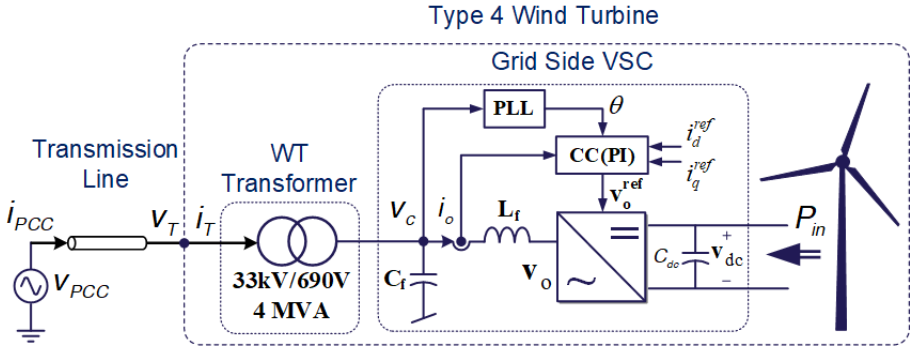

Fig. 5.5: System configuration of the wind turbine with 33 kV/690 V WT transformer including the basic control block diagram of grid side VSC. Source: [J6]. CC(PI): Ac current control with PI controller in the dq-frame.

the WT transformer with the three-phase LC filter, L_f and C_f, where the filter capacitor voltage, v_c, and the filter inductor current, i_o, are measured as the inputs for CC and PLL. Then, the current commands are given in the dq-frame, i_d^{ref} and i_q^{ref} as the input of CC(PI). The PI controllers are also used in the PLL for grid synchronization [74]. The system parameters and the control parameters are listed in Table 5.2.

Thus, the two-port network modeling method specified in Chapter 2.2 can be used, where the grid side VSC in Fig. 5.5 is represented as a two-port network in the $\alpha\beta$-frame characterized with the voltage vectors, v_c and $e^{j2\theta}v_c^*$ and current vectors, i_o and $e^{j2\theta}i_o^*$ as shown in Fig. 5.6. The electrical relationships are given as

$$\begin{bmatrix} i_o \\ e^{j2\theta}i_o^* \end{bmatrix} = [Y_{VSC}]_{2\times 2} \begin{bmatrix} v_c \\ e^{j2\theta}v_c^* \end{bmatrix} \tag{5.17}$$

Furthermore, the filter capacitor C_f and the WT transformer in Fig. 5.5 can also be modeled as the two-port network as shown in Fig. 5.7 characterized with the voltage vectors, v_c and v_T and current vectors, i_o and i_T with the electrical relationships given as

$$\begin{bmatrix} v_T \\ i_T \end{bmatrix} = \underbrace{\begin{bmatrix} 1 & Z_L(s) \\ 0 & 1 \end{bmatrix}}_{\mathbf{Z}_{Z_L}} \begin{bmatrix} \frac{1}{n} & 0 \\ 0 & n \end{bmatrix} \underbrace{\begin{bmatrix} 1 & 0 \\ sC_f & 1 \end{bmatrix}}_{\mathbf{Y}_{C_f}} \begin{bmatrix} v_c \\ -i_o \end{bmatrix} \tag{5.18}$$

where (5.18) is the two-port network with ABCD-parameters that can be transformed into the Y-parameter representation introduced in Chapter 2.4. $Z_L(s) = sL_L + R_L$, L_L and R_L are the leakage inductance and leakage resistance of the WT transformer, respectively. To connect to the other voltage

Table 5.2: Control and System Parameters. Source: [J6].

Symbol	Description	Value
v_{pcc}	Nominal grid voltage (line-line, rms)	33 kV
P_{in}	Nominal power	3.6 MW
ω_1	Rated frequency	314.16 rad/s (50 Hz)
f_s	Sampling frequency	2 kHz
L_f	Converter-side filter inductor	50 µH
C_f	Filter capacitor	1 mF
$i_{d,ref}$	d-axis current command	4.26 kA
$i_{q,ref}$	q-axis current command	0.95 kA
K_{pc}	Current controller K_p	0.0785 Ω
K_{ic}	Current controller K_i	8.2247 Ω/s
	Current control bandwidth	5 pu (250 Hz)
$K_{p,PLL}$	PLL controller K_p	0.2788 rad/(V s)
$K_{i,PLL}$	PLL controller K_i	2.9197 rad/(V s^2)
	Phase-locked loop bandwidth	0.5 pu (25 Hz)
X/R	X/R ratio of WT transformer	10
Z_L	Leakage impedance of WT transformer	0.1 pu

and current vectors of Fig. 5.6, $e^{j2\theta}v_c^*$ and $e^{j2\theta}i_o^*$, the complex conjugate and frequency shifted matrix of (5.18) can be derived [J6] as

$$\begin{bmatrix} e^{j2\theta}v_T^* \\ e^{j2\theta}i_T^* \end{bmatrix} = \begin{bmatrix} 1 & (s-j2\omega_1)L_L + R_L \\ 0 & 1 \end{bmatrix} \begin{bmatrix} \frac{1}{n} & 0 \\ 0 & n \end{bmatrix} \begin{bmatrix} 1 & 0 \\ (s-j2\omega_1)C_f & 1 \end{bmatrix} \begin{bmatrix} e^{j2\theta}v_c^* \\ -e^{j2\theta}i_o^* \end{bmatrix} \tag{5.19}$$

Before bringing the asymmetrical dynamics of VSCs to the 33 kV network, the stability of three cascaded two-port networks, (5.18), (5.17), and (5.19), have to be ensured. Since the WT transformer models, (5.18) and (5.19) contain only passive components, the admittance-ratio stability analysis method specified in Chapter 2.3 can be applied. Then, the asymmetrical dynamics of VSCs can be brought to the 33 kV network by cascading (5.18), (5.17), and (5.19).

For the wind turbine at the end of String 1 in Fig. 5.4, to connect to PCC #1, the transmission line contains 9 sections of transmission cables with different lengths and different cross sections, where other wind turbines are connected to intermediate nodes. Similar to Fig. 5.7, the transmission cables can be modeled with π-model as shown in Fig. 5.8 [22], where the electrical

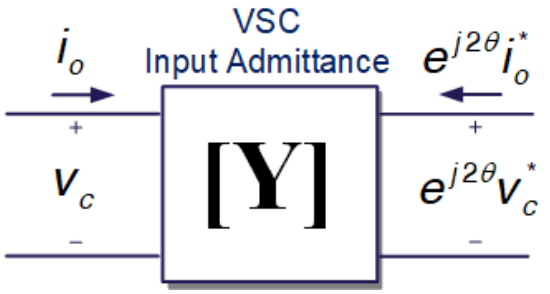

Fig. 5.6: Admittance form of the two-port network representation of grid side VSC. Source: [J6].

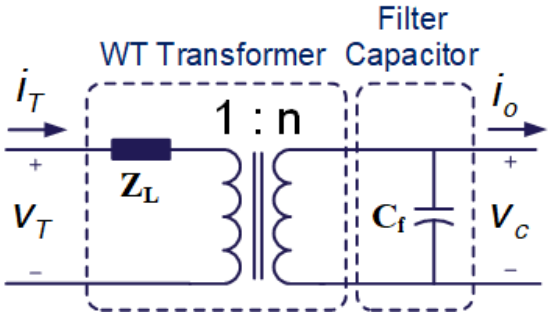

Fig. 5.7: Two-port network representation of the WT transformer and the filter capacitor C_f. Source: [J6].

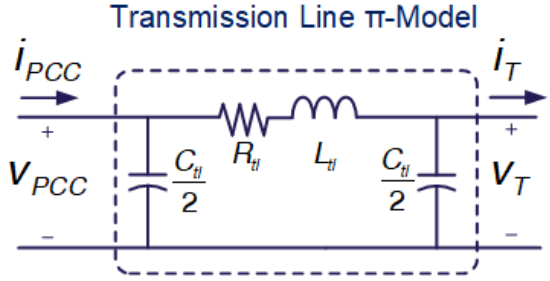

Fig. 5.8: Two-port network representation of the π-model of the transmission line. Source: [J6].

relationships are given as

$$\begin{bmatrix} v_{PCC} \\ i_{PCC} \end{bmatrix} = \begin{bmatrix} 1 & 0 \\ \frac{sC_{tl}}{2} & 1 \end{bmatrix} \begin{bmatrix} 1 & sL_{tl}+R_{tl} \\ 0 & 1 \end{bmatrix} \begin{bmatrix} 1 & 0 \\ \frac{sC_{tl}}{2} & 1 \end{bmatrix} \begin{bmatrix} v_T \\ -i_T \end{bmatrix} \quad (5.20)$$

where the complex conjugate and frequency shifted matrix of (5.20) can be derived as

$$\begin{bmatrix} e^{j2\theta}v^*_{PCC} \\ e^{j2\theta}i^*_{PCC} \end{bmatrix} = \begin{bmatrix} 1 & 0 \\ \frac{(s-j2\omega_1)C_{tl}}{2} & 1 \end{bmatrix} \begin{bmatrix} 1 & (s-j2\omega_1)L_{tl}+R_{tl} \\ 0 & 1 \end{bmatrix} \begin{bmatrix} 1 & 0 \\ \frac{(s-j2\omega_1)C_{tl}}{2} & 1 \end{bmatrix} \begin{bmatrix} e^{j2\theta}v^*_T \\ -e^{j2\theta}i^*_T \end{bmatrix} \quad (5.21)$$

Since the two-port network representations of the components in the wind turbine strings are derived with (5.17) to (5.21), String 3 in Fig. 5.4 with two branches is used to derive the equivalent aggregated model at PCC #1 because the structure of String 1 in Fig. 5.4 is relatively simple with only a single branch. The two-port networks connection of the wind turbine String 3 in Fig. 5.4 is shown in Fig. 5.9, where WT1 to WT9 are the wind turbine models at the 33 kV network. It is worth mentioning that String 3 contains multiple wind turbines, which makes String 3 to become a multi-VSC system. Thus, the stability analysis at 33 kV requires to use the reflection coefficient stability criterion as specified in Chapter 3.3.

Thus, the nodal admittance matrix of String 3 can be derived as

$$[Y_{Str3}] = \mathbf{A}_{G,Str3}\mathbf{Y}_{E,Str3}\mathbf{A}^T_{G,Str3} \quad (5.22)$$

where $\mathbf{A}_{G,Str3}$ is the oriented incidence matrix of String 3 and $\mathbf{Y}_{E,Str3}$ is the elementary matrix of String 3. The damping characteristic of the resonance modes in wind turbine String 3 can be analyzed with the modal quality factor sensitivity analysis method described in Chapter 4.3. The dimensions of $[Y_{Str3}]$, $\mathbf{A}_{G,Str3}$, and $\mathbf{Y}_{E,Str3}$ are illustrated in Fig. 5.10, where $[Y_{Str3}]$ is a 20×20 matrix representing a twenty-port network.

The 20×20 complex matrix requires 400 entries of complex numbers to describe a single frequency point, where the data increases dramatically when analyzing the system in a wide frequency range [J6]. For analyzing the system depicted in Fig. 5.4, the nodal admittance matrix becomes a 74×74 complex matrix, which makes the analysis rather difficult. Thus, equation (5.4) is used by defining the 18 nodes inside the block of Fig. 5.9 which are the interior ports of the network. The matrix $[Y_{Str3}]$ is then divided into 4 submatrices as

$$[Y_{Str3}]_{20\times20} = \begin{bmatrix} [Y_{ee,Str3}]_{2\times2} & [Y_{ei,Str3}]_{2\times18} \\ [Y_{ie,Str3}]_{18\times2} & [Y_{ii,Str3}]_{18\times18} \end{bmatrix} \quad (5.23)$$

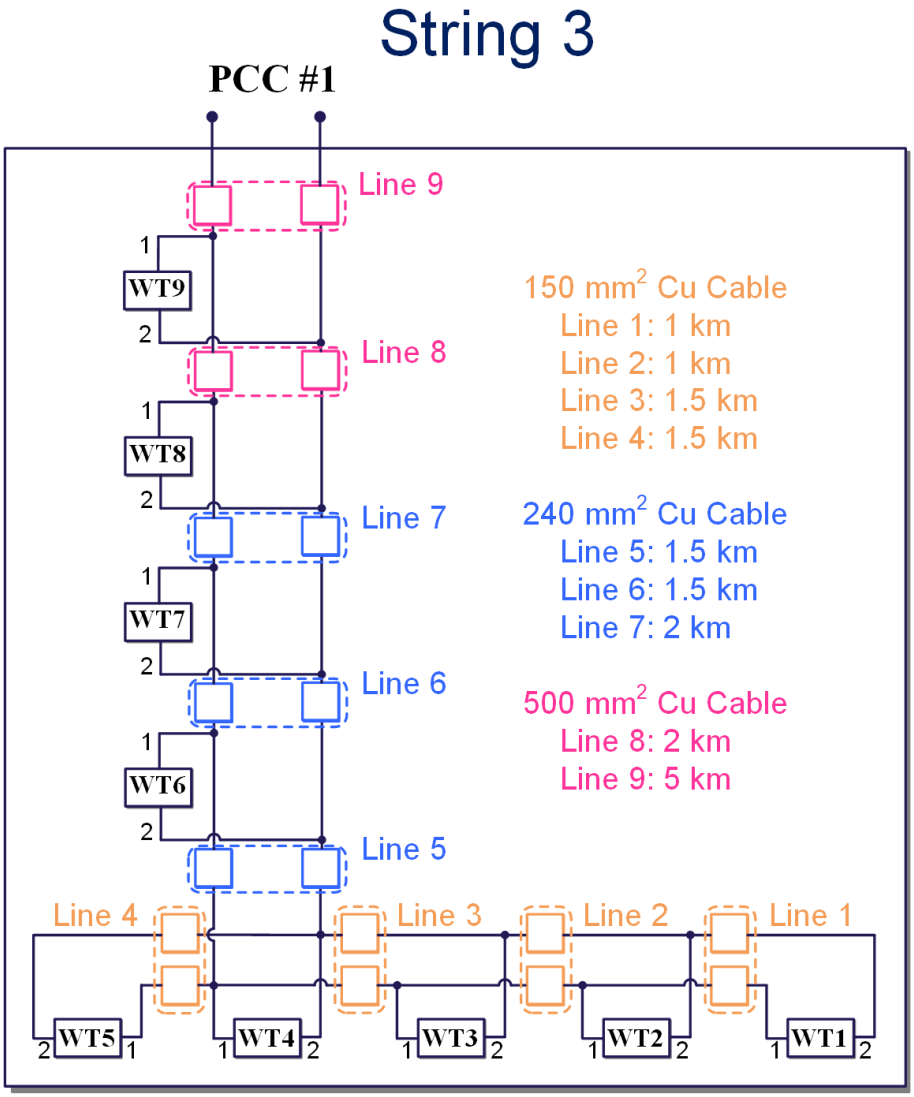

Fig. 5.9: Two-port networks connection of wind turbine String 3 shown in Fig. 5.4. Source: [J6].

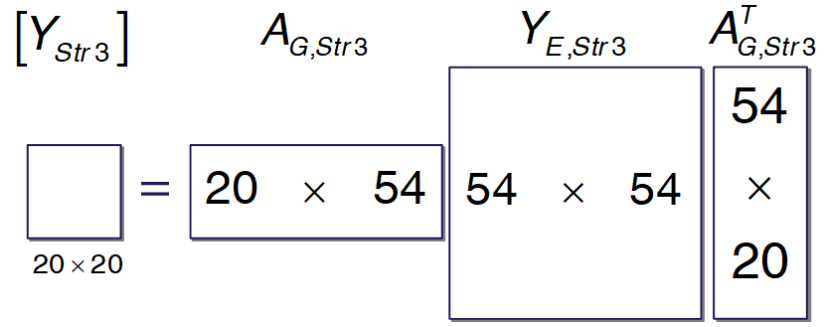

Fig. 5.10: Illustration of the nodal admittance matrix in (5.22). Source: [J6].

Table 5.3: Cable Lengths of the components in Fig. 5.4. Source: [J6].

	150 mm^2 Section 1	150 mm^2 Section 2	150 mm^2 Section 3	150 mm^2 Section 4	240 mm^2 Section 1	240 mm^2 Section 2	240 mm^2 Section 3	500 mm^2 Section 1	500 mm^2 Section 2
String 1	1 km	1 km	1 km	1 km	1 km	1 km	1 km	1 km	7.5 km
String 2	1 km	1.5 km	1.5 km	1 km	1 km	1 km	1 km	2 km	6.5 km
String 3	1 km	1 km	1.5 km	1.5 km	1.5 km	1.5 km	2 km	2 km	5 km
String 4	1 km	1 km	2 km	1.5 km	1.5 km	2.5 km	2 km	2 km	5 km

where the equivalent aggregated model of the wind turbine String 3,$\mathbf{Y}_{eq,Str3}$, is then derived as

$$\mathbf{Y}_{eq,Str3} = [Y_{ee,Str3}] - [Y_{ei,Str3}]\,[Y_{ii,Str3}]^{-1}\,[Y_{ie,Str3}] \tag{5.24}$$

where $\mathbf{Y}_{eq,Str3}$ results into a 2×2 matrix, and the entries of $\mathbf{Y}_{eq,Str3}$ are plotted in Fig. 5.11 with the parameters listed in Table 5.1 and Table 5.2. Here the cable lengths in String 3 are given in Fig. 5.9 and the asymmetrical dynamics of VSCs are preserved.

Then, the equivalent aggregated models of wind turbine String 1, wind turbine String 2, and wind turbine String 4 can be derived following the same process from (5.22) to (5.24). Since the transmission lines are modeled to derive the aggregated model, the cable lengths used in wind turbine String 1, wind turbine String 2, wind turbine String 3, and wind turbine String 4 are as listed in Table 5.3.

The $(1,1)$ entry of the aggregated models of wind turbine String 1, wind turbine String 2, wind turbine String 3, and wind turbine String 4 are plotted in Fig. 5.12 considering the same wind turbine models but different cable lengths of the transmission lines. Yet, the difference can hardly be noticed in the log plot in Fig. 5.12. Thus, the plots in Fig. 5.12 are normalized with the average value of the $(1,1)$ entries of of the aggregated models of wind turbine String 1, wind turbine String 2, wind turbine String 3, and wind

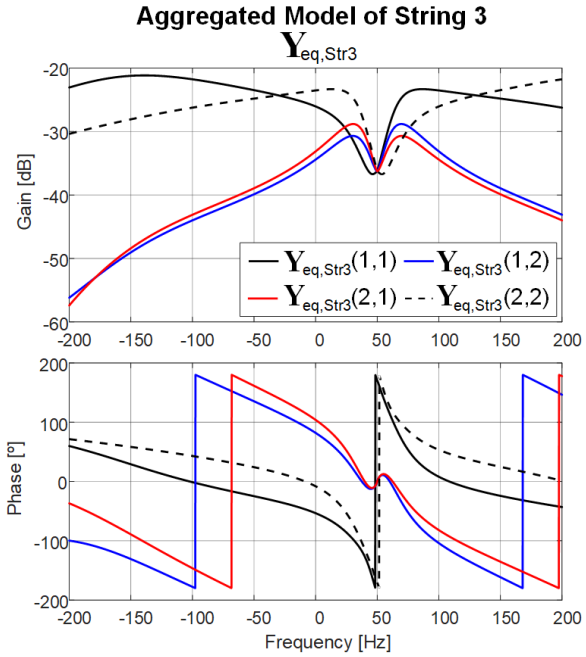

Fig. 5.11: Entries of wind turbine String 3 aggregated model, $\mathbf{Y}_{eq,Str3}$, in Fig. 5.9. Source: [J6].

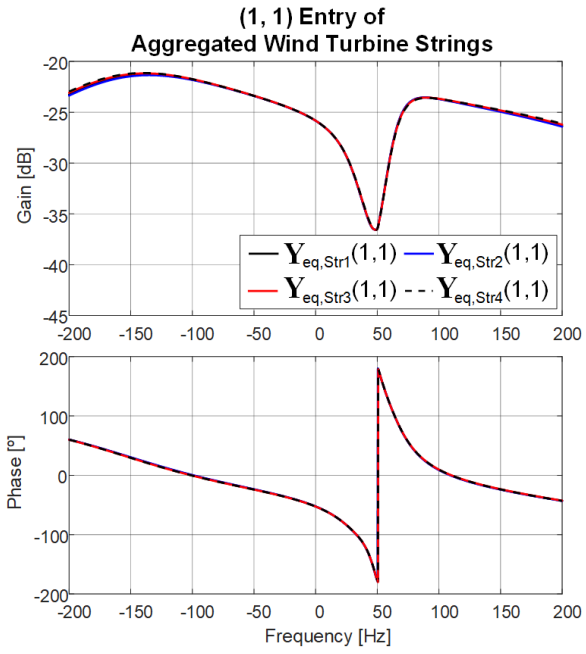

Fig. 5.12: The $(1,1)$ entry of the aggregated models of wind turbine String 1, wind turbine String 2, wind turbine String 3, and wind turbine String 4 in Fig. 5.9. Source: [J6].

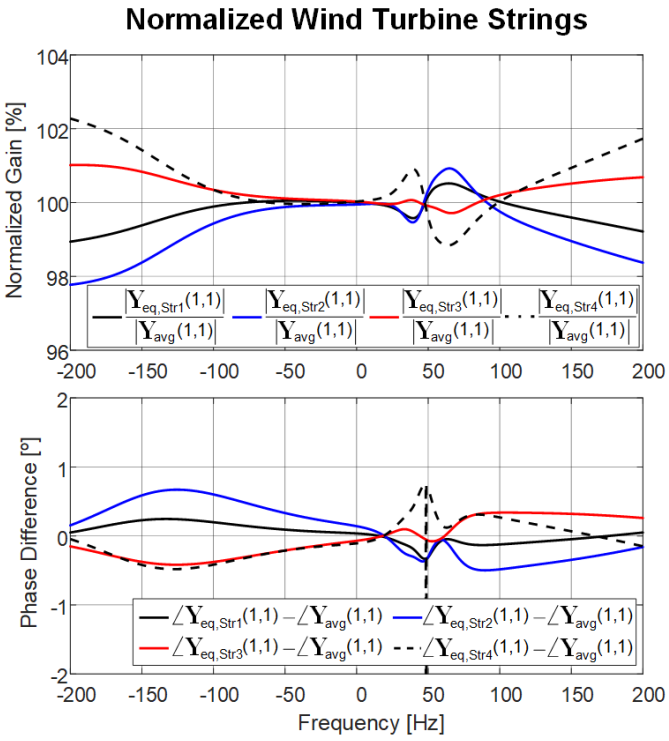

Fig. 5.13: Normalized admittance of the $(1,1)$ entry in the aggregated wind turbine strings models shown in Fig. 5.12. Source: [J6].

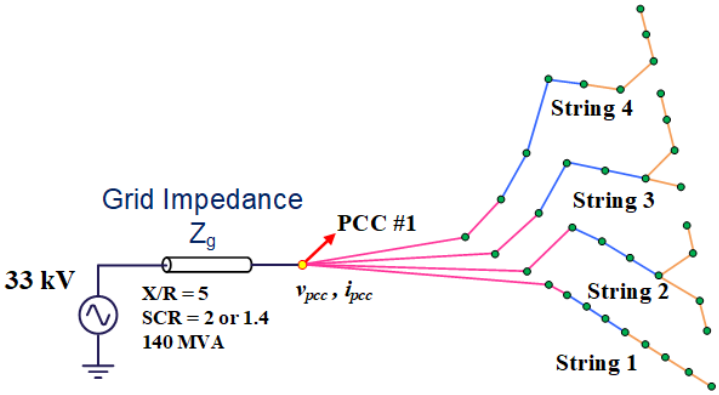

Fig. 5.14: System configuration of the studied system in Fig. 5.4 used in the simulation. Source: [J6].

turbine String 4, Y_{avg}, given as

$$\mathbf{Y}_{avg} = \frac{\mathbf{Y}_{eq,Str1}}{4} + \frac{\mathbf{Y}_{eq,Str2}}{4} + \frac{\mathbf{Y}_{eq,Str3}}{4} + \frac{\mathbf{Y}_{eq,Str4}}{4} \tag{5.25}$$

where the normalized results are plotted in Fig. 5.13, and the magnitude differences are more than $\pm$ 2% in some frequency ranges with the phase differences are around $\pm$ 0.5°, which are not negligible. Even though the wind turbine String 1 and wind turbine String 4 have the same structure of cable connection, they still show a difference in the aggregated models.

In view of the system capacity and the number of wind turbines of the whole WPP, the model validation is conducted with the simulation of the studied system in Fig. 5.4 using PLECS, where the system parameters can be found in Table 5.1 and Table 5.2, and the cable lengths can be found in Table 5.3 [J6].

The studied system given in Fig. 5.4 is simulated with a simplified configuration as shown in Fig. 5.14, where the other groups of wind turbines Fig. 5.4 are not considered. In the simulation, the average models of VSCs are used instead of the switching models of VSCs to reduce the simulation time. The sampling frequency is 2 kHz, and the current control bandwidth and the bandwidth of PLL are set to 5 pu (250 Hz) and 0.5 pu (25 Hz), respectively. The d-axis current command of each wind turbine is equal to 4.26 kA to reach the rated power of 3.6 MW. Two cases of grid impedance Z_g with the different short circuit ratios (SCR), $SCR = 1.4$ and $SCR = 2$ are tested but the same X/R ratio of 5 is used. To support the voltage of PCC #1 at 33 kV, the q-axis current command of each wind turbine is set to 0.95 kA. Thus, the power rating of the system is 140 MV A at the 33 kV network. The values of L_g and R_g at $SCR = 1.4$ or 2 composing the Z_g are given as

$$\begin{aligned} SCR = 1.4: &\qquad L_g = 17.7 \text{ mH}, R_g = 1.07\ \Omega \\ SCR = 2: &\qquad L_g = 12.4 \text{ mH}, R_g = 0.8\ \Omega \end{aligned} \tag{5.26}$$

The voltage and current time-domain waveforms at PCC #1, v_{PCC} and i_{PCC} of the case with $SCR = 2$ are shown in Fig. 5.15, where the system is stable. On the other hand, the v_{PCC} and i_{PCC} of the case with $SCR = 1.4$ are shown in Fig. 5.16, where the system is unstable with resonance observed. Since the wind turbine Strings 1 to 4 are modeled as two-port networks and they are parallel connected at PCC #1, the equivalent admittance matrix can be derived with the entrywise addition of the four equivalent admittance matrices, which is 4 times of $\mathbf{Y}_{avg}$ in (5.25). Thus, the return-ratio of the system at PCC #1, $\mathbf{G}_m$ can be calculated [J6] as

$$\mathbf{G}_m = 4\mathbf{Y}_{avg} \begin{bmatrix} sL_g + R_g & 0 \\ 0 & (s - j2\omega_1) L_g + R_g \end{bmatrix} \tag{5.27}$$

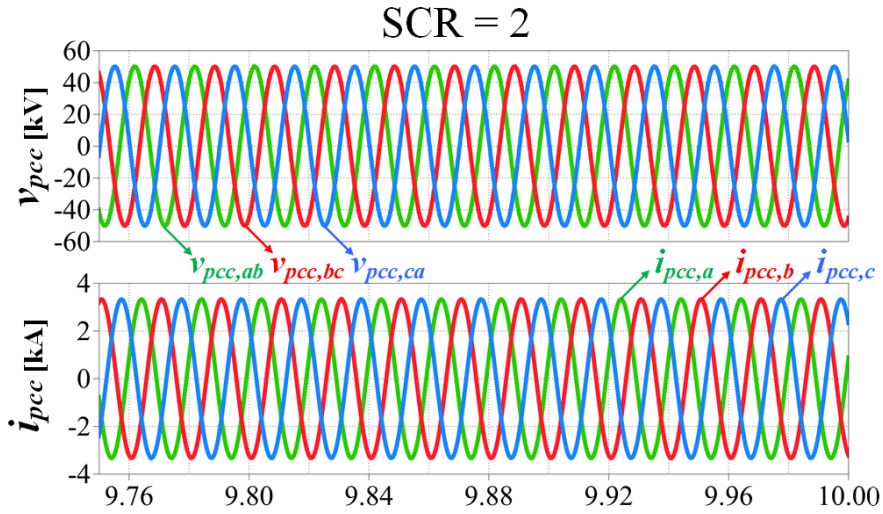

Fig. 5.15: Voltage and current waveforms of the time-domain simulation with the system configuration in Fig. 5.14, where $SCR = 2$ (X-axis: 40 ms/div, Y-axis: $i_{pcc,a}$, $i_{pcc,b}$, $i_{pcc,c}$: 2 kA/div, $v_{pcc,ab}$, $v_{pcc,bc}$, $v_{pcc,ca}$: 20 kV/div). Source: [J6].

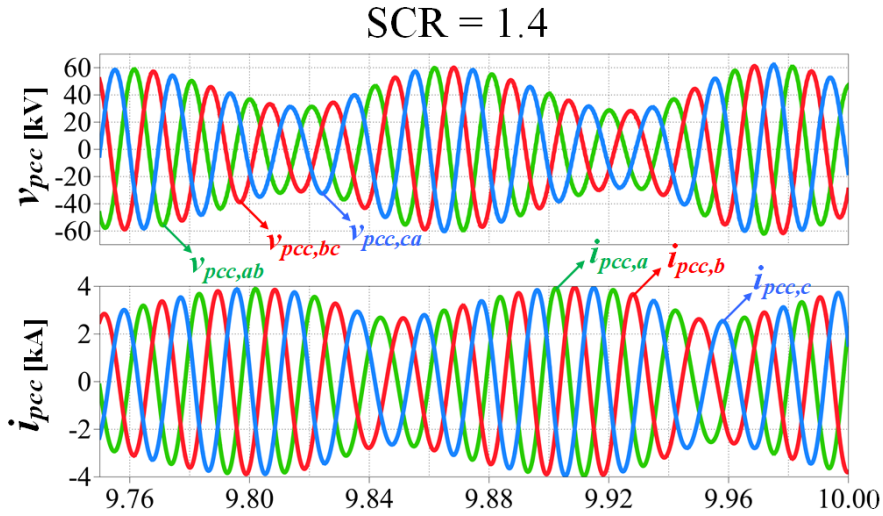

Fig. 5.16: Voltage and current waveforms of the time-domain simulation with the system configuration in Fig. 5.14, where $SCR = 1.4$ (X-axis: 40 ms/div, Y-axis: $i_{pcc,a}$, $i_{pcc,b}$, $i_{pcc,c}$: 2 kA/div, $v_{pcc,ab}$, $v_{pcc,bc}$, $v_{pcc,ca}$: 20 kV/div). Source: [J6].

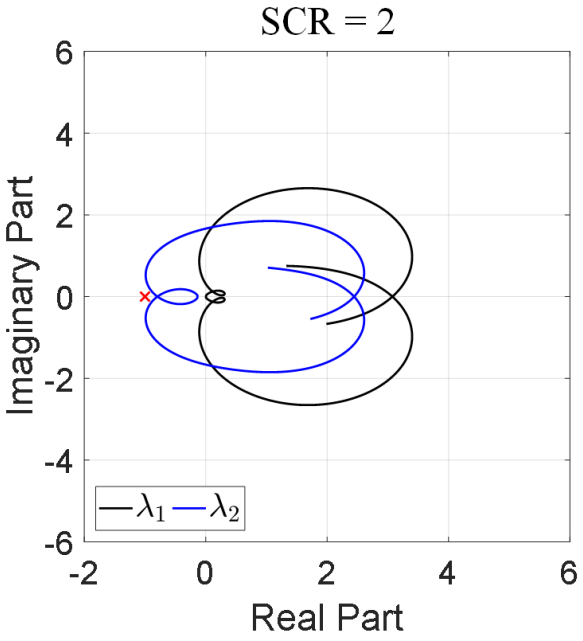

Fig. 5.17: Eigenvalues of the return ratio matrix $\mathbf{G}_m$ of the case $SCR = 2$ for the system shown in Fig. 5.14. Source: [J6].

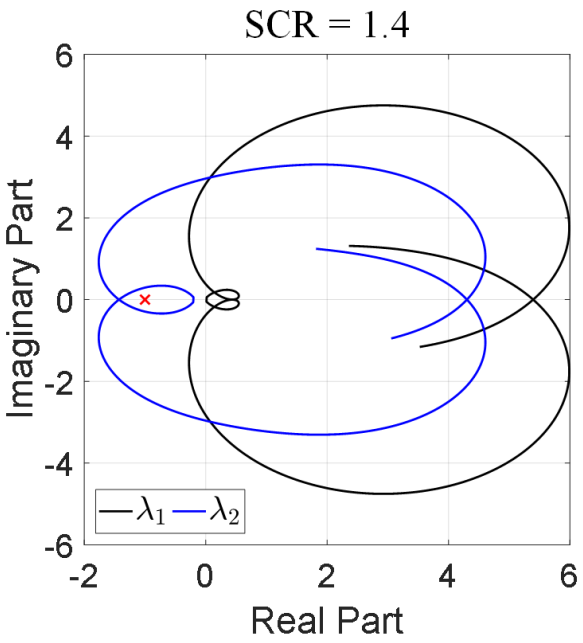

Fig. 5.18: Eigenvalues of the return ratio matrix $\mathbf{G}_m$ of the case $SCR = 1.4$ for the system shown in Fig. 5.14. Source: [J6].

Thus, the eigenvalues of $\mathbf{G}_m$ are plotted in Fig. 5.17 and Fig. 5.18. The encirclement in the case of $SCR = 1.4$ show that the system is unstable, which the eigenvalues of $\mathbf{G}_m$ have no encirclement in the case with $SCR = 2$.

5.4 Impedance-Based Modeling and Analysis Process Workflow

The aggregated models of the wind turbine strings are validated in the Anholt offshore WPP, where the workflow can be summarized as illustrated in Fig. 5.19. The process starts with the modeling of the wind turbine at the 690 V low voltage network as shown in Fig. 5.5, where the admittance-ratio stability analysis method can be used to analyze the interaction between the wind turbine and WT transformer by connecting the primary side of the transformer to an ideal power grid [J1]. If the low voltage network is stable, the wind turbine and WT transformer can be considered as an an internally stable system, whose instability can only be caused by the interaction with external power network. [62]. Yet, if the low voltage network is unstable, the resonance mode analysis in [J4] can be used to investigate the sensitivity of the control parameters change in wind turbine on the resonance mode, where corresponding parameters change can be made to enhance the damping. To be noticed that the resonance mode analysis only indicates that the system approaches singularity at certain frequency point, where the stability analysis in [J1] is necessary to apply again when the system parameters are changed to guarantee the stability of system.

The asymmetric dynamics of wind turbine have been preserved at the 33 kV medium voltage network in Fig. 5.9 by using the two-port network modeling method [J1]. However, the 33 kV medium voltage network contains not only the transmission line cables and the 220 kV/33 kV park transformer, but also other admittances of wind turbines. The reflection coefficient stability criterion can then be used to analyze the system stability and provide the stability margin indices [J2]. If the system is unstable, the resonance mode analysis in [J4] can be used again to investigate the influence of the system parameters change on the resonance mode, where the stability analysis in [J2] is necessary to apply again when system parameters are changed. For stable system, the nodal admittance matrix of the system can be derived using the graph theory in [C4] and the two-port network modeling method in [J1].

After ensuring the stability, the system can be seen as an internally stable system and then be aggregated with the aggregated model specified in [J5], which keeps the terminal behaviors and reduces the dimensions of the networks. The aggregated model can then be used in the frequency-domain stability analysis in the large-scale power electronic based power system, i.e. the

system in Fig. 5.14. The process can be repeated until the aggregated model is derived at the target network, e.g. the 33 kV medium voltage network in Fig. 5.14 can be aggregated with other wind turbine subgroups depicted in Fig. 5.4, and the system can be analyzed further in the 220 kV high voltage network, where the asymmetrical dynamics of VSCs are preserved within the process proposed.

To be noticed that when a system is aggregated, the dimensions of networks have been reduced to show only the terminal behaviors, e.g. the 20×20 admittance matrix of wind turbine String 3 was reduced to a 2×2 admittance matrix in Chapter 5.3, where the aggregation process is noninvertible. Even though the influence of system parameters change on the terminal behaviors can be revealed using the eigenvalue analysis and singular value analysis, the information of the corresponding sensitivity matrices has also been concealed during the aggregation process. To effectively utilize the aggregated model, the worst scenario of system operation should be identified, which the topic is not addressed here.

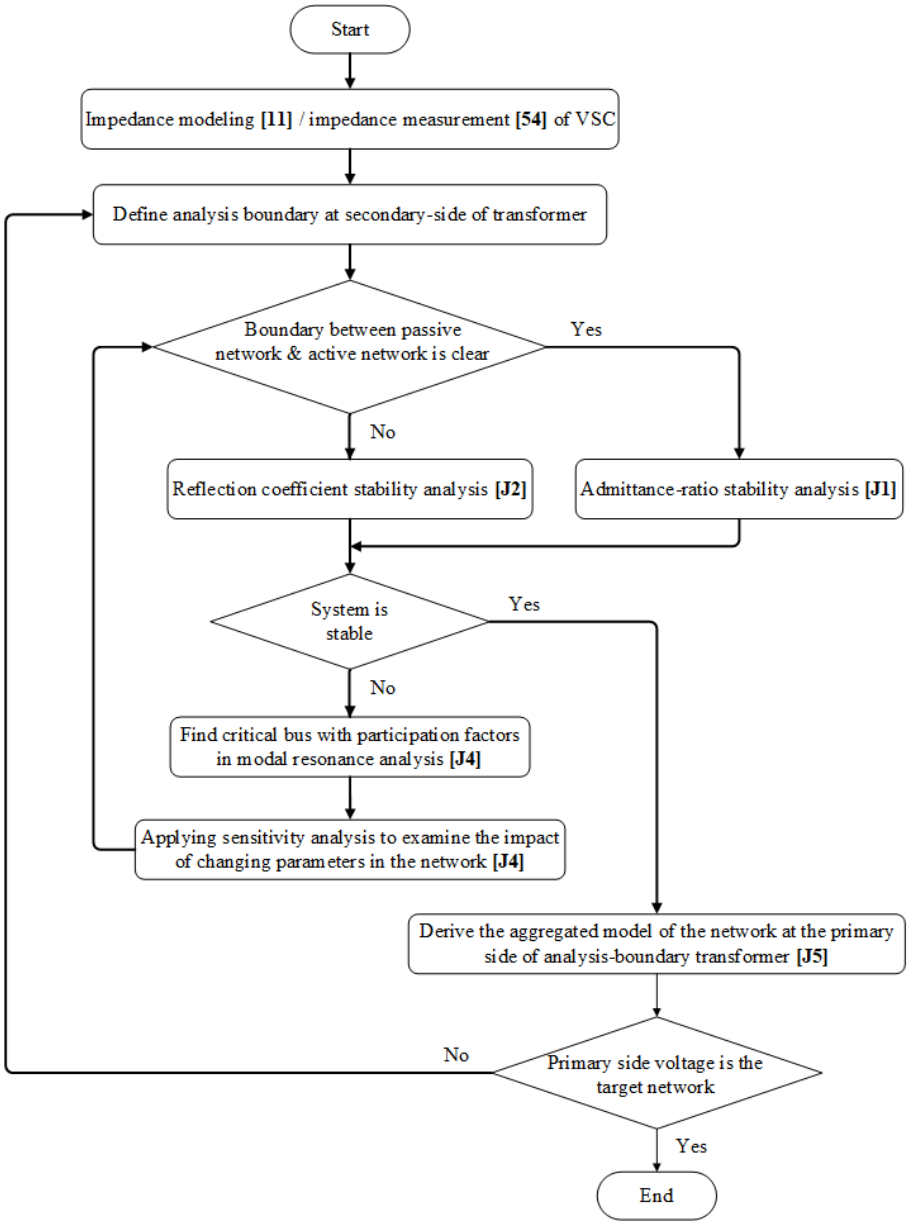

Fig. 5.19: Work flowchart of the impedance-based modeling and analysis process for large scale power electronic based power system. Source: [J6].

5.5 Summary

In this chapter, the frequency-dependent aggregated model based on the two-port network modeling method is introduced, where asymmetrical control dynamics of the VSCs can be preserved in the analysis of large-scale power electronic based power system. The aggregated model is applied in the Anholt offshore wind power plant considering the wind turbines, transmission line cables, and wind turbine transformers, where the stability analysis is conducted at 33 kV medium voltage network to show its effectiveness. A impedance-based modeling and analysis process workflow is summarized according to the key contributions in the previous chapters.

Related Publications

[C5] **S.-F. Chou**, X. Wang, and F. Blaabjerg, "An Aggregated Model for Power Electronic System Based on Multi-Port Network Reduction Method," *2020 IEEE 21st Workshop on Control and Modeling for Power Electronics (COMPEL)*, Aalborg, Denmark, 2020, pp. 1-6.

[J5] **S.-F. Chou**, X. Wang, and F. Blaabjerg, "Frequency-Dependent Aggregated Model for Power Electronic System," under review in *IEEE Trans. Power Electrons.*, 2021.

[J6] **S.-F. Chou**, X. Wang, and F. Blaabjerg, "Impedance-Based Modeling and Analysis Process for VSC Dominant Power System," under review in *IEEE Journal Emerg. Sel. Topics Power Electron.*, 2021.

Chapter 6

Conclusion

This chapter summarizes the main results and research outcomes of the Ph.D. project, where the main contributions are highlighted. Finally, some future research perspectives are discussed.

6.1 Summary

This Ph.D. project aims to efficiently analyze the harmonic stability of large-scale power electronic power systems, since modern power systems have become power electronic-dominant with a high penetration level of power-electronic-interfaced renewable energy resources, like wind and solar photovoltaic power generations. In these power-electronic-interfaced renewable energy resources, the voltage source converters (VSCs) are widely used as grid-interfaced converters. Furthermore, renewable energy power plants are designed to have a large number of power generation devices with small power capacity, which makes the large scale renewable energy power plants to become VSC dominant power systems. When multiple VSCs are closely connected, interactions may occur, leading to instability and failure. In order to solve these problems, it is necessary to understand the dynamic behavior of large-scale power electronic based power systems, which is the main goal of this PhD project. A summary of each chapter in the thesis is given in the following:

In Chapter 1, the research gaps in modeling and stability analysis of the large-scale power electronic based power system have been summarized. These gaps guide the motivation and research tasks for this Ph.D. project. The gaps also raised some research questions, which were individually addressed in the following chapters. Chapter 2 focused on single VSC-grid interaction, where the VSC had been described as a two-port network with Y-parameters. The frequency-coupled dynamics of the VSC as well as the

sequence-coupled resonance were clearly revealed in the VSC-grid interaction with two SISO admittance ratios at the terminal of the two-port network. Yet, the admittance-ratio stability analysis rely on the knowledge that one of the admittance does not contain right half-plane zero to guarantee the correctness of stability assessment, which may fail in the multiple-VSC system. Chapter 3 used the modeling method of two-port networks with S-parameters and the reflection coefficient stability criterion to detect the existence of the right half-plane pole/zero in the admittance. Thus, the relative stability at each bus in the multiple-VSC system can be defined, the sensitive bus can be determined, as well as the potential resonance frequency can be predicted. The harmonic stability of the system was the focus in Chapter 2 and Chapter 3, providing qualitatively information, where they provided no quantitative information about the resonance in the system, especially the contribution of the VSCs to the resonance was not clearly shown. Thus, Chapter 4 investigated the resonance modes in the multiple-VSC system with the nodal admittance matrix derived with the graph theory. The phase information of the modal impedance was shown to be related to the damping characteristic of the system. By presenting the modal quality factor sensitivity index, the contributions of VSCs to the resonance modes had been quantitatively determined. In view of the high dimension of the nodal admittance matrix of multiple-VSC system, the aggregated model based on the two-port network modeling method was introduced in Chapter 5, where the asymmetrical control dynamics of the VSCs had been be preserved in the analysis large-scale power electronic based power system. Finally, the aggregated model had been tested in the analysis of Anholt offshore wind power plant.

6.2 Main Contributions

The main research contributions of this Ph.D. project are summarized below.

Equivalent admittance-ratio model for stability analysis of MIMO dynamics of VSCs

An impedance-based modeling method based on the two-port network theory is introduced in Chapter 2, where MIMO system caused by the frequency-coupled dynamics of VSC can be simplified as two SISO sub-systems allowing the use of conventional stability analysis tools.

Alternative stability criterion for interconnected systems with open-loop RHP poles

An alternative stability criterion for interconnected systems with open-loop RHP poles is introduced in Chapter 3, which does not require prior

knowledge of the number of open-loop right-half-plane poles in the impedance-ratio, which is convenient in analyzing the multi-VSC system.

Improved resonance mode analysis for VSC-based power system

The nodal admittance matrix incorporating the MIMO impedance matrices of VSCs is derived with the graph theory in Chapter 4, where the phase information of the modal impedance is shown to correspond to the quality factor of the system, which has not been investigated. The modal quality factor sensitivity analysis is then introduced in Chapter 4, by which the impact of the control parameters in VSCs to the resonance mode can be quantitatively defined.

Aggregated dynamic model for large-scale power electronic based power system

The aggregated model for large-scale power electronic based power system is derived in Chapter 5 by reducing the dimensions of nodal admittance matrix derived in Chapter 4. Thus, the influence of components change in nodal admittance matrix on the aggregated dynamic model is investigated with the eigenvalues or singular values of its submatrices. A test case with practical layout of the Anholt offshore wind power plant is studied, which shows the modularity, scalability, and the flexibility of the aggregated model.

6.3 Research Perspectives

In addition to the research gaps addressed in this Ph.D. project, some other interesting and relevant topics can be chosen for future studies. Some of the perspectives are listed as follows:

Including nonlinearities and operating-point-dependent impedance models of VSCs

Proposed impedance modeling method is based on the two-port network theory, which are assumed to be linear systems. Yet, the controllers in the VSCs usually contain limiters, e.g. ac current controllers, where the nonlinearity has to be considered for a generalized approach. Also, the impedance-models of VSC depends on the operating points, where the dynamic behavior may change severely.

Utilizing the impedance model with frequency-coupled dynamics in the time-domain simulation

The impedance models have advantages for frequency-domain analysis.

However, the impedance model with frequency-coupled dynamics obtained from the measurement cannot be directly used in time-domain simulations,e.g. the electromagnetic transients (EMT) simulation. Even if the transfer functions of impedances can be estimated through the technique like vector fitting. The frequency-coupled dynamics may be lost in vector fitting process, which affects the accuracy in the simulation. A method that can directly use the impedance model with frequency-coupled dynamics in time-domain simulation is an important topic for future research.

Online evaluation of the system stability

The stability analysis conducted in this Ph.D. project derives the open-loop gains at each bus in the system, where maybe not every one of these gains can be measured in practical system. Furthermore, the impedance models of the VSCs in the system change from time to time, e.g. the varying wind speed causes the different operating points of wind turbines. In order to make sure the system stability, an online evaluation of the system stability may be considered for further instigation.

Validation with complete wind turbine models

In the validation, impedance models consider only the basic control blocks, e.g., ac current control and PLL, where the outer control loops, such as, dc bus voltage control loop, active and reactive power control loops, are omitted to simplify the system and to reduce the time of simulations. Furthermore, the wind turbine dynamics is assumed decoupled at the dc link, where the dynamics from the machine side converter of wind turbine are neglected. A comprehensive wind turbine impedance model considering both dynamics of grid side converter and of machine side converter should be validated in the future.

Mission profile based system stability assessment

Impedance models of VSCs depend on different operating points, e.g. active power and reactive power set points, where the active power set points are related to wind speed in wind power plants and to solar irradiance in solar power plants. The concept of renewable energies mission profile is using the historical data of wind speed and solar irradiance to derive the static and dynamic load profile for reliability assessment. The load profiles can also be used to derive the impedance models of VSCs, where the impedance models can be used in future system stability assessment.

References

[1] EIA, U.S. Energy Information Administration, "International Energy Outlook 2019," 2019. [Online]. Available: https://www.eia.gov/outlooks/ieo/pdf/ieo2019.pdf

[2] REN21, Renewable Energy Policy Network for the 21st Century, "Renewables 2020 Global Status Report," 2020. [Online]. Available: https://www.ren21.net/gsr-2020/

[3] DNV GL, "Energy Transition Outlook 2020 Executive Summary," 2020. [Online]. Available: https://eto.dnv.com/2020/

[4] GWEC, Global Wind Energy Council, "Global Offshore Wing Report 2020," 2020. [Online]. Available: https://gwec.net/global-offshore-wind-report-2020/

[5] ——, "Global Wind Report 2019," 2019. [Online]. Available: https://gwec.net/global-wind-report-2019/

[6] Energinet, "Environmental Report 2018," 2018. [Online]. Available: https://en.energinet.dk/About-our-reports/Reports/Environmental-Report-2018

[7] F. Blaabjerg, Y. Yang, D. Yang, and X. Wang, "Distributed Power-Generation Systems and Protection," *Proceedings of the IEEE*, vol. 105, no. 7, pp. 1311–1331, 2017.

[8] J. Adams, C. Carter, and S. Huang, "ERCOT experience with Sub-synchronous Control Interaction and proposed remediation," in *PES T&D, Orlando, FL, USA*, 2012, pp. 1–5.

[9] S. Golestan, E. Ebrahimzadeh, J. M. Guerrero, J. C. Vasquez, and F. Blaabjerg, "An Adaptive Least-Error Squares Filter-Based Phase-Locked Loop for Synchronization and Signal Decomposition Purposes," *IEEE Trans. Industrial Electron.*, vol. 64, no. 1, pp. 336–346, 2017.

[10] X. Wang and F. Blaabjerg, "Harmonic Stability in Power Electronic-Based Power Systems: Concept, Modeling, and Analysis," *IEEE Trans. Smart Grid*, vol. 10, no. 3, pp. 2858–2870, 2019.

[11] X. Wang, L. Harnefors, and F. Blaabjerg, "Unified Impedance Model of Grid-Connected Voltage-Source Converters," *IEEE Trans. Power Electron.*, vol. 33, no. 2, pp. 1775–1787, 2018.

[12] M. Taul, "Synchronization stability of grid-connected converters under grid faults," Ph.D. dissertation, 2020, phD supervisor: Prof. Frede Blaabjerg, Aalborg University Assistant PhD supervisors: Prof. Xiongfei Wang, Aalborg University Assoc. Prof. Pooya Davari, Aalborg University.

[13] S. Peyghami, F. Blaabjerg, and P. Palensky, "Incorporating power electronic converters reliability into modern power system reliability analysis," *IEEE Journal of Emerging and Selected Topics in Power Electronics*, vol. 9, no. 2, pp. 1668–1681, 2021.

[14] C. Wan, M. Huang, C. K. Tse, and X. Ruan, "Stability of Interacting Grid-Connected Power Converters," in *2014 IEEE International Symposium on Circuits and Systems (ISCAS)*, 2014, pp. 2668–2671.

[15] X. Wang, F. Blaabjerg, and P. C. Loh, "An Impedance-Based Stability Analysis Method for Paralleled Voltage Source Converters," in *2014 International Power Electronics Conference (IPEC-Hiroshima 2014 - ECCE ASIA)*, 2014, pp. 1529–1535.

[16] A. Ghosh, G. Ledwich, F. Zare, and R. Majumder, "Stability Analysis for Multiple Voltage Source Converters Connected at a Bus," in *ENERGY 2011 : The First International Conference on Smart Grids, Green Communications and IT Energy-aware Technologies*, 2011, pp. 185–194.

[17] P. Dang, J. Petzoldt, and T. Ellinger, "Stability analysis of multi-parallel APF systems," in *Proceedings of the 2011 14th European Conference on Power Electronics and Applications*, 2011, pp. 1–8.

[18] X. Wang, F. Blaabjerg, M. Liserre, Z. Chen, J. He, and Y. Li, "An Active Damper for Stabilizing Power-Electronics-Based AC Systems," *IEEE Trans. Power Electron.*, vol. 29, no. 7, pp. 3318–3329, 2014.

[19] L. P. Kunjumuhammed, B. C. Pal, C. Oates, and K. J. Dyke, "Electrical Oscillations in Wind Farm Systems: Analysis and Insight Based on Detailed Modeling," *IEEE Trans. Sustainable Energy*, vol. 7, no. 1, pp. 51–62, 2016.

[20] ——, "The Adequacy of the Present Practice in Dynamic Aggregated Modeling of Wind Farm Systems," *IEEE Trans. Sustainable Energy*, vol. 8, no. 1, pp. 23–32, 2017.

[21] R. W. Erickson and D. Maksimovic, *Fundamentals of Power Electronics*, 2nd ed. Springer, 2001.

[22] P. Kundur, N. J. Balu, and M. G. Lauby, *Power System Stability and Control*. McGraw-hill New York, 1994, vol. 7.

[23] B. Kim and S. Sul, "Shaping of PWM Converter Admittance for Stabilizing Local Electric Power Systems," *IEEE Trans. Emerg. Sel. Topics Power Electron.*, vol. 4, no. 4, pp. 1452–1461, 2016.

[24] X. Wang, F. Blaabjerg, and W. Wu, "Modeling and Analysis of Harmonic Stability in an AC Power-Electronics-Based Power System," *IEEE Trans. Power Electron.*, vol. 29, no. 12, pp. 6421–6432, 2014.

[25] L. Harnefors, X. Wang, A. G. Yepes, and F. Blaabjerg, "Passivity-Based Stability Assessment of Grid-Connected VSCs—An Overview," *IEEE Trans. Emerg. Sel. Topics Power Electron.*, vol. 4, no. 1, pp. 116–125, 2016.

[26] X. Wang, F. Blaabjerg, and P. C. Loh, "Passivity-Based Stability Analysis and Damping Injection for Multiparalleled VSCs with LCL Filters," *IEEE Trans. Power Electron.*, vol. 32, no. 11, pp. 8922–8935, 2017.

[27] L. Harnefors, "Modeling of Three-Phase Dynamic Systems Using Complex Transfer Functions and Transfer Matrices," *IEEE Trans. Ind. Electron.*, vol. 54, no. 4, pp. 2239–2248, 2007.

[28] L. Harnefors, M. Bongiorno, and S. Lundberg, "Input-Admittance Calculation and Shaping for Controlled Voltage-Source Converters," *IEEE Trans. Ind. Electron.*, vol. 54, no. 6, pp. 3323–3334, 2007.

[29] B. Wen, D. Boroyevich, R. Burgos, P. Mattavelli, and Z. Shen, "Analysis of D-Q Small-Signal Impedance of Grid-Tied Inverters," *IEEE Trans. Power Electron.*, vol. 31, no. 1, pp. 675–687, 2016.

[30] A. Rygg, M. Molinas, C. Zhang, and X. Cai, "A Modified Sequence-Domain Impedance Definition and Its Equivalence to the dq-Domain Impedance Definition for the Stability Analysis of AC Power Electronic Systems," *IEEE Trans. Emerg. Sel. Topics Power Electron.*, vol. 4, no. 4, pp. 1383–1396, 2016.

[31] M. Cespedes and J. Sun, "Impedance Modeling and Analysis of Grid-Connected Voltage-Source Converters," *IEEE Trans. Power Electron.*, vol. 29, no. 3, pp. 1254–1261, 2014.

[32] M. Kazem Bakhshizadeh, X. Wang, F. Blaabjerg, J. Hjerrild, . Kocewiak, C. L. Bak, and B. Hesselbæk, "Couplings in Phase Domain Impedance Modeling of Grid-Connected Converters," *IEEE Trans. Power Electron.*, vol. 31, no. 10, pp. 6792–6796, 2016.

[33] D. Lu, X. Wang, and F. Blaabjerg, "Impedance-Based Analysis of DC-Link Voltage Dynamics in Voltage-Source Converters," *IEEE Trans. Power Electron.*, vol. 34, no. 4, pp. 3973–3985, 2019.

[34] B. Wen, D. Boroyevich, R. Burgos, P. Mattavelli, and Z. Shen, "Small-Signal Stability Analysis of Three-Phase AC Systems in the Presence of Constant Power Loads Based on Measured d-q Frame Impedances," *IEEE Trans. Power Electron.*, vol. 30, no. 10, pp. 5952–5963, 2015.

[35] H. Zhang, X. Wang, L. Harnefors, H. Gong, J. Hasler, and H. Nee, "SISO Transfer Functions for Stability Analysis of Grid-Connected Voltage-Source Converters," *IEEE Trans. Ind. Appl.*, vol. 55, no. 3, pp. 2931–2941, 2019.

[36] I. J. Perez-Arriaga, G. C. Verghese, and F. C. Schweppe, "Selective Modal Analysis with Applications to Electric Power Systems, PART I: Heuristic Introduction," *IEEE Trans. Power Appar. Syst.*, vol. PAS-101, no. 9, pp. 3117–3125, 1982.

[37] G. C. Verghese, I. J. Perez-Arriaga, and F. C. Schweppe, "Selective Modal Analysis With Applications to Electric Power Systems, Part II: The Dynamic Stability Problem," *IEEE Trans. Power Appar. Syst.*, vol. PAS-101, no. 9, pp. 3126–3134, 1982.

[38] X. Li, X. Chen, G. Tang, and S. Wang, "Reduced-order model of hvdc light system based on multi-time scale," in *2009 4th IEEE Conference on Industrial Electronics and Applications*, 2009, pp. 2158–2162.

[39] Y. Gu, N. Bottrell, and T. C. Green, "Reduced-Order Models for Representing Converters in Power System Studies," *IEEE Trans. Power Electron.*, vol. 33, no. 4, pp. 3644–3654, 2018.

[40] Wilsun Xu, Zhenyu Huang, Yu Cui, and Haizhen Wang, "Harmonic resonance mode analysis," *IEEE Trans. Power Deliv.*, vol. 20, no. 2, pp. 1182–1190, 2005.

[41] Z. Huang, Y. Cui, and W. Xu, "Application of Modal Sensitivity for Power System Harmonic Resonance Analysis," *IEEE Trans. Power Syst.*, vol. 22, no. 1, pp. 222–231, 2007.

[42] H. Hu, H. Tao, X. Wang, F. Blaabjerg, Z. He, and S. Gao, "Train–Network Interactions and Stability Evaluation in High-Speed Railways—Part II:

Influential Factors and Verifications," *IEEE Trans. Power Electron.*, vol. 33, no. 6, pp. 4643–4659, 2018.

[43] L. Hong, W. Shu, J. Wang, and R. Mian, "Harmonic Resonance Investigation of a Multi-Inverter Grid-Connected System Using Resonance Modal Analysis," *IEEE Trans. Power Deliv.*, vol. 34, no. 1, pp. 63–72, 2019.

[44] Z. Liu, J. Rong, G. Zhao, and Y. Luo, "Harmonic Assessment for Wind Parks Based on Sensitivity Analysis," *IEEE Trans. Sustain Energy*, vol. 8, no. 4, pp. 1373–1382, 2017.

[45] Ł. Kocewiak, B. Kramer, O. Holmstrøm, K. Jensen, and L. Shuai, "Resonance Damping in Array Cable Systems by Wind Turbine Active Filtering in Large Offshore Wind Power Plants," *IET Renew. Power Gener.*, vol. 11, 01 2017.

[46] Ö. Göksu, R. Teodorescu, C. L. Bak, F. Iov, and P. C. Kjær, "Instability of Wind Turbine Converters During Current Injection to Low Voltage Grid Faults and PLL Frequency Based Stability Solution," *IEEE Trans. Power Syst.*, vol. 29, no. 4, pp. 1683–1691, 2014.

[47] D. Yang, X. Wang, and F. Blaabjerg, "Sideband Harmonic Instability of Paralleled Inverters With Asynchronous Carriers," *IEEE Trans. Power Electron.*, vol. 33, no. 6, pp. 4571–4577, 2018.

[48] E. Ebrahimzadeh, F. Blaabjerg, X. Wang, and C. Leth Bak, "Efficient approach for harmonic resonance identification of large wind power plants," in *2016 IEEE 7th International Symposium on Power Electronics for Distributed Generation Systems (PEDG)*, 2016, pp. 1–7.

[49] Y. Cui and X. Wang, "Modal Frequency Sensitivity for Power System Harmonic Resonance Analysis," *IEEE Trans. Power Deliv.*, vol. 27, no. 2, pp. 1010–1017, 2012.

[50] WindEurope, "Wind energy in Europe 2020 Statistics and the outlook for 2021-2025," 2020. [Online]. Available: https://windeurope.org/intelligence-platform/product/wind-energy-in-europe-in-2020-trends-and-statistics/

[51] D. M. Van de Sype, K. De Gusseme, A. R. Van den Bossche, and J. A. Melkebeek, "Small-Signal Z-Domain Analysis of Digitally Controlled Converters," *IEEE Trans. Power Electron.*, vol. 21, no. 2, pp. 470–478, Mar. 2006.

[52] J. Undrill and T. Kostyniak, "Subsynchronous Oscillations Part I: Comprehensive System Stability Analysis," *IEEE Trans. Power Appr. Syst.*, vol. 95, no. 4, pp. 1446–1455, Jul. 1976.

[53] W. Ren and E. Larsen, "A Refined Frequency Scan Approach to Sub-Synchronous Control Interaction (SSCI) Study of Wind Farms," *IEEE Trans. Power Systems*, vol. 31, no. 5, pp. 3904–3912, Sept. 2016.

[54] Y. Liao and X. Wang, "Stationary-Frame Complex-Valued Frequency-Domain Modeling of Three-Phase Power Converters," *IEEE Trans. Emerg. Sel. Topics Power Electron.*, vol. 8, no. 2, pp. 1922–1933, 2020.

[55] W. Chen, *Active Network Analysis*, ser. Advanced series in electrical and computer engineering. World Scientific, 1991.

[56] R. Gilmore and L. Besser, *Practical RF Circuit Design for Modern Wireless Systems: Active circuits and systems*, ser. Active Circuits and Systems. Artech House, 2003.

[57] F. Liu, J. Liu, H. Zhang, and D. Xue, "Stability Issues of $Z + Z$ Type Cascade System in Hybrid Energy Storage System (HESS)," *IEEE Trans. Power Electron.*, vol. 29, no. 11, pp. 5846–5859, Nov 2014.

[58] H. Liu, X. Xie, X. Gao, H. Liu, and Y. Li, "Stability Analysis of SSR in Multiple Wind Farms Connected to Series-Compensated Systems Using Impedance Network Model," *IEEE Trans. Power Syst.*, vol. 33, no. 3, pp. 3118–3128, 2018.

[59] K. Kurokawa, "Power Waves and the Scattering Matrix," *IEEE Trans. Microw. Theory Techn.*, vol. 13, no. 2, pp. 194–202, Mar. 1965.

[60] P. Kundur, *Power System Stability and Control*. New York: McGrawHill, 1994.

[61] R. Dorf and R. Bishop, *Modern Control Systems*. Pearson Prentice Hall, 2011.

[62] S. Skogestad and I. Postlethwaite, *Multivariable Feedback Control: Analysis and Design*. Wiley, 2005.

[63] D. A. Frickey, "Conversions Between S, Z, Y, H, ABCD, and T Parameters which are Valid for Complex Source and Load Impedances," *IEEE Trans. Microw. Theory Techn.*, vol. 42, no. 2, pp. 205–211, Feb. 1994.

[64] AWR, Inc., "NI AWR Design Environment," v14. [Online]. Available: https://www.awrcorp.com/

[65] N. M. Nguyen and R. G. Meyer, "Start-up and Frequency Stability in High-Frequency Oscillators," *IEEE J. Solid-State Circuits*, vol. 27, no. 5, pp. 810–820, May 1992.

[66] I. H. Model and S. T. Force, "Modeling and simulation of the propagation of harmonics in electric power networks. I. Concepts, models, and simulation techniques," *IEEE Trans. Power Deliv.*, vol. 11, no. 1, pp. 452–465, 1996.

[67] J. Gross, J. Yellen, and P. Zhang, *Handbook of Graph Theory*, ser. Discrete Mathematics and Its Applications. CRC Press, 2013.

[68] Z. Fu and J. He, *Modal Analysis*. Elsevier Science, 2001.

[69] G. Kouroussis, L. Ben Fekih, C. Conti, and O. Verlinden, "EasyMod: A MatLab/SciLab toolbox for teaching modal analysis," in *Proceedings of the 19th International Congress on Sound and Vibration, Vilnius (Lithuania)*, July 9-12 2012.

[70] K. Koli, "CMOS Current Amplifiers: Speed versus Nonlinearity," Ph.D. dissertation, chapter 6, Helsinki University of Technology Electronic Circuit Design Laboratory, 2000.

[71] Ørsted, DK. (2019), "Anholt Offshore Wind Farm." [Online]. Available: http://dise.org.pl/dania2019/AnholtOffshoreWindFarm.pdf

[72] P. Brogan and N. Goldenbaum, "Harmonic Model of the Network Bridge Power Converter for Wind Turbine Harmonic Studies," in *The 11th Int. Workshop on Large-Scale Integration of Wind Power into Power Systems as well as on Transmission Networks for Offshore Wind Power Plants*, Lisbon, 2012, pp. 538–544.

[73] EstralinHVC, "Power Cables and Cable Systems 6-220 kV." [Online]. Available: http://estralin.com/files/catalogues/Kabel-eng.pdf

[74] S.-K. Chung, "Phase-locked loop for grid-connected three-phase power conversion systems," *IEE Proceedings – Electric Power Applications.*, vol. 147, no. 3, pp. 213–219, May 2000.

ISSN (online): 2446-1636
ISBN (online): 978-87-7210-964-0 AALBORG UNIVERSITY PRESS